

Studying (Electro)Chemical Catalysis of Au Nanoparticles and Carbon
Nanostructures Using Single Molecule Fluorescence Microscopy

A Dissertation

Presented to the Faculty of the Graduate School

of Cornell University

in Partial Fulfillment of the Requirements for the Degree of

Doctor of Philosophy

by

Hao Shen

January 2015

© 2015 Hao Shen

Studying (Electro)Chemical Catalysis of Au Nanoparticles and Carbon Nanostructures Using Single Molecule Fluorescence Microscopy

Hao Shen

Cornell University 2015

This dissertation presents the results on studies of chemical and electrochemical catalysis using single molecule fluorescence microscopy. With its real-time, single-turnover observations at millisecond, sub-diffraction limit resolutions, the single molecule fluorescence microscopy is a powerful technique in interrogating nanocatalysts in catalyzing chemical and electrochemical transformations. In this work, three major topics are covered: (i) revealing a hidden surface reaction intermediate in a catalytic process on a single nanoparticle, (ii) visualizing monolayer graphene oxide sheets in electrocatalysis and monitoring their activity changes upon electrochemical reduction, and (iii) studying electrochemical catalysis of arrays of aligned single-walled carbon nanotubes.

Detecting and characterizing reaction intermediates is important and powerful for elucidating reaction mechanisms, but challenging in general because of the low populations of intermediates in a reaction mixture. Studying surface reaction intermediates in heterogeneous catalysis presents additional challenges, especially the ubiquitous structural heterogeneity among the catalyst particles and the accompanying polydispersion in reaction kinetics. The single molecule fluorescence spectroscopy was used in this work to study the oxidative N-deacetylation of amplex red catalyzed by Au@mSiO₂ nanorods and 5.3 nm Au nanoparticles. The distribution of microscopic reaction times for the catalysts followed the initial-rise-and-then-decay behaviors,

indicating a kinetic intermediate straddled by two rate determining steps. The rate constant for each step was quantified, and a working mechanism was formulated for the catalytic kinetics.

Graphene oxide sheets are a novel material that can be potentially used for the electrochemical, optoelectronic and mechanical related applications. Challenges in the research of graphene oxide sheets include imaging the single-sheet and understanding the electrochemical activity. By using a fluorogenic reaction, the electrochemical catalysis of graphene oxide sheets was studied in real time. Morphologies of individual sheets were revealed by this fluorescence microscopy approach, including the boundaries, wrinkles and folded regions. A graphene oxide sheet might be divided into different regions whose electrochemical activities were studied and compared. A constant negative potential was applied to the graphene oxide sheets for their partial reduction while monitoring the activity changes.

The fundamental understanding of single-walled carbon nanotubes in electrochemical processes is important for tailoring their structures for optimal performances. Single molecule fluorescence microscope was applied to study large arrays of aligned single-walled carbon nanotubes. Super-resolution imaging technique was used to precisely locate the active sites at the sub-diffraction limit resolution. After the single molecule study, the same piece of sample was imaged by AFM and SEM to overlay the active sites on top of nanotubes. Multiple active sites were observed on the same nanotube at different locations, and compared in terms of the dependence of substrate concentrations and applied potentials.

BIOGRAPHICAL SKETCH

Hao Shen obtained his B.S. in Chemistry from Nanjing University, China, in 2007. During his undergraduate studies, he worked with some research projects, in which one was the preparation of high surface area acidic carbons for the reforming of dimethoxymethane to produce hydrogen. Hao later moved to Ithaca, New York, where he attended graduate school in the Department of Chemistry and Chemical Biology at Cornell University, and was supervised by Professor Peng Chen. His PhD research was about the single-molecule study of electrocatalysis on carbon nanotubes and other carbon-based materials. He also studied the intermediates and kinetic mechanisms at the single-molecule level for the catalytic reactions on the surface of Au nanoparticles.

Dedicated to Rongrong Wang and Jianyi Shen

ACKNOWLEDGMENTS

I would like to express my deepest gratitude to my advisor, Peng Chen, as none of the work would be possible without his guidance and help. As an advisor, his passion and enthusiasm for research inspired me the quality of a good researcher. I also thank my committee member Prof. Héctor Abruña for taking the time carefully read and edit my dissertation; Prof. Jiwoong Park, for his valuable feedback and scientific insights.

I am grateful to the former and present members of Chen group, whose supports, contribution and discussions were of great value to my research: Weilin Xu, for his foundational study on single-molecule electrocatalysis; Xiaochun Zhou, for starting the single-molecule super-resolution imaging study on Au catalyst, and generously sharing his Matlab codes; Debashis Panda, Jérôme Benitez, Aaron Keller and Nesha May Andoy, for training me in optics and single-molecule microscopy; Tai-yen Chen, for his patience in helping me improving the coding; Justin Sambur and Eric Choudhary, for the frequent discussion on electrocatalysis and providing valuable insights; Ningmu Zou, for providing the TEM images of Au@mSiO₂ nanorods; and Feng Yang, for his friendship and being a wonderful roommate.

My thanks also go to the collaborators who provided me samples for single-molecule measurements. They are Michael Segal in Prof. Jiwoong Park's group, who designed and fabricated the aligned single-walled carbon nanotubes on quartz wafer; and Jaemyung Kim, in Prof. Jiaxin Huang's group, Northwestern, who synthesized the large sized single-layered graphene oxide sheets.

Last, but not least, I would like to thank my mother, Rongrong Wang and father, Jianyi Shen. Despite the distance, their supports and encouragements kept me through my entire PhD, and I will forever be in debt to their future happiness.

TABLE OF CONTENTS

CHAPTER 1: PAST APPLICATIONS OF SINGLE-MOLECULE FLUORESCENCE		
MICROSCOPY IN CHEMICAL CATALYSIS AND ELECTROCHEMICAL CATALYSIS 1		
1.1 INTRODUCTION	1	
1.2 PIONEERING STUDIES IN SINGLE-MOLECULE ENZYMOLOGY	2	
1.3 SINGLE-MOLECULE KINETICS OF NANOPARTICLE CATALYSIS	4	
1.4 SINGLE-MOLECULE NANOSCALE ELECTROCATALYSIS.....	9	
1.5 STRUCTURE AND CATALYTIC ACTIVITY CORRELATION AND SUPER- RESOLUTION IMAGING	12	
1.6 SCOPE OF THIS THESIS	16	
1.7 REFERENCES	18	
CHAPTER 2: SINGLE-MOLECULE KINETICS REVEALS A HIDDEN SURFACE		
REACTION INTERMEDIATE IN SINGLE-NANOPARTICLE CATALYSIS		23
2.1 INTRODUCTION	23	
2.2 MATERIALS AND METHODS	25	
2.2.1 Synthesis and Characterization of Au Nano-catalysts.....	25	
2.2.2 Catalytic Reaction Conditions.....	26	
2.2.3 Single-Molecule Fluorescence Microscopy	26	

2.2.4 Scanning Electron Microscopy (SEM).....	27
2.3 RESULTS AND DISCUSSION	27
2.3.1 Catalytic Reaction and Catalysts.....	27
2.3.2 Single-Turnover Kinetics of Single Au@mSiO ₂ Nanorods Reveals A Reaction Intermediate.....	30
2.3.3 Single-Turnover Kinetics of Single 5.3 nm Pseudospherical Bare Au Nanoparticles Again Reveals a Reaction Intermediate	34
2.3.4 Mechanism of Catalysis	37
2.3.5 Inhomogeneity and Size-Dependence of Nanocatalyst Reactivity.....	43
2.4 CONCLUSION	46
2.5 REFERENCES	47
2.6 SUPPORTING INFORMATION	53
2.6.1 Au Nanocatalysts Preparation and Characterization	53
2.6.1.1 Preparation of Au@mSiO ₂ Nanorods	53
2.6.1.2 Structural Characterization of Au Nanocatalysts.....	54
2.6.1.3 Determining the Lengths of Au Nanorod Core from the SEM Images of Individual Au@mSiO ₂ Nanorods	55
2.6.2 Analysis Procedures to Extract the Fluorescence Intensity vs Time Trajectories during Catalysis of Single Nanocatalysts	55
2.6.2.1 Analysis Procedures for 5.3 nm Pseudospherical Nanoparticles	56
2.6.2.2 Analysis Procedures for Au@mSiO ₂ Nanorods	56

2.6.2.3 Distribution of Fluorescence Burst On-Time during Catalysis by Au Nanocatalysts	57
2.6.3 The Distribution of Compiled τ	58
2.6.3.1 Distributions of τ Compiled from Many Au@mSiO ₂ Nanorods	58
2.6.3.2 Distributions of τ Compiled from Many 5.3 nm Au Nanoparticles	59
2.6.4 Kinetic Mechanism and Derivation of the Probability Density Function $f(\tau)$ of the Microscopic Reaction Time τ	60
2.6.4.1 Mechanism 1: Surface-Adsorbed AR• Being the Kinetic Intermediate ...	63
2.6.4.2 Mechanism 2: Surface-Adsorbed OH• Being the Kinetic Intermediate ..	68
2.6.5 References	73

CHAPTER 3: VISUALIZING GRAPHENE OXIDE SHEETS AND STUDYING THEIR ELECTROCHEMISTRY BY FLUORESCENCE MICROSCOPY	76
3.1 INTRODUCTION	76
3.2 MATERIALS AND METHODS	78
3.2.1 Synthesis of Graphene Oxide (GO)	78
3.2.2 Modified Fluorescence Quenching Microscopy (FQM)	79
3.2.3 Ensemble Electrochemical Catalysis	79
3.2.4 Fluorescence Enabled Electrochemical Microscopy	80
3.2.5 Normalization of Laser Intensity within Electrochemical Cell	81

3.2.6 Algorithm of Canny Edge Detection	81
3.2.6.1 Smooth Entire Image by Applying a Gaussian Mask	82
3.2.6.2 Sobel-Operator Determined Derivative and Gradient	82
3.2.6.3 Applying Non-Maximum Suppression	83
3.2.6.4 Edge Filtering by Low and High Thresholding	84
3.3 RESULTS AND DISCUSSION	84
3.3.1 Morphology of As-Received GO under Fluorescence Quenching Microscope (FQM)	84
3.3.2 Ensemble GOs Electrocatalyzed Reduction of Resazurin	87
3.3.3 Electrochemistry of GOs by Observing the Fluorescent Product Molecules	89
3.3.4 Electrochemical Fluorescence Imaging of GOs and Mapping the Sub-Structures	95
3.3.5 Electrochemical Reduction and Activity Change	98
3.3.6 The Electrochemical Activity Changes of GO in Multistage Reduction	103
3.3.7 Raman Spectrum Correlated Activity Measurement	103
3.4 REFERENCES	107
CHAPTER 4: SINGLE-MOLECULE ELECTROCATALYSIS ON ALIGNED ARRAYS OF SINGLE-WALLED CARBON NANOTUBES	112
4.1 INTRODUCTION	112

4.2 MATERIALS AND METHODS	114
4.2.1 Fabrication of Aligned SWNTs	114
4.2.1.1 Etching Mapping Features on Quartz Wafer	114
4.2.1.2 Depositing Fe Catalyst for SWNT Growth	115
4.2.1.3 The Growth of SWNTs	115
4.2.1.4 Depositing Au electrodes	115
4.2.2 Sample Preparation for Single-Molecule Electrocatalysis Imaging	117
4.2.2.1 Cleaning the Quartz Slide with Aligned SWNTs	117
4.2.2.2 Electrochemical Flow Cell and Probing Reaction for Single-Molecule Electrocatalysis	117
4.2.3 Single-Molecule Fluorescence Microscopy	118
4.2.4 Super-Resolution Imaging of Reactive Sites	118
4.3 RESULTS AND DISCUSSION	121
4.3.1 Morphologies of Aligned SWNTs	121
4.3.2 Selection of Possible Active Sites in Single-Molecule Electrocatalysis	123
4.3.2.1 Extraction of Fluorescence Time Trajectory	123
4.3.2.2 Correlating the Locations of Fluorescent Bursts with SEM Image	123
4.3.2.3 Further Filtering of the Possible Active Site with Super-Resolution Imaging	124
4.3.3 Resazurin Concentration Titration on Aligned SWNTs	127

4.3.4 Potential Titration on Aligned SWNTs	131
4.3.5 Proton Concentration Titration on ITO Supported Commercial SWNTs	132
4.4 REFERENCES	134

LIST OF FIGURES

Figure 1.1 Enzymology of Cholesterol Oxidase (COx)	7
Figure 1.2 Kinetic Mechanism of 6 nm Au Nanoparticle Catalyzed Resazurin Reaction	8
Figure 1.3 Single-molecule Electrocatalysis of Single-Walled Carbon Nanotubes and Its Underlying Kinetics	11
Figure 1.4 Spatially Resolved Activity Distribution on LDH Single Crystal, Au@mSiO ₂ Nanorod and Au@mSiO ₂ Nanoplate	15
Figure 2.1 Au Nanoparticles Catalyzed N-deacetylation of Amplex Red by H ₂ O ₂	29
Figure 2.2 Single Au@mSiO ₂ Nanorod Catalysis	33
Figure 2.3 Single 5.3 nm Au Nanoparticle Catalysis	36
Figure 2.4 Ensemble Reaction Rate of Bare 5.3 nm Au Nanoparticles	42
Figure 2.5 Distribution of Rate Constants for Au@mSiO ₂ and 5.3 nm Au Nanoparticles	45
Figure S2.1 TEM Characterization of the 5.3 nm Au Nanoparticles and Au@mSiO ₂ Nanorods	54
Figure S2.2 SEM Image of Au@mSiO ₂ Nanorods	55
Figure S2.3 Distribution of Fluorescence Burst On-Time	58
Figure S2.4 Distribution of τ Compiled from Many Au@mSiO ₂ Nanorods	59
Figure S2.5 Distribution of τ Compiled from Many 5.3 nm Au Nanoparticles	59
Figure 3.1 Determining the Direction of Gradient in Canny Edge Detection	83

Figure 3.2 Visualizing GOs by Fluorescence Quenching Microscopy (FQM)	86
Figure 3.3 GOs-Catalyzed Electrochemistry of Resazurin	88
Figure 3.4 Scheme of Flow Cell for GOs Catalysis and the Stability of GOs in Electrocatalysis	93
Figure 3.5 Illustration of Triangular Potential Waveform, the Cycle Averaged Fluorescent Intensity from a Piece of GO and the Corresponding Time Derivative	94
Figure 3.6 Electrochemical Fluorescence Imaging of GO, Edge Detection by Canny Method and Defining Regions by Expanding Edge Lines	97
Figure 3.7 Fluorescence Intensity Represented Electrocatalytic Activity Change upon Electrochemical Reduction	101
Figure 3.8 The Electrochemical Activity Change of GO by Stepwise Reduction	105
Figure 3.9 Raman Spectrum Correlated with Electrochemical Activity Measurement	106
Figure 4.1 SEM of SWNTs on Quartz Chip	116
Figure 4.2 Super-Resolution Imaging of SWNT Reactive Sites	120
Figure 4.3 AFM Images of One Block of Aligned SWNTs Before and After Carrying out Electrocatalysis	122
Figure 4.4 Single-Turnover Detection of Aligned SWNTs Electrochemical Catalysis	126
Figure 4.5 Resazurin Concentration Dependence from Two Individual Active Sites	130
Figure 4.6 Potential Dependence of $\langle\tau_{on}\rangle^{-1}$	132
Figure 4.7 Proton Concentration Dependence of $\langle\tau_{on}\rangle^{-1}$	133

LIST OF TABLE AND SCHEMES

Table 3.1 Peak Potential Changes upon Electrochemical Reduction from the Fluorescence Current Curve	102
Scheme 2.1 Possible Reaction Steps of Amplex Red Oxidation by H ₂ O ₂ Catalyzed on Au Nanoparticle Surfaces	42
Scheme 2.2 Minimal Kinetic Mechanism	43
Scheme S2.1 Balanced Chemical Equation of Oxidative Deacetylation of Amplex Red by H ₂ O ₂ to Generate Resorufin, Acetate, and Water	60
Scheme S2.2 Possible Mechanism of Catalysis	60
Scheme S2.3 Reduced Effective Kinetic Mechanism with AR• Being the Observed Reaction Intermediate	63
Scheme S2.4 Reduced Kinetic Mechanism with OH• Being the Observed Reaction Intermediate	68

CHAPTER ONE

PAST APPLICATIONS OF SINGLE-MOLECULE FLUORESCENCE MICROSCOPY IN CHEMICAL CATALYSIS AND ELECTROCHEMICAL CATALYSIS

1.1 Introduction

The efficient usage of fossil fuels and the seeking for alternative energy feedstock are critical to mankind's sustainable future, because of the increasing energy demands and the declining reserves of fossil fuels. Catalysis and electrochemical catalysis are widely used in chemoselective processing of fossil fuels, removing pollutants from gas exhausts and promoting solar energy conversion to fuels.¹⁻¹² Therefore, they are considered one of the key technologies to meet the energy challenges. Nanoparticle catalysts are an integral part of catalysis technology, and they can catalyze many energy conversion related reactions. Partly owing to their high surface-to-volume ratios and new electronic properties, nanoparticle catalysts often show new or superior activity compared to their bulk counterparts.^{2-4, 13} To improve the performances of current nanoparticle catalysts and design new ones is one of the major goals in today's catalysis research. In order to achieve these goals, an essential task is to understand the fundamental structure-activity correlation of nanoscale materials for catalysis and electrochemical catalysis, as well as studying their underlying mechanisms during the catalytic processes.

There are tremendous efforts in characterizing the catalytic properties of nanoparticles at the ensemble level, where a collection of nanoparticles are studied simultaneously. Significant insights have been made into the structure-activity correlations of nanoparticle catalysts. However, this ensemble-averaged characterization is not precise, since nanoparticle catalysts always have structural dispersions, such as in sizes and shapes; even on a single particle, surface atoms reside

at various corners, edges, and facet sites.¹³⁻¹⁵ This structure heterogeneity inevitably leads to different properties among individual particles, and presents a great challenge for traditional characterization methods, where only averaged catalytic behaviors are obtained while individuality is lost.

To address these questions, one needs to study the nanoparticle catalysis at the single-particle level. The rapid technological advances have made it possible to detect the fluorescence of a single molecule readily under ambient conditions.¹⁶⁻²⁴ By applying this single-molecule approach to catalysis and electrochemical catalysis, one can directly probe the individuality among nanocatalysts. Besides removing the ensemble averaging, it also allows visualization of catalytic reactions in real time with single-turnover resolution. With tens of milliseconds time resolution at a single nanocatalyst, this approach becomes a powerful tool to dissect the reaction mechanism. Moreover, by applying the super-resolution approach, the single-molecule fluorescence detection can offer optical imaging beyond the diffraction-limited resolution, giving tens of nanometers resolution.

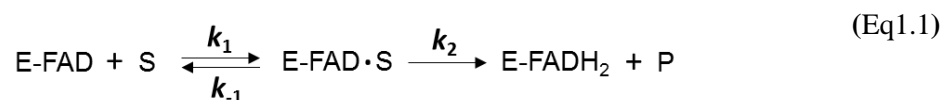
The single-molecule fluorescence microscopy has been proven a powerful tool to quantitatively study metal nanoparticles and carbon nanostructures in catalysis and electrochemical catalysis in a spatially resolved fashion.^{16, 25} Continuous efforts are being made into this field and many exciting insights are discovered. The following sections present examples of the wide applications of single-molecule fluorescence microscopy in catalysis.

1.2 Pioneering Studies in Single-Molecule Enzymology

Single-molecule fluorescence microscopy was applied to biocatalysis prior to heterogeneous catalysis.^{22, 26-29} Much alike the nanoparticle heterogeneous catalysis, the enzyme based biocatalysis study is also limited in conventional measurements for the following reasons.

First, the activity differences among identical enzymes could be as large as one magnitude.³⁰⁻³² This activity heterogeneity is known as the static disorder. In addition, each enzyme is in constant conformational changes, which inevitably leads to a time-dependent activity fluctuation.^{30, 33-35} Observing this dynamic disorder is a challenging task for bulk measurements, because at any given time, the measured results are a mixture of enzymes at all possible conformations. In enzyme kinetics, the Michaelis-Menten model is often used,^{20, 36-41} where the substrate reversibly binds to enzyme forming an intermediate before it is fully converted to the final product. This intermediate state, however, is usually concealed, because the concentration of steady-state intermediate is too low to be detected.⁴² The single-molecule fluorescence microscopy, on the other hand, meets all the above challenges.

The single enzyme study done by Xie and coworkers is one of the best examples that illustrate the single-molecule fluorescence microscopy being a very informative technique in enzymology.²⁰ In their work, they studied the single cholesterol oxidase (COx) catalyzed oxidation of cholesterol by oxygen (Figure 1.1A). This enzyme involves a fluorescent cofactor (flavin adenine dinucleotide, FAD), which gets reduced in the catalytic cycle and becomes nonfluorescent (FADH₂). Without catalysis, the fluorescent intensity from a single COx enzyme shows slow fluctuation, indicating the enzyme conformational changes around the fluorescent FAD center, which is a hidden process in ensemble-averaging measurements. With an excess amount of cholesterol and oxygen, the catalytic transformation starts to take place, which is reflected in the fluorescent intensity as a digital on-off behavior (Figure 1.1B). The non-exponential on-time distribution indicates the existence of the substrate-bound state, which was well explained by the Michaelis-Menten mechanism (Eq 1.1).



They further extracted the rate constant k_2 for individual enzymes, which had a broad distribution reflecting the static disorder (Figure 1.1C). Moreover, the positive autocorrelation function of on-time (Figure 1.1D) had a slowly decay timescale that matched the fluorescence intensity fluctuations from a single COx, which further confirmed that the dynamic disorder indeed stemmed from the conformational dynamics.

1.3 Single-molecule kinetics of nanoparticle catalysis

Aside from being a powerful tool in enzymology, the single-molecule approach has approved its own value in heterogeneous catalysis as well. The pioneering work was respectively done by Hofkens, Majima and Chen with their coworkers on single-crystal catalysis, TiO₂ and Au nanoparticles.^{22, 43-44} The Au nanoparticle work is used here as an example to illustrate the uniqueness of single-molecule approach in catalysis.

In this work, the non-fluorescent substrate molecule resazurin was catalyzed to become the highly fluorescent product resorufin with reductant hydroxylamine at single-reaction resolution. Similar to enzyme catalysis, the fluorescence time trajectories from single Au nanoparticles were also digitalized with consistent heights of their on-level, which is characteristic of single-molecule fluorescence detection (Figure 1.2A). Each sudden intensity increase in the trajectory marked a product formation event on a nanoparticle. The product molecule stayed on the nanoparticle for a while due to its finite affinity for the nanoparticle surface before dissociation; the dissociation is marked by a sudden intensity decrease in the trajectory. Every off-on cycle in the trajectory corresponded to a single turnover of a catalytic formation of a product and its subsequent dissociation from one nanoparticle. In a single-particle fluorescence turnover trajectory, the waiting times, τ_{off} and τ_{on} , are the two most important observables (Figure 1.2A). Their clean resolution separates the catalysis into two parts temporally: τ_{off} is the waiting time before the

formation of each product, and τ_{on} is the waiting time for the product dissociation after its formation. The individual values of τ_{off} and τ_{on} are stochastic, but their statistical properties, such as their distributions and averages, are defined by the underlying reaction kinetics.

One of the major differences between the enzyme (homogeneous) catalysis and nanoparticle (heterogeneous) catalysis is on the kinetic mechanism. The most commonly used mechanism for enzymology is the classic Michaelis-Menten mechanism, which applies for one-site, one-substrate kinetic model. However, there exist multiple catalytic sites for nanoparticles, and therefore the Michaelis-Menten model is not appropriate any more. To address this issue, Chen and coworkers used the Langmuir-Hinshelwood mechanism which explicitly includes the multiplicity of catalytic sites. The $\langle \tau_{\text{off}} \rangle^{-1}$ ($\langle \rangle$ denotes averaging), representing the rate of product formation, takes the form of:

$$\langle \tau_{\text{off}} \rangle^{-1} = \frac{\gamma_{\text{eff}} K_1 [\text{S}]}{1 + K_1 [\text{S}]} \quad (\text{Eq1.2})$$

where γ_{eff} is the effective rate constant, K_1 is the adsorption-desorption equilibrium constant of the substrate resazurin (S); $[\text{S}]$ is the substrate concentration. The Langmuir isotherm $\frac{K_1 [\text{S}]}{1 + K_1 [\text{S}]}$ gives an increase and then saturation kinetics of $\langle \tau_{\text{off}} \rangle^{-1}$ versus the substrate concentration, which well predicted the experimental results (Figure 1.2C).

In a single-particle turnover trajectory, τ_{on} starts at the moment when a product molecule forms on a particle surface, and ends once this product leaves the particle surface. Strikingly, τ_{on} also showed a $[\text{S}]$ dependence, which suggested two parallel pathways for product dissociation: one was the direct desorption; and the other, the substrate assisted product desorption (Figure 1.2B).¹⁷ In this mechanism, k_2 and k_3 were two apparent rate constants respectively for these two desorption pathways. With different relative magnitudes of k_2 and k_3 , this mechanism immediately

predicts three types of [S] dependence of $\langle \tau_{\text{on}} \rangle^{-1}$: Type I : $\langle \tau_{\text{on}} \rangle^{-1}$ increases with the increase of [S] and eventually saturates if $k_2 > k_3$; Type II : $\langle \tau_{\text{on}} \rangle^{-1}$ decreases with the increase of [S] and flattens if $k_2 < k_3$; Type III: $\langle \tau_{\text{on}} \rangle^{-1}$ is independent of [S] if $k_2 = k_3$, or $k_1/(k_{-1}+k_2) = 0$. All three types of behaviors were observed for individual 6-nm Au-nanoparticles (Figure 1.2D), and they have different subpopulations: 66% of Au-nanoparticles are Type I , 19% are Type II , and 15% are Type III.¹⁶ These different behaviors are manifestations of the differential selectivity of individual Au-nanoparticles between the two parallel product dissociation pathways. This differential selectivity is completely hidden in nanoparticle averaged results, which are dominated by the behavior of the Type I particles.⁴⁵

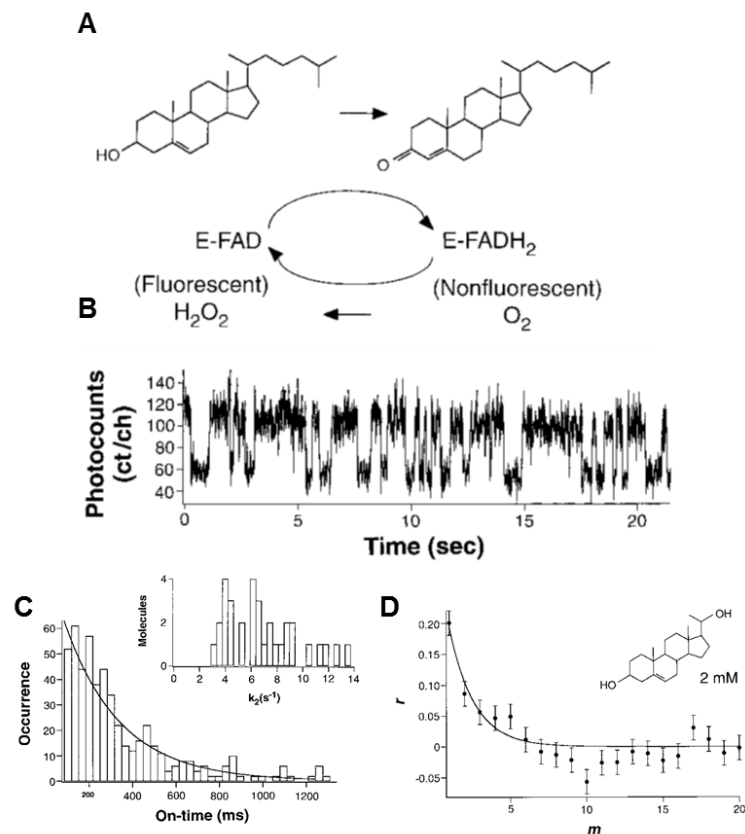


Figure 1.1 (A) The enzymatic cycle of cholesterol oxidase (COx). (B) Real-time observation of single COx catalyzing cholesterol molecules. (C) The on-time distribution from a single COx molecule with 2 mM 5-pregene-3 β -20 α -diol substrate. The insert is the static distribution of k_2 . (D) The autocorrelation function of on-time from a single COx with 2 mM 5-pregene-3 β -20 α -diol substrate. Figures adapted from Xie et al.²⁰ Copyright 1998 American Association for the Advancement of Science.

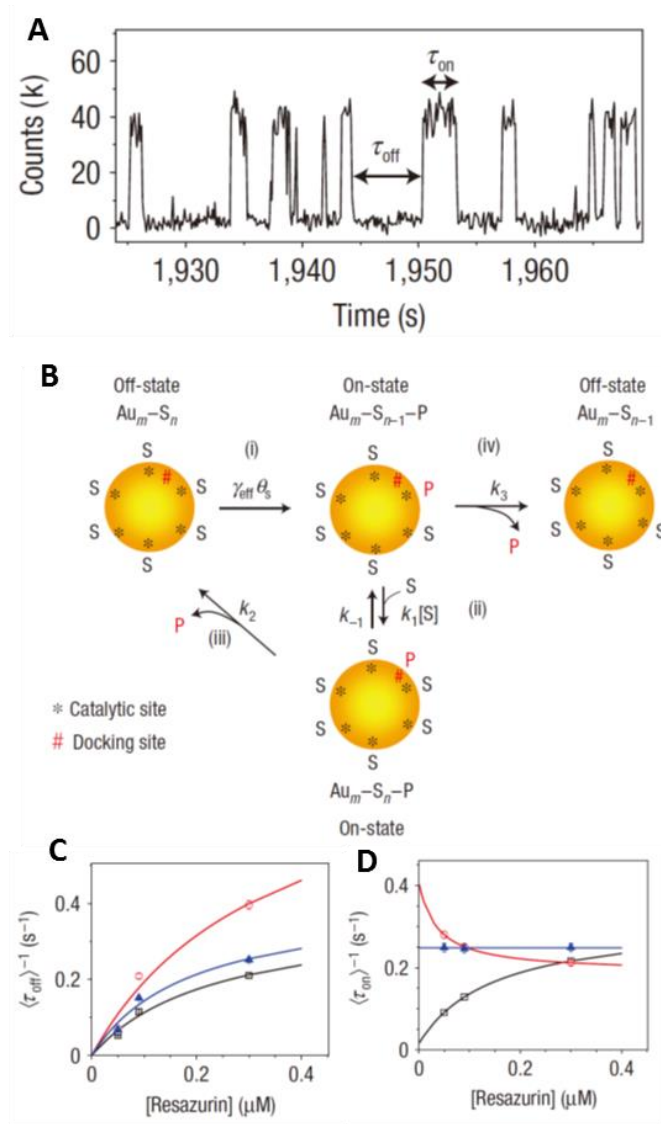


Figure 1.2 (A) Segment of the fluorescence time trajectory from a 6-nm Au nanoparticle. (B) Kinetic mechanism of Au-nanoparticle catalysis. Au_m : Au-nanoparticles; S: the substrate resazurin; P: the product resorufin; Au_mS_n represents an Au-nanoparticle having n adsorbed substrate molecules. (C) Resazurin concentration dependence of $\langle \tau_{\text{off}} \rangle^{-1}$ from three 6-nm Au-nanoparticles. Each titration is from one nanoparticle. (D) Resazurin concentration dependence of $\langle \tau_{\text{on}} \rangle^{-1}$ from three individual Au-nanoparticles with Type I, Type II and Type III behaviors. Figures adapted from Xu et al.⁴³

1.4 Single-Molecule Nanoscale Electrocatalysis

Another example of the wide applications of the single-molecule approach was on the electrocatalysis of single-walled carbon nanotubes (SWNTs) done by Chen and coworkers.²⁵ SWNTs can electrocatalyze reactions such as the oxygen reduction reaction (ORR), thus are attractive for energy related applications. The single SWNT electrochemistry was done previously by Crooks and Dekker et al via direct current measurements.⁴⁶⁻⁴⁸ However, this method required delicate engineering to attach the SWNT to electrodes, and thus was limited for multiplexed observations. With the wide-field fluorescence microscopy, Chen and coworkers were able to simultaneously study the electrochemistry of a single SWNT at single turnover level from multiple SWNTs.

In this work, the two-stage electrochemical reduction of resazurin to the highly fluorescent resorufin, then to nonfluorescent dihydroresorufin was used as the probe to measure the activity of individual SWNTs (Figure 1.3A). Unlike the chemical catalysis by an Au nanoparticle, the sudden intensity decreases in the fluorescence time trajectory primarily resulted from electro-reduction of resorufin to dihydroresorufin.²⁵ At constant electrochemical potentials, the electro-reduction of resorufin to dihydroresorufin contained in τ_{on} followed a simple, one step reaction kinetics (reaction (iv), Figure 1.3B). This simple kinetic mechanism of resorufin electro-reduction was manifested experimentally in that $\langle \tau_{\text{on}} \rangle^{-1}$ was independent of resazurin concentration (Figure 1.3C). For the electrocatalytic formation of resorufin contained in τ_{off} , the reaction kinetics contained two parallel reaction pathways. One involved a substitution reaction of dihydroresorufin by resazurin at the reactive site followed by electrocatalytic reduction (reactions (i) and (ii), Figure 1.3B), the other was a direct electro-oxidation of dihydroresorufin to resorufin (reaction (iii)). This electro-oxidation is possible because the redox of resorufin to dihydroresorufin redox is reversible (Figure 1.3A).

By analyzing many fluorescence electrocatalysis trajectories, the distributions of kinetic rate constants among many SWNT reactive sites were obtained at any applied potential, for example those of k_2^{red} and k_4^{red} in Figure 1.3D. As expected, their distributions were dependent on the applied potential. Relative to their average values, the distribution widths of all rate constants were broad, indicating the large reactivity inhomogeneity among the SWNT reactive sites. Several of these rate constants, such as k_2^{red} and k_4^{red} , involve interfacial electron transfer from a SWNT to an adsorbed molecule and were thus related to the electronic properties of the SWNT reactive sites. This work again showed that single-molecule approach is a powerful method in dissecting kinetic mechanisms of reactions.

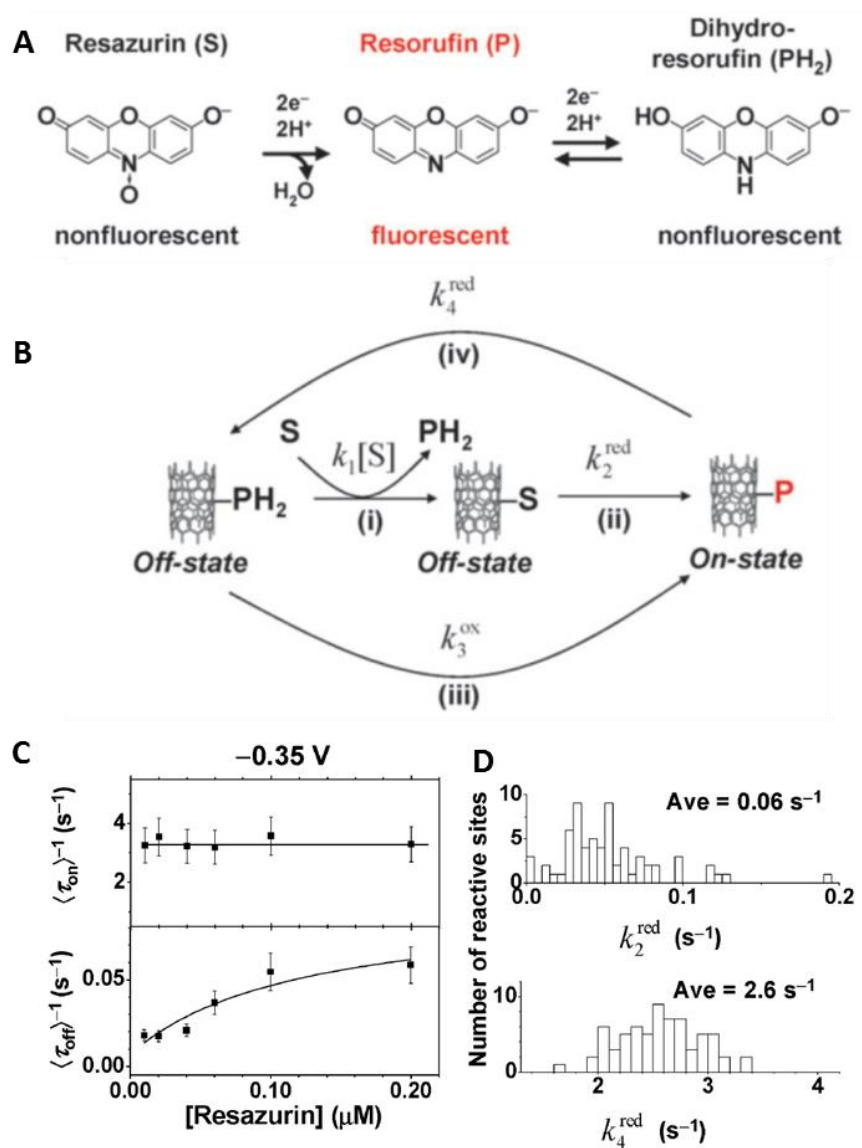


Figure 1.3 (A) Redox chemistry of resazurin in aqueous solution. (B) Scheme of the kinetic mechanism. The fluorescence state (on or off) is indicated at each stage of the reaction. S: resazurin; P: resorufin; PH₂: dihydroresorufin. (C) Resazurin concentration dependence of $\langle \tau_{on} \rangle^{-1}$ and $\langle \tau_{off} \rangle^{-1}$ of a single reactive site at -0.35 V (vs. Ag/AgCl). (D) Distribution of k_2^{red} and k_4^{red} from many SWNT reactive sites at -0.35 V. Figures adapted from Xu et al.²⁵ Copyright 2009 American Chemical Society.

1.5 Structure and catalytic activity correlation and super-resolution imaging

Other than being a powerful tool in studying the kinetic mechanism in catalysis and electrochemical catalysis, single molecule fluorescence approach is also useful in understanding the structure-activity correlation due to its powerful spatial resolution. One of the first studies in spatially resolved catalytic activity was done by Hofkens and his coworkers on the $[\text{Li}^+-\text{Al}^{3+}]$ layered double hydroxide (LDH) catalyst.²² In this work, both the hydrolysis and transesterification of the non-fluorescent 5-carboxyfluorescein diacetate (C-FDA) was catalyzed by LDH, yielding a fluorescent product (Figure 1.4A and B). Single molecule results showed that the active sites for the transesterification reaction was non-specifically distributed on the $\{0001\}$ facets, as the fluorescent products were generated all over the basal plane. On the other hand, the hydrolysis reaction was location specific. Majority of the products were found at the crystal edges with very few at the basal plane. This structure related activity preference was due to the OH^- ions exchange at the $\{1010\}$ facet, which can only be predicted indirectly by conventional methods, but observed directly with the single molecule fluorescence microscopy. By tracking the product molecule and examining the mean square displacement ($\langle r^2 \rangle$), they found that although most of the product molecules were highly mobile ($> 90\%$), there exist a small portion of molecules that were almost immobile on catalyst surface.

Furthermore, Hofkens and his coworkers studied the zeolite chemistry with confocal fluorescent microscopy. In one case, two fluorescence probes were used to image the outer and inner surfaces of ZSM-5 zeolites respectively.⁴⁹ The larger probe, an asymmetrically substituted perylene diimide dye (PDI-TEA) being pre-quenched in free base, could react with the acid site to restore the fluorescence. The smaller probe, 4-(4-diethylaminostyryl)-*N*-methylpyridinium iodide (DAMPI) could enter the zeolite pores, and become fluorescent because of the pore size confinement preventing the trans-cis isomerization.⁴⁹⁻⁵⁰ With this fluorescence approach, they

proved that the acid sites on the outer surface of ZSM-5 are uniform. Moreover, the single crystals are accessible for substrate molecules from the straight pores located on {010} facets.

Albeit the optical microscopy based activity study contains rich spatial information, it has a spatial resolution limit: the well-known diffraction-limited resolution, defined by the Rayleigh criterion (Equation 1.3):

$$\text{Resolution}_{x,y} = \frac{0.61\lambda}{\text{N.A.}} \quad (\text{Eq1.3})$$

where λ is the wavelength, and N.A. is the numerical aperture of the objective.⁵¹⁻⁵³ In a typical experiment, the spatial resolution is usually between 200~300 nm, with which many nanoparticle catalysts would appear as point objects. Therefore, the optical diffraction limited approach is only suitable for large sized catalysts. To overcome this diffraction limit, mathematical fitting of the fluorescence point spread functions (PSF) was used to achieve higher resolution. This technique, known as super-resolution imaging,⁵⁴⁻⁶⁶ again first emerged in biophysics, and was later adapted to nanocatalysis by Chen and Hofkens in studying the Au and ZSM-22 catalysts respectively.⁶⁷⁻⁶⁹ By fitting the PSF of fluorescence bursts from spherical Au nanoparticles with various sizes, Chen and coworkers achieved a final resolution of 15~40 nm, which is about one magnitude higher than the diffraction limited resolution. This optical advance greatly expanded the possible application of single molecule catalysis, because small sized nanocatalysts can be chemically imaged and the activity variation such as facets, defect sites might be resolved.

Chen and coworkers used this super-resolution technique to map out the activity distribution on Au nanorods in mesoporous silica shell (Au@mSiO₂ nanorod) as well as on Au nanoplate (Au@mSiO₂ nanoplate).⁶⁷⁻⁶⁸ As a pseudo-1-D material, a Au@mSiO₂ nanorod showed a linear specific activity gradient along the length of its side facets in catalyzing an N-deacetylation reaction. Highest activity was observed in the middle of the nanorod and the activity gradually

decayed towards its two ends (Figure 1.4C, D). As a pseudo-2-D nanocatalyst, a Au@mSiO₂ nanoplate showed a radial gradient specific activity within its flat facet ($\{111\}$) in catalyzing a N-deoxygenation reaction. Highest activity was observed in the center and the activity decayed gradually toward its periphery (Figure 1.4E, F). For individual Au@mSiO₂ nanorods, the specific activity at the center of a nanorod can be a factor of ten larger than the extrapolated specific activity for perfect side facets.

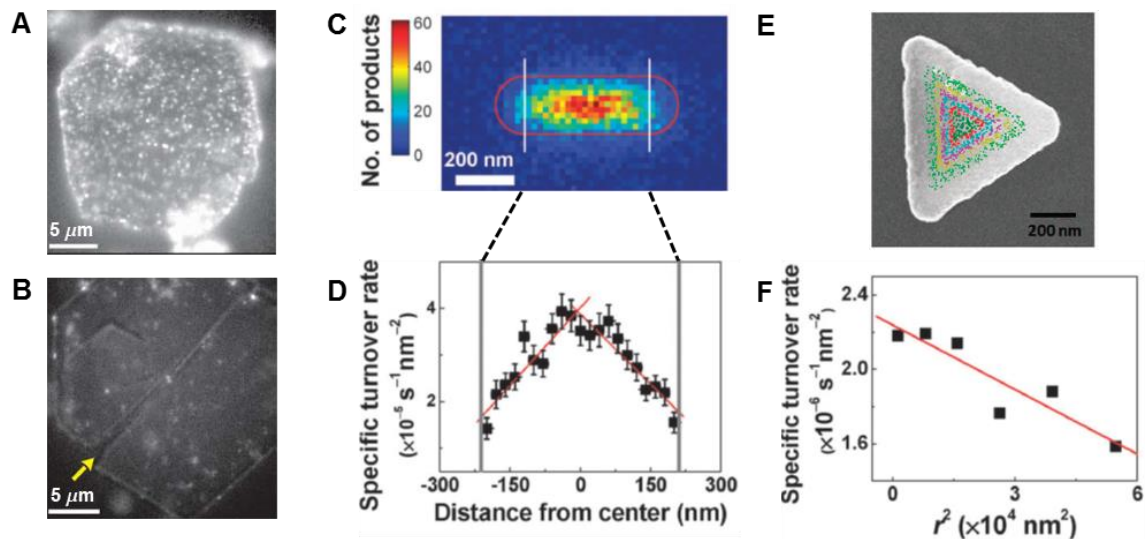


Figure 1.4 Spatially resolved activity distribution. (A) Single LDH catalyzed transesterification of C-FDA with 700 nM 1-butanol. (B) Hydrolysis of 600 nM C-FDA. (C) 2-D histogram of catalytic product locations on a single Au@mSiO₂ nanorod in catalyzing a N-deacetylation reaction. The red line is the SEM structural contour of the nanorod. The white lines separate out the two ends. (D) Dependence of the specific turnover rate on location at every ~20 nm segment along the length of the nanorod in (C). (E) Locations of product molecules overlaid on top of the SEM image of a single Au@mSiO₂ nanoplate. The product locations in different radial segments are colored differently. (F) Dependence of the specific turnover rates of radial segments on r^2 , where r is the distance along the center-to-corner vector of the nanoplate. (A) - (B) adapted from Roeffaers et al (Copyright Nature Publishing Group).²² (C) - (D) adapted from Zhou et al (Copyright Nature Publishing Group).⁶⁷ (E) - (F) adapted from Andoy et al (Copyright 2013 American Chemical Society).⁶⁸

1.6 Scope of this thesis

This dissertation focuses on studying the heterogeneous catalysis and electrochemical catalysis using fluorescence microscopy. We fully utilize its advantages in high-temporal, high-spatial resolution to dissect reaction kinetics and correlate the activity differences with structure.

Chapter 2 focuses on the chemical catalysis by nanoscale particles. Detecting and characterizing reaction intermediates is important and powerful for elucidating reaction mechanisms, but challenging in general because of the low populations of intermediates in a reaction mixture. Studying surface reaction intermediates in heterogeneous catalysis presents additional challenges, especially the ubiquitous structural heterogeneity among the catalyst particles and the accompanying polydispersion in reaction kinetics. In chapter 2, we use single-molecule fluorescence microscopy to study the oxidative deacetylation of amplex red by H_2O_2 catalyzed by two complementary types of Au nanocatalysts — mesoporous-silica-coated Au nanorods (i.e., Au@mSiO_2 nanorods) and bare 5.3 nm pseudospherical Au nanoparticles — at the single-particle, single-turnover resolution. For both nanocatalysts, the distributions of the microscopic reaction time from a single catalyst particle clearly reveal a kinetic intermediate, which is hidden when the data are averaged over many particles or only the time-averaged turnover rates are examined for a single particle. Detailed single-molecule kinetic analysis leads to a quantitative reaction mechanism and supports that the intermediate is likely a surface-adsorbed one-electron-oxidized amplex red radical. The quantitation of kinetic parameters further allows for the evaluation of the large reactivity inhomogeneity among the individual nanorods and pseudospherical nanoparticles, and for Au@mSiO_2 nanorods, it uncovers their size-dependent reactivity in catalyzing the first one-electron oxidation of amplex red to the radical. Such single-particle, single-molecule kinetic studies are expected to be broadly useful for dissecting reaction kinetics and mechanisms.

In Chapter 3, the spatial resolution of fluorescence microscopy was used to study the electrochemical activity of graphene oxide (GO). A fluorogenic electrocatalytic reaction was designed to probe the activity of individual GO sheets supported on transparent conducting ITO electrodes. By imaging the fluorescence, thus the electrocatalytic activity using fluorescence microscopy, the activity distribution on GO sheets was mapped out. This fluorescence approach enabled the imaging of GO sheets and resolving their fine features, including boundaries, wrinkles and folded regions. By further manipulating their activity with prior electrochemical reduction, domains within individual GO sheets were differentiated. The division lines between neighboring domains were mapped out as well, and they possibly reflected the grain boundaries. The electrochemical reduction of GO was further studied by sequential reduction. Localized reduction centers were observed, which preferentially existed within wrinkles and boundaries.

Chapter 4 discusses the aligned arrays of single-walled carbon nanotubes. This is an extension of previous single-molecule electrochemistry on SWNTs.²⁵ With etched position markers on quartz substrate, the spatially resolved active sites with sub-diffraction resolution were correlated with the AFM and SEM images. It is known that large reactivity heterogeneity existed among SWNTs. However it is unclear whether multiple active sites can occur on the same nanotube and whether multiple active sites from the same nanotube behave differently. In Chapter 4, the substrate concentration and driving force dependence of reactivity were studied in the spatially resolved fashion.

1.7 References

1. Ertl, G.; Knözinger, H.; Weitkamp, J., *Handbook of heterogeneous catalysis*. VCH: 1997.
2. Bell, A. T., The Impact of Nanoscience on Heterogeneous Catalysis. *Science* **2003**, *299* (5613), 1688-1691.
3. Heiz, U.; Landman, U., *Nanocatalysis*. Springer: 2007.
4. Somorjai, G. A.; Contreras, A. M.; Montano, M.; Rioux, R. M., Clusters, surfaces, and catalysis. *Proceedings of the National Academy of Sciences* **2006**, *103* (28), 10577-10583.
5. Crooks, R. M.; Zhao, M.; Sun, L.; Chechik, V.; Yeung, L. K., Dendrimer-Encapsulated Metal Nanoparticles: Synthesis, Characterization, and Applications to Catalysis. *Accounts of Chemical Research* **2000**, *34* (3), 181-190.
6. Chen, M.; Goodman, D. W., Catalytically Active Gold: From Nanoparticles to Ultrathin Films. *Accounts of Chemical Research* **2006**, *39* (10), 739-746.
7. Hughes, M. D.; Xu, Y.-J.; Jenkins, P.; McMorn, P.; Landon, P.; Enache, D. I.; Carley, A. F.; Attard, G. A.; Hutchings, G. J.; King, F.; Stitt, E. H.; Johnston, P.; Griffin, K.; Kiely, C. J., Tunable gold catalysts for selective hydrocarbon oxidation under mild conditions. *Nature* **2005**, *437* (7062), 1132-1135.
8. Lee, H.; Habas, S. E.; Kweskin, S.; Butcher, D.; Somorjai, G. A.; Yang, P., Morphological Control of Catalytically Active Platinum Nanocrystals. *Angewandte Chemie* **2006**, *118* (46), 7988-7992.
9. Jaramillo, T. F.; Jørgensen, K. P.; Bonde, J.; Nielsen, J. H.; Horch, S.; Chorkendorff, I., Identification of Active Edge Sites for Electrochemical H₂ Evolution from MoS₂ Nanocatalysts. *Science* **2007**, *317* (5834), 100-102.
10. Hansen, P. L.; Wagner, J. B.; Helveg, S.; Rostrup-Nielsen, J. R.; Clausen, B. S.; Topsøe, H., Atom-Resolved Imaging of Dynamic Shape Changes in Supported Copper Nanocrystals. *Science* **2002**, *295* (5562), 2053-2055.
11. Newton, M. A.; Belver-Coldeira, C.; Martinez-Arias, A.; Fernandez-Garcia, M., Dynamic in situ observation of rapid size and shape change of supported Pd nanoparticles during CO/NO cycling. *Nat Mater* **2007**, *6* (7), 528-532.
12. Kamat, P. V., Meeting the Clean Energy Demand: Nanostructure Architectures for Solar Energy Conversion. *The Journal of Physical Chemistry C* **2007**, *111* (7), 2834-2860.
13. Burda, C.; Chen, X.; Narayanan, R.; El-Sayed, M. A., Chemistry and Properties of Nanocrystals of Different Shapes. *Chemical Reviews* **2005**, *105* (4), 1025-1102.
14. Somorjai, G. A.; Li, Y., *Introduction to Surface Chemistry and Catalysis*. John Wiley & Sons: 2010.
15. Xia, Y.; Xiong, Y.; Lim, B.; Skrabalak, S. E., Shape-Controlled Synthesis of Metal

Nanocrystals: Simple Chemistry Meets Complex Physics? *Angewandte Chemie International Edition* **2009**, *48* (1), 60-103.

16. Xu, W.; Kong, J. S.; Yeh, Y.-T. E.; Chen, P., Single-molecule nanocatalysis reveals heterogeneous reaction pathways and catalytic dynamics. *Nature Materials* **2008**, *7* (12), 992-996.

17. Xu, W.; Kong, J. S.; Chen, P., Single-Molecule Kinetic Theory of Heterogeneous and Enzyme Catalysis. *The Journal of Physical Chemistry C* **2009**, *113* (6), 2393-2404.

18. Xu, W.; Kong, J. S.; Chen, P., Probing the catalytic activity and heterogeneity of Au-nanoparticles at the single-molecule level. *Physical Chemistry Chemical Physics* **2009**, *11* (15), 2767.

19. Chen, P., Single-nanoparticle catalysis at single-turnover resolution. *Chemical Physics Letters* **2009**, *470* (4-6), 151-157.

20. Lu, H. P.; Xun, L.; Xie, X. S., Single-Molecule Enzymatic Dynamics. *Science* **1998**, *282* (5395), 1877-1882.

21. Han, K. S.; Liu, G.; Zhou, X.; Medina, R. E.; Chen, P., How Does a Single Pt Nanocatalyst Behave in Two Different Reactions? A Single-Molecule Study. *Nano Letters* **2012**, *12* (3), 1253-1259.

22. Roeffaers, M. B. J.; Sels, B. F.; Uji-i, H.; De Schryver, F. C.; Jacobs, P. A.; De Vos, D. E.; Hofkens, J., Spatially resolved observation of crystal-face-dependent catalysis by single turnover counting. *Nature* **2006**, *439* (7076), 572-575.

23. Sakamoto, M.; Tachikawa, T.; Fujitsuka, M.; Majima, T., Photoreactivity of As-Fabricated Au Clusters at the Single-Cluster Level. *Journal of the American Chemical Society* **2008**, *131* (1), 6-7.

24. Tachikawa, T.; Majima, T., Exploring the Spatial Distribution and Transport Behavior of Charge Carriers in a Single Titania Nanowire. *Journal of the American Chemical Society* **2009**, *131* (24), 8485-8495.

25. Xu, W.; Shen, H.; Kim, Y. J.; Zhou, X.; Liu, G.; Park, J.; Chen, P., Single-Molecule Electrocatalysis by Single-Walled Carbon Nanotubes. *Nano Letters* **2009**, *9* (12), 3968-3973.

26. Cordes, T.; Blum, S. A., Opportunities and challenges in single-molecule and single-particle fluorescence microscopy for mechanistic studies of chemical reactions. *Nat Chem* **2013**, *5* (12), 993-999.

27. Kiel, A.; Kovacs, J.; Mokhir, A.; Krämer, R.; Herten, D.-P., Direct Monitoring of Formation and Dissociation of Individual Metal Complexes by Single-Molecule Fluorescence Spectroscopy. *Angewandte Chemie International Edition* **2007**, *46* (27), 5049-5049.

28. Jung, G.; Schmitt, A.; Jacob, M.; Hinkeldey, B., Fluorescent Probes for Chemical Transformations on the Single-Molecule Level. *Annals of the New York Academy of Sciences* **2008**, *1130* (1), 131-137.

29. Esfandiari, N. M.; Blum, S. A., Homogeneous vs Heterogeneous Polymerization Catalysis

Revealed by Single-Particle Fluorescence Microscopy. *Journal of the American Chemical Society* **2011**, *133* (45), 18145-18147.

30. Smiley, R. D.; Hammes, G. G., Single Molecule Studies of Enzyme Mechanisms. *Chemical Reviews* **2006**, *106* (8), 3080-3094.

31. Craig, D. B.; Arriaga, E. A.; Wong, J. C. Y.; Lu, H.; Dovichi, N. J., Studies on Single Alkaline Phosphatase Molecules: Reaction Rate and Activation Energy of a Reaction Catalyzed by a Single Molecule and the Effect of Thermal DenaturationThe Death of an Enzyme. *Journal of the American Chemical Society* **1996**, *118* (22), 5245-5253.

32. Shi, J.; Dertouzos, J.; Gafni, A.; Steel, D.; Palfey, B. A., Single-molecule kinetics reveals signatures of half-sites reactivity in dihydroorotate dehydrogenase A catalysis. *Proceedings of the National Academy of Sciences* **2006**, *103* (15), 5775-5780.

33. Engelkamp, H.; Hatzakis, N. S.; Hofkens, J.; De Schryver, F. C.; Nolte, R. J. M.; Rowan, A. E., Do enzymes sleep and work? *Chemical Communications* **2006**, (9), 935-940.

34. Xie, S., Single-Molecule Approach to Enzymology. *Single Molecules* **2001**, *2* (4), 229-236.

35. Antikainen, N. M.; Smiley, R. D.; Benkovic, S. J.; Hammes, G. G., Conformation Coupled Enzyme Catalysis: Single-Molecule and Transient Kinetics Investigation of Dihydrofolate Reductase†. *Biochemistry* **2005**, *44* (51), 16835-16843.

36. Palmer, T., *Understanding enzymes*. E. Horwood: 1991.

37. Kou, S. C.; Cherayil, B. J.; Min, W.; English, B. P.; Xie, X. S., Single-Molecule Michaelis–Menten Equations. *The Journal of Physical Chemistry B* **2005**, *109* (41), 19068-19081.

38. Min, W.; English, B. P.; Luo, G.; Cherayil, B. J.; Kou, S. C.; Xie, X. S., Fluctuating Enzymes: Lessons from Single-Molecule Studies. *Accounts of Chemical Research* **2005**, *38* (12), 923-931.

39. Min, W.; Gopich, I. V.; English, B. P.; Kou, S. C.; Xie, X. S.; Szabo, A., When Does the Michaelis–Menten Equation Hold for Fluctuating Enzymes? *The Journal of Physical Chemistry B* **2006**, *110* (41), 20093-20097.

40. Sunney Xie, X., Single-molecule approach to dispersed kinetics and dynamic disorder: Probing conformational fluctuation and enzymatic dynamics. *The Journal of Chemical Physics* **2002**, *117* (24), 11024-11032.

41. Chaudhury, S.; Cherayil, B. J., Dynamic disorder in single-molecule Michaelis-Menten kinetics: The reaction-diffusion formalism in the Wilemski-Fixman approximation. *The Journal of Chemical Physics* **2007**, *127* (10), -.

42. Xue, Q.; Yeung, E. S., Differences in the chemical reactivity of individual molecules of an enzyme. *Nature* **1995**, *373* (6516), 681-683.

43. Xu, W.; Kong, J. S.; Yeh, Y.-T. E.; Chen, P., Single-molecule nanocatalysis reveals heterogeneous reaction pathways and catalytic dynamics. *Nat Mater* **2008**, *7* (12), 992-996.

44. Naito, K.; Tachikawa, T.; Fujitsuka, M.; Majima, T., Single-Molecule Fluorescence Imaging of the Remote TiO₂ Photocatalytic Oxidation. *The Journal of Physical Chemistry B* **2005**, *109* (49), 23138-23140.
45. Xu, W.; Shen, H.; Liu, G.; Chen, P., Single-molecule kinetics of nanoparticle catalysis. *Nano Research* **2010**, *2* (12), 911-922.
46. Campbell, J. K.; Sun, L.; Crooks, R. M., Electrochemistry Using Single Carbon Nanotubes. *Journal of the American Chemical Society* **1999**, *121* (15), 3779-3780.
47. Heller, I.; Kong, J.; Heering, H. A.; Williams, K. A.; Lemay, S. G.; Dekker, C., Individual Single-Walled Carbon Nanotubes as Nanoelectrodes for Electrochemistry. *Nano Letters* **2004**, *5* (1), 137-142.
48. Heller, I.; Kong, J.; Williams, K. A.; Dekker, C.; Lemay, S. G., Electrochemistry at Single-Walled Carbon Nanotubes: The Role of Band Structure and Quantum Capacitance. *Journal of the American Chemical Society* **2006**, *128* (22), 7353-7359.
49. Roeffaers, M. B. J.; Ameloot, R.; Baruah, M.; Uji-i, H.; Bulut, M.; De Cremer, G.; Müller, U.; Jacobs, P. A.; Hofkens, J.; Sels, B. F.; De Vos, D. E., Morphology of Large ZSM-5 Crystals Unraveled by Fluorescence Microscopy. *Journal of the American Chemical Society* **2008**, *130* (17), 5763-5772.
50. Seebacher, C.; Rau, J.; Deeg, F. W.; Bräuchle, C.; Altmaier, S.; Jäger, R.; Behrens, P., Visualization of Mesostructures and Organic Guest Inclusion in Molecular Sieves with Confocal Microscopy. *Advanced Materials* **2001**, *13* (18), 1374-1377.
51. Betzig, E.; Patterson, G. H.; Sougrat, R.; Lindwasser, O. W.; Olenych, S.; Bonifacino, J. S.; Davidson, M. W.; Lippincott-Schwartz, J.; Hess, H. F., Imaging Intracellular Fluorescent Proteins at Nanometer Resolution. *Science* **2006**, *313* (5793), 1642-1645.
52. Born, M.; Wolf, E.; Bhatia, A. B., *Principles of Optics: Electromagnetic Theory of Propagation, Interference and Diffraction of Light*. Cambridge University Press: 1999.
53. Rayleigh, XXXI. Investigations in optics, with special reference to the spectroscope. *Philosophical Magazine Series 5* **1879**, *8* (49), 261-274.
54. Huang, B.; Bates, M.; Zhuang, X., Super-Resolution Fluorescence Microscopy. *Annual Review of Biochemistry* **2009**, *78* (1), 993-1016.
55. Lidke, K.; Rieger, B.; Jovin, T.; Heintzmann, R., Superresolution by localization of quantum dots using blinking statistics. *Opt. Express* **2005**, *13* (18), 7052-7062.
56. Rust, M. J.; Bates, M.; Zhuang, X., Sub-diffraction-limit imaging by stochastic optical reconstruction microscopy (STORM). *Nat Meth* **2006**, *3* (10), 793-796.
57. Thompson, R. E.; Larson, D. R.; Webb, W. W., Precise Nanometer Localization Analysis for Individual Fluorescent Probes. *Biophysical Journal* **2002**, *82* (5), 2775-2783.
58. Yildiz, A.; Selvin, P. R., Fluorescence Imaging with One Nanometer Accuracy: Application to Molecular Motors. *Accounts of Chemical Research* **2005**, *38* (7), 574-582.

59. Betzig, E.; Trautman, J. K., Near-Field Optics: Microscopy, Spectroscopy, and Surface Modification Beyond the Diffraction Limit. *Science* **1992**, *257* (5067), 189-195.
60. Hell, S. W.; Wichmann, J., Breaking the diffraction resolution limit by stimulated emission: stimulated-emission-depletion fluorescence microscopy. *Opt. Lett.* **1994**, *19* (11), 780-782.
61. Hell, S. W., Far-Field Optical Nanoscopy. *Science* **2007**, *316* (5828), 1153-1158.
62. Hell, S. W.; Kroug, M., Ground-state-depletion fluorescence microscopy: A concept for breaking the diffraction resolution limit. *Appl. Phys. B* **1995**, *60* (5), 495-497.
63. Gustafsson, M. G. L., Nonlinear structured-illumination microscopy: Wide-field fluorescence imaging with theoretically unlimited resolution. *Proceedings of the National Academy of Sciences of the United States of America* **2005**, *102* (37), 13081-13086.
64. Hess, S. T.; Girirajan, T. P. K.; Mason, M. D., Ultra-High Resolution Imaging by Fluorescence Photoactivation Localization Microscopy. *Biophysical Journal* **2006**, *91* (11), 4258-4272.
65. Cheezum, M. K.; Walker, W. F.; Guilford, W. H., Quantitative Comparison of Algorithms for Tracking Single Fluorescent Particles. *Biophysical Journal* **2001**, *81* (4), 2378-2388.
66. Gordon, M. P.; Ha, T.; Selvin, P. R., Single-molecule high-resolution imaging with photobleaching. *Proceedings of the National Academy of Sciences of the United States of America* **2004**, *101* (17), 6462-6465.
67. Zhou, X.; Andoy, N. M.; Liu, G.; Choudhary, E.; Han, K.-S.; Shen, H.; Chen, P., Quantitative super-resolution imaging uncovers reactivity patterns on single nanocatalysts. *Nat Nano* **2012**, *7* (4), 237-241.
68. Andoy, N. M.; Zhou, X.; Choudhary, E.; Shen, H.; Liu, G.; Chen, P., Single-Molecule Catalysis Mapping Quantifies Site-Specific Activity and Uncovers Radial Activity Gradient on Single 2D Nanocrystals. *Journal of the American Chemical Society* **2013**, *135* (5), 1845-1852.
69. Roeffaers, M. B. J.; De Cremer, G.; Libeert, J.; Ameloot, R.; Dedecker, P.; Bons, A.-J.; Bückins, M.; Martens, J. A.; Sels, B. F.; De Vos, D. E.; Hofkens, J., Super-Resolution Reactivity Mapping of Nanostructured Catalyst Particles. *Angewandte Chemie International Edition* **2009**, *48* (49), 9285-9289.

CHAPTER TWO

SINGLE-MOLECULE KINETICS REVEALS A HIDDEN SURFACE REACTION INTERMEDIATE IN SINGLE-NANOPARTICLE CATALYSIS

2.1 Introduction

Observing and characterizing reaction intermediates represents a powerful approach in elucidating the mechanism of chemical transformations, such as those in enzyme catalysis, homogeneous catalysis, and heterogeneous catalysis.¹⁻⁸ But trapping and detecting reaction intermediates is difficult in general because of their very nature of being intermediates — their populations in a reaction mixture are low, and they exist only transiently. Synchronization of reaction progress (e.g., via the stopped-flow technique^{9, 10}) and trapping of reactive species (e.g., via rapid-freeze quench^{11, 12} or chemical trapping^{13, 14}) are often needed to obtain an appreciable amount of the desired intermediate, so as to characterize it by spectroscopic techniques.

In heterogeneous catalysis, studying reaction intermediates presents additional challenges.^{1, 2, 5-7, 15, 16} Besides the general low population of surface-adsorbed species, the ubiquitous heterogeneity among catalyst particles gives rise to polydispersion in reaction kinetics, making synchronization more difficult. Yet it is important to know whether and how many intermediates are involved in a surface catalytic reaction, so one can determine the number of rate-limiting steps in the reaction and how one could possibly modify the catalyst to accelerate the respective reaction steps for improving the catalyst performance.

Single-molecule kinetics provides advantages in dissecting reaction steps and uncovering reaction intermediates.¹⁷⁻²⁵ By studying individual molecules/catalysts, this approach removes ensemble averaging, so dispersion in kinetics among different molecules can be circumvented.

Synchronization of molecular actions is not needed either, as it monitors one molecule at a time. It also allows for following the actions of individual molecules in real time, and at any time point, only one molecular state is present even if the molecule can adopt multiple different states; this feature is particularly useful in capturing intermediates and elucidating reaction mechanisms.

The capability of single-molecule kinetics in uncovering intermediates and elucidating mechanisms has in particular been shown in single-molecule fluorescence studies of biological molecules. For example, Lu *et al.* studied the catalysis by single cholesterol oxidases and observed an enzyme-substrate complex as a kinetic intermediate.²⁶ Others have observed kinetic intermediates in the catalysis by β -galactosidase,²⁷ α -chymotrypsin,²⁸ and nitrite reductase,²² in the DNA unwinding by nonstructural protein 3 (NS3),²⁹ and in virus fusion.³⁰

Single-molecule kinetics via fluorescence microscopy has also been achieved in studying catalysis (or reactions) by layered double hydroxides³¹, zeolites,^{32, 33} metal nanoparticles,³⁴⁻⁴¹ semiconductor nanocrystals,⁴²⁻⁴⁸ carbon nanotubes,⁴⁹ and small molecules.⁵⁰⁻⁵³ Other techniques, such as optical tweezers,^{54, 55} magnetic tweezers,⁵⁶ single-channel-recording,⁵⁷ and atomic force microscopy,⁵⁸ are also powerful in studying dynamic processes.

We have previously used single-molecule microscopy of fluorogenic reactions to study catalysis on single Au or Pt nanoparticles at the single-turnover temporal resolution and nanometer spatial precision³⁴⁻⁴⁰. In this approach, the catalyzed reaction converts a nonfluorescent reactant to a highly fluorescent product on the surface of the nanoparticles, which are dispersed at a low density and spatially separated on a slide. Under continuous laser excitation, each catalytically produced reaction product emits a large number of fluorescence photons, enabling its easy detection and imaging at the single-molecule level (as well as its position localization down to nanometer precision). By imaging this fluorescent product one molecule at a time in real time, one can follow the catalytic reactions on a single nanoparticle at the single-turnover resolution *in situ*.

Using this single-molecule microscopy approach, we examined individual mesoporous-silica-coated Au nanorods (i.e., Au@mSiO₂ nanorods) in catalyzing the fluorogenic oxidative deacetylation of amplex red (i.e., AR) to resorufin by H₂O₂.³⁸ There, by measuring the time-averaged catalytic turnover rate as a function of the reactant concentration in a spatially resolved manner, we discovered reactivity gradients along the side facets of individual nanorods, which were attributable to an underlying defect density gradient. Here we report that single-molecule kinetics further uncovers a hidden kinetic intermediate during the surface catalysis of amplex red deacetylation on single Au@mSiO₂ nanorods; the same catalytic intermediate is resolved as well on single bare 5.3 nm pseudospherical Au nanoparticles. By analyzing the distributions of the microscopic reaction time of individual catalyst particles, we have been able to resolve two rate-determining steps, quantify the rate constant of each step, provide evidences for the nature of the captured intermediate, and formulate a quantitative working mechanism for the catalytic reaction.

2.2 Materials and Methods

2.2.1 Synthesis and Characterization of Au Nano-catalysts

The 5.3 nm pseudospherical Au-nanoparticles, prepared from citrate reduction of HAuCl₄ and capped with tannic acid, was purchased from Ted Pella (JME1052). Mesoporous-silica-coated Au nanorods (i.e., Au@mSiO₂ nanorods) were prepared by making the Au nanorods first via stepwise seeded growth,⁵⁹ coating them with silica and subsequently etching the silica shell with base in the presence of CTAB to make it mesoporous,⁶⁰ as reported previously (more details in supporting information (SI)).³⁸ The Au@mSiO₂ nanorods were later calcinated at 500°C to remove the organic ligands for activation for surface catalysis, during which the Au nanorod cores maintained their morphology as examined by TEM, as we reported previously.³⁸ All samples were characterized by a FEI Tecnai 12 transmission electron microscopy (TEM) at Cornell Center for Materials Research.

2.2.2 Catalytic Reaction Conditions

The oxidative deacetylation of amplex red (AR), a nonfluorescent molecule, to resorufin, a highly fluorescent molecule, by hydrogen peroxide (H_2O_2) was studied in 50 mM pH 7.3 degassed sodium phosphate buffer. Ensemble reaction measurements were done via monitoring the fluorescence of the reaction product resorufin (excited at 532 nm and detected at 585 nm) using a Varian Cary Eclipse fluorometer.

2.2.3 Single-Molecule Fluorescence Microscopy

Single-molecule fluorescence measurements were performed on a homebuilt prism-type total internal reflection fluorescence (TIRF) microscope based on an Olympus IX71 inverted microscope as previously described.³⁴⁻³⁷ 5-6 mW continuous-wave circularly polarized 532 nm laser (CrystaLaser, GCL-025-L-0.5%) was focused onto an area of $\sim 80 \times 40 \mu\text{m}^2$ in a microfluidic reactor cell to directly excite the fluorescence of the product resorufin generated on immobilized nanocatalysts. The fluorescence of resorufin was collected by a 60 \times NA 1.2 water-immersion objective (UPLSAPO60XW, Olympus), filtered by two filters (HQ550LP, HQ580m60), and projected onto a camera (Andor iXon EMCCD) controlled by the Andor IQ software. The time resolution of image acquisition was 25 ms.

The microfluidic reactor, about 100 μm (height) \times 2 cm (length) \times 5 mm (width), was assembled using double-sided tapes sandwiched between a quartz slide (Technical Glass) and a borosilicate coverslip (Gold Seal). The quartz slide was amine-functionalized by an aminoalkylsiloxane reagent (Vectabond, Vector Laboratory) to have a positive charged surface to immobilize the negatively charged 5.3 nm Au nanoparticles. As for the Au@mSiO₂ nanorods, they were drop casted on the quartz slide. The reactant solution was flowed in continuously at 25 $\mu\text{L min}^{-1}$, maintaining nonequilibrium steady-state reaction kinetics.

2.2.4 Scanning Electron Microscopy (SEM)

The microfluidic reactor used for the fluorescence microscopy measurements was subsequently disassembled for characterizing the nanoparticles on the slide under a LEO 1550VP FESEM (operated at 2-5 keV). A carbon film of ~10 nm was coated on the quartz slide before the SEM measurements.

2.3 Results and Discussion

2.3.1 Catalytic Reaction and Catalysts

We studied the catalyzed oxidative deacetylation of amplex red (AR) by H_2O_2 to generate resorufin and acetate (Figure 2.1A).³⁷ The product resorufin is highly fluorescent, allowing for its single-molecule fluorescence imaging.

We studied two types of Au nanocatalysts: mesoporous-silica-coated Au nanorods (i.e., Au@mSiO₂ nanorods) and “bare” pseudospherical 5.3 ± 0.7 nm Au nanoparticles (Figure 2.1B and C, and SI Figure S2.1; here “bare” refers to that the particles have weak surface ligands, e.g., citrate or tannic acid, which can be readily washed off).

These two types of Au nanocatalysts are complementary model catalysts. The Au nanorods are pseudo-1-D nanocatalysts with defined surface facets (e.g., their side facets are {110} and {100}).^{61, 62} The Au nanorod cores have monodisperse diameters (21.4 ± 3.2 nm), but their lengths are variable (from ~100 nm to 600-700 nm);³⁸ and they are large enough to be imaged readily under SEM (SI Figure S2.2) to be correlated with optical microscopy using the same sample preparation (i.e., dispersed on quartz slides). The mSiO₂ shell (~80 nm in thickness) here was necessary for removing through calcination the capping ligands that were used in synthesizing these nanorods while maintaining their morphology and preventing aggregation. The mesopores here are large enough for reactants to access the gold surface, and the catalytic kinetics is not limited by mass transport of reactants, as we reported.^{38, 39} The mSiO₂ shell also helps temporarily trap the product

resorufin, facilitating its single-molecule fluorescence detection, before it desorbs, diffuses into surrounding solution, and gets carried away by the solution flow.

On the other hand, the 5.3 nm pseudospherical Au nanoparticles are pseudo-0-D nanocatalysts with many types of surface facets, which are hard to define. Their small sizes also make them harder to image by SEM. But, these pseudospherical particles can be prepared without using strong capping ligands, removing the need for the mSiO₂ encapsulation.

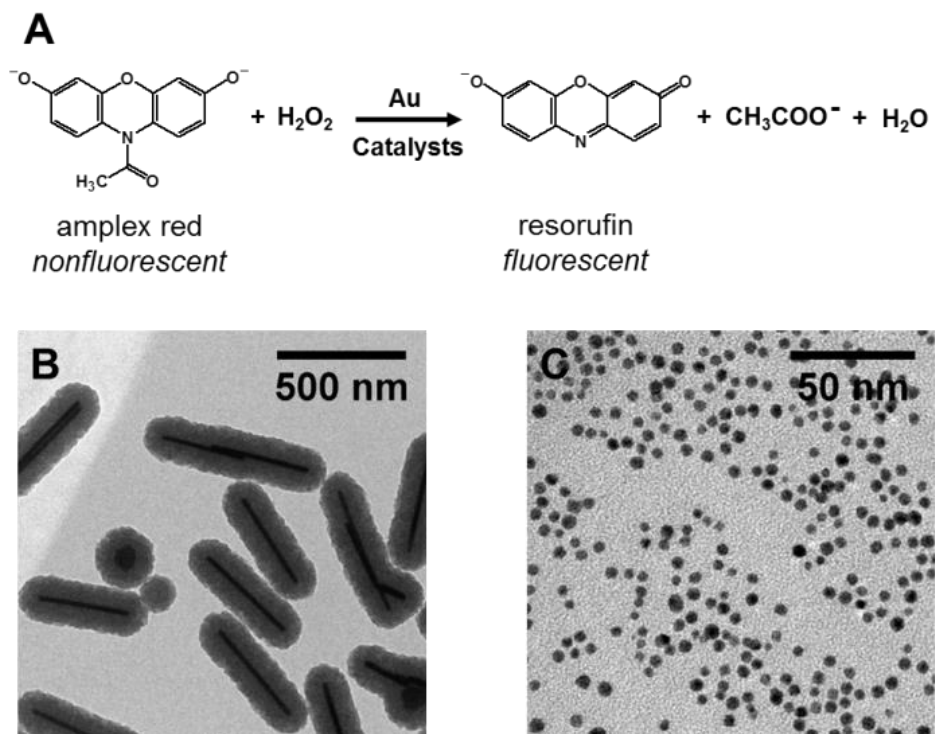


Figure 2.1 (A) Balanced chemical equation of the Au-nanoparticle-catalyzed oxidative N-deacetylation of amplex red by H₂O₂, generating resorufin, acetate, and water. (B, C) TEM images of Au@mSiO₂ nanorods (B) and 5.3 nm pseudospherical Au nanoparticles (C).

2.3.2 Single-turnover Kinetics of Single Au@mSiO₂ Nanorods Reveals a Reaction Intermediate

Figure 2.2A shows an exemplary fluorescence intensity versus time trajectory from a single immobilized Au@mSiO₂ nanorod in catalyzing the oxidative deacetylation of amplex red to resorufin by H₂O₂. The reactants were kept at constant concentrations and supplied continuously via a flow, giving steady-state reaction kinetics. This trajectory features stochastic fluorescence intensity bursts over a constant background emission of the Au nanorod; each burst reports the generation of a fluorescent product molecule resorufin. These bursts each typically last for ~50 - 100 ms (SI Figure S2.3), before the product desorbs, diffuses out of the laser excitation volume, and gets carried away by the solution flow; the times (τ) between the bursts are the microscopic reaction times for catalytic product generation. These τ 's are probabilistic in their individual values, but their statistical properties, such as averages and distributions, are defined by the underlying reaction kinetics.^{63, 64}

Figures 2.2B-D show the distributions of τ from a single Au@mSiO₂ nanorod at various amplex red concentrations (i.e., [AR]) while the H₂O₂ concentration was kept at large excess. (The catalytic activities of these Au@mSiO₂ nanorods were sufficiently stable so that each nanorod could be studied over a range of [AR] over a period of many hours.³⁸ Strikingly, the distributions of τ show an initial-rise-and-then-decay behavior with a delayed maximum at $\tau > 0$ (especially clear at [AR] = 0.05 μ M, Figure 2.2B), in contrast to the typical single-exponential decay behavior for single-molecule kinetics that contains just one rate-determining step.^{18, 63, 65-67} This initial-rise-and-then-decay behavior of τ distributions indicates that the catalytic kinetics in forming the fluorescent product contains at least two sequential rate-determining steps — i.e., there is a hidden kinetic intermediate.^{21, 26, 63} Similar behaviors of τ distributions were also observed in the single-molecule kinetics of some enzyme reactions that contain kinetic intermediates.^{21, 26-30} It is important to note that this initial-rise-and-then-decay behavior of τ distributions could *not* be reliably discerned when

τ 's from many nanorods are compiled because of the polydispersion in kinetics among the individual nanorods (SI Figure S2.4); therefore, even at the single-turnover resolution, measurements at the single-particle level were also essential in unmasking the kinetic signature of this intermediate.

The distributions of τ from single Au@mSiO₂ nanorods can each be fitted by an empirical equation of a combination of two exponentials:

$$y = A(e^{-k_1\tau} - e^{-k_2\tau}) \quad (2.1)$$

where k_1 and k_2 are the apparent rate constants for the two rate-determining steps straddling the kinetic intermediate (see later and SI Section 2.6.4 for derivation of this functional form of the τ distribution), and A is a scaling factor. Interestingly, in examining the results across a range of [AR], we find that k_1 is dependent on [AR]: it increases with increasing [AR] and eventually saturates (Figure 2.2E); this dependence indicates that the associated rate-determining step involves the reactant amplex red. In contrast, k_2 is virtually independent of [AR] (Figure 2.2F), indicating that the associated rate-determining step does not involve amplex red. Moreover, k_2 is in general an order of magnitude larger than k_1 across different [AR]. These trends of k_1 and k_2 versus [AR] persist, regardless of whether individual Au@mSiO₂ nanorods are examined or k_1 and k_2 are averaged over many nanorods (Figures 2.2E-F).

The single-turnover kinetics also readily gives the conventional rate of turnovers (ν , in s⁻¹ particle⁻¹) for a single Au@mSiO₂ nanorod, which is equivalent to $\langle \tau \rangle^{-1}$, where $\langle \rangle$ denotes averaging. With increasing [AR], the single-particle rate of turnovers $\langle \tau \rangle^{-1}$ shows typical saturation kinetics, regardless if the data are from a single Au@mSiO₂ nanorod or averaged over many nanorods (Figure 2.2G). These saturation kinetics of $\langle \tau \rangle^{-1}$ *alone* can be well accounted for by the classic Langmuir-Hinshelwood mechanism for surface catalysis⁶⁸ involving surface adsorbed amplex red molecules, without the need of invoking an intermediate in the catalytic kinetics, as we previously showed.^{34, 36-38} In other words, the conventional titration of turnover rate vs. reactant

concentration is insensitive here to the presence of this intermediate. This insensitivity again highlights the capability of single-turnover resolution kinetics to produce the distribution of the microscopic reaction time τ to unmask kinetic intermediates.

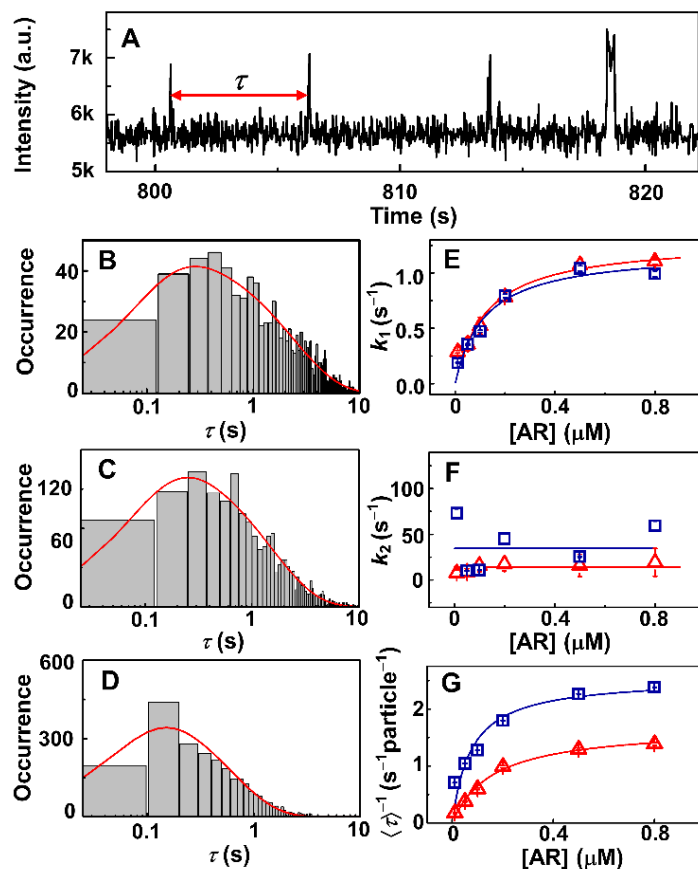


Figure 2.2 Single Au@mSiO₂ nanorod catalysis. (A) Fluorescence intensity versus time trajectory of a single Au@mSiO₂ nanorod in catalyzing the oxidative deacetylation of amplex red at [AR] = 0.05 μM and [H₂O₂] = 60 mM. (B, C, D) Distributions of τ from a single Au@mSiO₂ nanorod at [AR] = 0.05 μM (B), 0.1 μM (C) and 0.5 μM (D), respectively. H₂O₂ concentration was kept at 60 mM. Solid red lines are empirical fits with $= A \cdot (e^{-k_1\tau} - e^{-k_2\tau})$ (Equation (2.1)). (E, F) Dependences of the apparent rate constant k_1 and k_2 on [AR] for the same Au@mSiO₂ nanorod in B-D (red triangles) and when averaged over 257 nanorods (blue squares). Solid lines are fits with Equations (2.3) and (2.4) at the limiting condition of $[H] \rightarrow \infty$, where $\frac{G_B^{1/2}[H]^{1/2}}{1+G_B^{1/2}[H]^{1/2}} \rightarrow 1$. (G) Dependence of $\langle\tau\rangle^{-1}$ on [AR] for the same Au@mSiO₂ nanorod in B-D (red triangles) and when averaged over 257 nanorods (blue squares). Solid lines are fits with Equation (2.5) at the limiting condition of $\gamma_{\text{eff}2} \gg \gamma_{\text{eff}1}$. Error bars in E, F and G are all s.e.m.

2.3.3 Single-turnover Kinetics of Single 5.3 nm Pseudospherical Bare Au Nanoparticles Again Reveals a Reaction Intermediate

To probe if the observed kinetic intermediate is unique to Au@mSiO₂ nanorods or is somehow related to the presence of its mSiO₂ shell, we further studied bare pseudospherical Au nanoparticles of 5.3 nm in diameter. Figure 2.3A shows an exemplary fluorescence intensity versus time trajectory from a single 5.3 nm Au nanoparticle in catalyzing the deacetylation of amplex red by H₂O₂. This trajectory exhibits the characteristic intensity bursts reporting the generation of the fluorescent product molecule resorufin, similarly as in Figure 2.2A. The distribution of the microscopic reaction time τ from a single particle also shows a clear initial-rise-and-then-decay behavior (Figure 2.3B-C), indicating the presence of a hidden reaction intermediate straddled by two rate-determining steps in converting amplex red to the product resorufin. Again, this initial-rise-and-then-decay behavior is masked when the τ 's from many particles are compiled together (SI Figure S2.5), further stressing the importance of having both single-particle and single-turnover level resolution in measuring kinetics here.

Compared with the Au@mSiO₂ nanorods, these 5.3 nm Au nanoparticles do not have the mSiO₂ shell, and the product resorufin is detected while it is temporarily adsorbed on the particle surface. Therefore, the persistent observation of a hidden kinetic intermediate indicates that this intermediate stems from the catalytic process on the Au surface and is unrelated to the presence or not of a mSiO₂ shell.

The distribution of τ for a single 5.3 nm Au nanoparticle here again can be satisfactorily fitted by Equation (2.1), where k_1 and k_2 are the apparent rate constants of the two rate-determining steps (Figure 2.3B-C). We further studied many 5.3 nm Au nanoparticles across a range of [AR] while [H₂O₂] was kept at large excess. (Note that due to particle inactivation that becomes significant after 2 hours, we could not study the same set of 5.3 nm Au nanoparticles over the entire range of [AR]; instead, a different set of particles were studied at each [AR] within a <2 hour time window.)

Once averaged over the many Au nanoparticles, the extracted k_1 shows a clear dependence on [AR]: it increases with increasing [AR] until saturation (Figure 2.3D), whereas k_2 is essentially independent of [AR] (Figure 2.3E); both trends are similar to those for Au@mSiO₂ nanorods (Figure 2.2E, F).

$\langle \tau \rangle^{-1}$, the single-particle rate of turnovers, for the 5.3 nm Au nanoparticles shows the typical saturation kinetics with increasing [AR] for surface-mediated catalysis (Figure 2.3F), similar to that of Au@mSiO₂ nanorods (Figure 2.2G). Again, this saturation kinetics of $\langle \tau \rangle^{-1}$ is insensitive to the presence of the kinetic intermediate that is unmasked by the distribution of τ in Figure 2.3B-C.

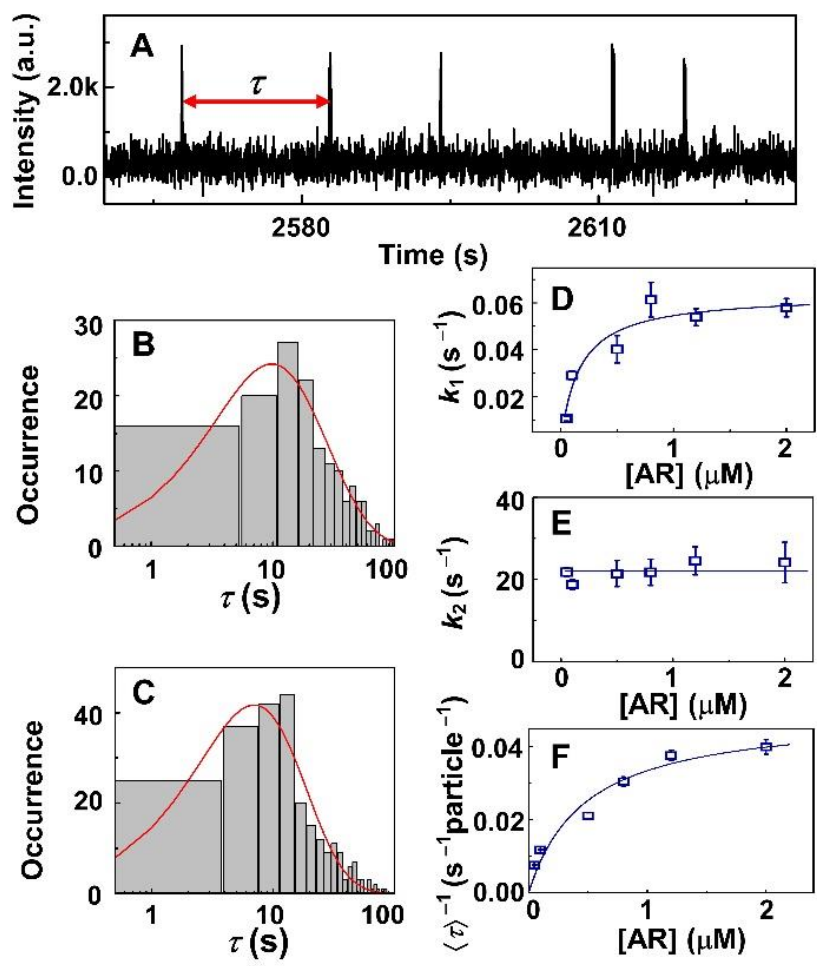


Figure 2.3 Single 5.3 nm pseudospherical Au nanoparticle catalysis. (A) Fluorescence intensity versus time trajectory of a single 5.3 nm pseudospherical Au nanoparticle under catalysis at $[AR] = 2 \mu\text{M}$ and $[\text{H}_2\text{O}_2] = 60 \text{ mM}$. (B, C) Distributions of τ from two 5.3 nm Au nanoparticles when $[AR]$ was $0.8 \mu\text{M}$ (B) and $2 \mu\text{M}$ (C), respectively. H_2O_2 concentration was kept at 60 mM . Solid lines are fits with $y = A \cdot (e^{-k_1\tau} - e^{-k_2\tau})$ (Equation (2.1)). (D, E) Dependences of the apparent rate constants k_1 and k_2 on $[AR]$; each data point is an average from ~ 90 nanoparticles. Solid lines are fits as those in Figure 2.2E-F. (F) Dependence of $\langle\tau\rangle^{-1}$ on $[AR]$; data averaged over ~ 570 nanoparticles. $[\text{H}_2\text{O}_2]$ was kept at 60 mM . Solid line is a fit as those in Figure 2.2G. Error bars in D-F are all s.e.m.

2.3.4 Mechanism of Catalysis

The single-turnover kinetics of single Au@mSiO₂ nanorods and single 5.3 nm Au nanoparticles above show that the surface-catalyzed oxidative deacetylation of amplex red by H₂O₂ involves a kinetic intermediate straddled by two rate-determining steps (Figures 2.2B-D and 2.3B-C). The kinetics of one of the two steps is dependent on [AR], whereas the other is independent (Figures 2.2E-F and 2.3D-E). The catalysis also directly involves surface-adsorbed amplex red molecules, as evidenced by the saturation behavior of the single-particle turnover rate $\langle \tau \rangle^{-1}$ vs. [AR] (Figures 2.2G and 2.3F).

Unfortunately, titrating [H₂O₂] in single-molecule imaging of single-nanoparticle catalysis is unreliable: the concentration of dilute H₂O₂ solutions is unstable, but the single-nanoparticle catalysis measurements need a long observation time (>1 h) to observe a sufficient number of catalytic turnovers per particle for accumulating statistics on τ . Nevertheless, we performed titration of the catalytic reaction rate vs. [H₂O₂] at the ensemble level, using 5.3 nm pseudospherical Au nanoparticles as a representative because they are less inhomogeneous in size (Figure 2.1C) (the Au@mSiO₂ nanorod sample contains a mixture of pseudospherical particles and nanorods, which are more problematic for ensemble-averaged measurements; Figure 2.1B and SI Figure S2.1C). The reaction rate shows saturation kinetics with increasing [H₂O₂] (Figure 2.4A), supporting that the catalysis involves adsorption of H₂O₂ onto the particle surfaces.

To account mechanistically for the observed single-turnover catalytic kinetics of Au@mSiO₂ nanorods and 5.3 nm Au nanoparticles, we first considered the following reaction sequence for the surface-catalyzed oxidative deacetylation of amplex red to resorufin by H₂O₂ (Scheme 2.1, and SI Section 2.6.4). This catalyzed reaction has overall a 1:1 reaction stoichiometry between amplex red and H₂O₂, as we determined previously (Figure 2.1A)³⁷, and for amplex red, it is overall a two-electron oxidation reaction.

In this overall reaction sequence (Scheme 2.1), the two reactants first adsorb reversibly to the Au surface (step *i*). The adsorbed H₂O₂ can undergo a reversible hemolytic O–O bond cleavage to generate surface-bound OH• radicals (step *ii*). Then the reaction proceeds via a one-electron oxidation of amplex red by a surface-bound OH• radical, generating a radical species AR• (step *iii*). A subsequent 2nd electron oxidation generates the product resorufin (step *iv*). The deacetylation of amplex red could be accompanying the 1st or the 2nd oxidation step, or occur as a separate step that is not explicitly included here, and both or either step can be coupled with proton transfer as well.

It is known that Au surface can catalyze H₂O₂ decomposition to form OH• radicals,⁶⁹⁻⁷⁴ and this reaction is reversible.⁷⁴ To test the involvement of OH• radical in the reaction pathway, we examined the effect of DMSO, a known effective scavenger of OH• radicals,⁷⁵⁻⁸⁰ on the catalytic kinetics at the ensemble level, again using 5.3 nm Au nanoparticles as the representative. The catalytic reaction rate is strongly quenched by DMSO in the solution (Figure 2.4B), consistent with the involvement of OH• radical in the reaction pathway. The involvement of the AR• radical in the oxidation of amplex red to form resorufin has been described in the catalysis by the enzyme horseradish peroxidase.⁸¹⁻⁸³

Our previous studies on small (≤ 15 nm in diameter) bare Au nanoparticles in catalyzing a different reductive reaction³⁴⁻³⁶ and the current results on 5.3 nm Au nanoparticles show that we could directly detect the fluorescence of the product resorufin on their surfaces. For Au@mSiO₂ nanorods, the generated resorufin on the Au nanorod surface could *potentially* be fluorescently quenched due to the proximity to the Au surface, before desorbing from Au nanorod surface and getting temporarily trapped in the mSiO₂ shell. Regardless, this fluorescence-quenched state of the product cannot be the observed kinetic intermediate, as the intermediate is still present for the bare 5.3 nm Au nanoparticles.

In Scheme 2.1, step *i* can be assumed to follow a fast adsorption-desorption equilibrium, in which amplex red and H₂O₂ each follow a Langmuir adsorption behavior onto different types of surface sites, which would be consistent with the saturation kinetics observed with increasing reactant concentrations. The two rate-determining steps observed experimentally should come from the remaining three reaction steps (i.e., steps *ii*, *iii*, and *iv*), involving two possible reaction intermediates: the surface-adsorbed OH• radical or the surface-adsorbed one-electron-oxidized amplex red radical AR•.

The OH• radical being the observed kinetic intermediate is significantly disfavored for two reasons (see SI Section 2.6.4.2 for details): (1) Based on the measurements of Lunsford *et al.*,⁷⁴ the O–O bond cleavage rate of H₂O₂ to generate OH• on Au surfaces is estimated to be around 0.1 μmol cm⁻² s⁻¹. For Au@mSiO₂ nanorods and 5.3 nm Au nanoparticles with average surface areas of 10⁻¹⁰ cm² and 10⁻¹² cm², respectively, this O–O bond cleavage rate would correspond to 10⁷ and 10⁵ s⁻¹particle⁻¹, at least 6 orders of magnitude larger than their observed highest turnover rates at ~2 and ~0.04 s⁻¹particle⁻¹ (Figure 2.2G and Figure 2.3F). (2) The apparent rate constants of the two rate-determining steps would both be predicted to be dependent on [AR] (SI Section 2.6.4.2), which is in conflict with the results in Figures 2.2E-F and 2.3D-E where only one of the rate-determining steps is dependent on [AR]. Therefore, the AR• radical, not the OH• radical, is likely the kinetic intermediate observed, and the steps *iii* and *iv* in Scheme 2.1 are the two rate-determining steps with the apparent rate constants k_{app1} and k_{app2} , respectively.

Assuming the O–O bond cleavage of H₂O₂ to generate OH• establishes a fast equilibrium on Au surfaces, the reaction sequence in Scheme 2.1 reduces to the minimal kinetic mechanism in Scheme 2.2. The probability density function $f(\tau)$ of the microscopic reaction time τ for this simplified kinetic scheme has been derived previously^{21, 26, 63} and described in detail in SI Section 2.6.4:

$$f(\tau) = \frac{k_{\text{app1}}k_{\text{app2}}}{k_{\text{app2}}-k_{\text{app1}}}(e^{-k_{\text{app1}}\tau} - e^{-k_{\text{app2}}\tau}) \quad (2.2)$$

$f(\tau)$ contains two exponentials, behaving with an initial exponential rise followed by an exponential decay, as observed experimentally (Figures 2.2B-D and 2.3B-C). And k_{app1} and k_{app2} here correspond to k_1 and k_2 in the empirical Equation (2.1), respectively.

Using classic Langmuir-Hinshelwood kinetics for surface catalysis where AR and OH• adsorb onto different types of surface sites, we can derive that k_{app1} and k_{app2} take the following forms (see derivations in SI Section 2.6.4):

$$k_{\text{app1}} = \gamma_{\text{eff1}} \frac{G_A[A]}{1+G_A[A]} \frac{G_B^{1/2}[H]^{1/2}}{1+G_B^{1/2}[H]^{1/2}} \xrightarrow{[H] \rightarrow \infty} \gamma_{\text{eff1}} \frac{G_A[A]}{1+G_A[A]} \quad (2.3)$$

$$k_{\text{app2}} = \gamma_{\text{eff2}} \frac{G_B^{1/2}[H]^{1/2}}{1+G_B^{1/2}[H]^{1/2}} \xrightarrow{[H] \rightarrow \infty} \gamma_{\text{eff2}} \quad (2.4)$$

Here G_A is the adsorption equilibrium constant of amplex red. G_B is the equilibrium constant for H_2O_2 adsorption to directly become two adsorbed OH•. $\gamma_{\text{eff1}} = \gamma_1 n_A n_B$, $\gamma_{\text{eff2}} = \gamma_2 n_B$, where γ_1 and γ_2 are two rate constants and n_A and n_B are respectively the total numbers of adsorption sites for amplex red and OH• on a particle. $[A]$ (i.e., [AR]) and $[H]$ are the solution concentrations of amplex red and H_2O_2 , respectively. Moreover, when H_2O_2 in the solution goes to saturation concentrations (e.g., at 60 mM in our experiment), $\frac{G_B^{1/2}[H]^{1/2}}{1+G_B^{1/2}[H]^{1/2}} \rightarrow 1$. Clearly, k_{app1} is dependent on $[A]$ (the amplex red concentration) — it increases with increasing $[A]$ and eventually saturates — whereas k_{app2} is independent of $[A]$, as observed experimentally for the two exponents in the distributions of τ (Figures 2.2E-F and 2.3D-E).

$\langle \tau \rangle^{-1}$, the time-averaged single-particle rate of turnovers, takes the form at saturating H_2O_2 concentrations:

$$\langle \tau \rangle^{-1} = \frac{\gamma_{\text{eff1}} G_A[A]}{1+(1+\frac{\gamma_{\text{eff1}}}{\gamma_{\text{eff2}}})G_A[A]} \xrightarrow{\gamma_{\text{eff2}} \gg \gamma_{\text{eff1}}} \frac{\gamma_{\text{eff1}} G_A[A]}{1+G_A[A]} \quad (2.5)$$

With increasing amplex red concentration, $\langle\tau\rangle^{-1}$ is predicted to show the typical saturation kinetics, consistent with experimental results (Figure 2.2G and 2.3E), and non-informative about the presence of the kinetic intermediate. The limiting form of Equation (2.5) at $\gamma_{\text{eff}2} \gg \gamma_{\text{eff}1}$ is identical to the classic Langmuir-Hinshelwood rate equation for the case there is merely one rate-determining step and no kinetic intermediate is present, which we used previously.³⁸

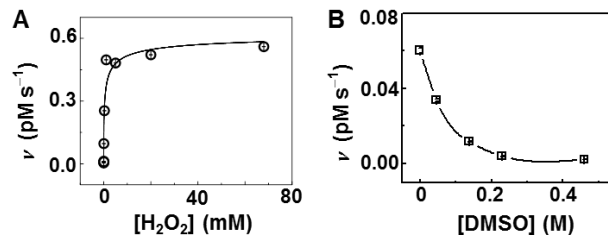
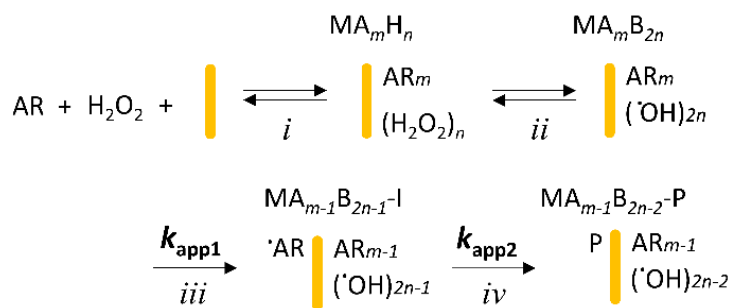


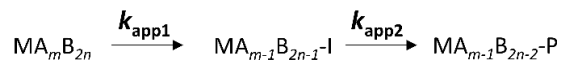
Figure 2.4 Ensemble reaction rates catalyzed by bare 5.3 nm pseudospherical Au nanoparticles. (A) Dependence on H_2O_2 concentration at $[\text{AR}] = 1 \mu\text{M}$. Solid line is a fit with $v = \frac{kG^{1/2}[\text{H}]^{1/2}}{1+G^{1/2}[\text{H}]^{1/2}}$, which is equivalent to the SI Equation S2.16 (SI Section 2.6.5) at saturating $[\text{A}]$. $[\text{H}]$ is the H_2O_2 concentration. (B) Dependence on DMSO concentration in the reaction solution at $[\text{AR}] = 10 \mu\text{M}$ and $[\text{H}_2\text{O}_2] = 50 \mu\text{M}$. Solid line is a spline connection for visual guide. All experiments here were carried out in 50 mM pH 7.3 degassed phosphate buffer with $\sim 0.44 \text{ nM}$ Au nanoparticles as the catalyst. Error bars are S.E.

Scheme 2.1 Possible reaction steps of amplex red oxidation by H_2O_2 catalyzed on Au nanoparticle surfaces ^a



^a M: Au nanocatalyst; A: amplex red; H: H_2O_2 ; B: $\text{OH}\cdot$ radical; I: intermediate $\text{AR}\cdot$; P: fluorescent product resorufin. For example, MA_mB_{2n} represents a Au nanorod/nanoparticle having m adsorbed amplex red molecules and $2n$ $\text{OH}\cdot$.

Scheme 2.2 Minimal kinetic mechanism



2.3.5 Inhomogeneity and Size-dependence of Nanocatalyst Reactivity

The formulation of the effective kinetic mechanism in Scheme 2.2 and the corresponding expressions for $f(\tau)$, k_{app1} and k_{app2} in Equations (2.2)-(2.4) allowed us to fit the experimental results to determine the kinetic parameters for each catalyst particle. For each Au@mSiO₂ nanorod, the data collected at all [AR] were globally fitted (e.g., fitting the distributions of τ in Figure 2.2B-D, or the k_1 and k_2 in Figure 2.2E-F) to obtain its γ_{eff1} ($=\gamma_1 n_A n_B$), γ_{eff2} ($=\gamma_2 n_B$), and G_A . These nanorods are sufficiently large to be easily identifiable in their SEM image (SI Figure S2.2),³⁸ from which the core length of each nanorod can be obtained using known mSiO₂ shell thickness (~80 nm, SI Section 2.6.1.3).³⁸ For each 5.3 nm Au nanoparticle, its distribution of τ at a [AR] was fitted to obtain its γ_{eff1} , γ_{eff2} , and G_A (e.g., Figure 2.3B-C).

In general, Au@mSiO₂ nanorods are more active on a per particle basis than the 5.3 nm Au nanoparticles, reflected by their ~20 times and ~2 times larger average γ_{eff1} and γ_{eff2} values, respectively (Figure 2.5A, B vs. E, F). It is not surprising, as the nanorods are much larger and thus have more surface sites per particle. The distributions of γ_{eff1} , γ_{eff2} , and G_A for the Au@mSiO₂ nanorods are all broad (Figure 2.5A, B and C), reflecting the large reactivity inhomogeneity among the individual nanorods. This large reactivity inhomogeneity is also observed among the individual 5.3 nm Au nanoparticles (Figure 2.5E, F and G). For these inhomogeneities, single-nanoparticle catalysis measurements are uniquely capable of quantifying them, for example here by the distributions of the respective kinetic parameters.

For the individual Au@mSiO₂ nanorods, the availability of their lengths from SEM also allowed for examining their size-dependent catalytic properties. Their $\gamma_{\text{eff1}} (= \gamma_1 n_A n_B)$ represents the combined reactivity of all the sites on a single nanorod in the first one-electron oxidation of AR to AR• by OH• (the first rate-determining step in Scheme 2.2); γ_{eff1} shows a clear positive correlation with the nanorod length (i.e., L ; Figure 2.5A, left), attributable to a larger number (i.e., n_A and n_B) of reactive sites on longer nanorods. However, once normalized by the nanorod length, γ_{eff1}/L decreases with increasing length (Figure 2.5D), suggesting that longer Au@mSiO₂ nanorods have smaller specific reactivity (i.e., γ_1) for the reaction of AR oxidation to AR•. In contrast, $\gamma_{\text{eff2}} (= \gamma_2 n_B)$, which represents the combined reactivity of all sites on a single nanorod for the second one-electron oxidation of AR• to P (the second rate-determining step in Scheme 2.2), shows no clear dependence on the nanorod length (Figure 2.5B, left), even though longer nanorods presumably have more reactive sites of the n_B type. This independence might result from opposite dependences of γ_2 and n_B on nanorod length, thus canceling each other. G_A , being the adsorption equilibrium constant of amplex red, does not show any clear dependence on the nanorod length, either (Figure 2.5C, left).

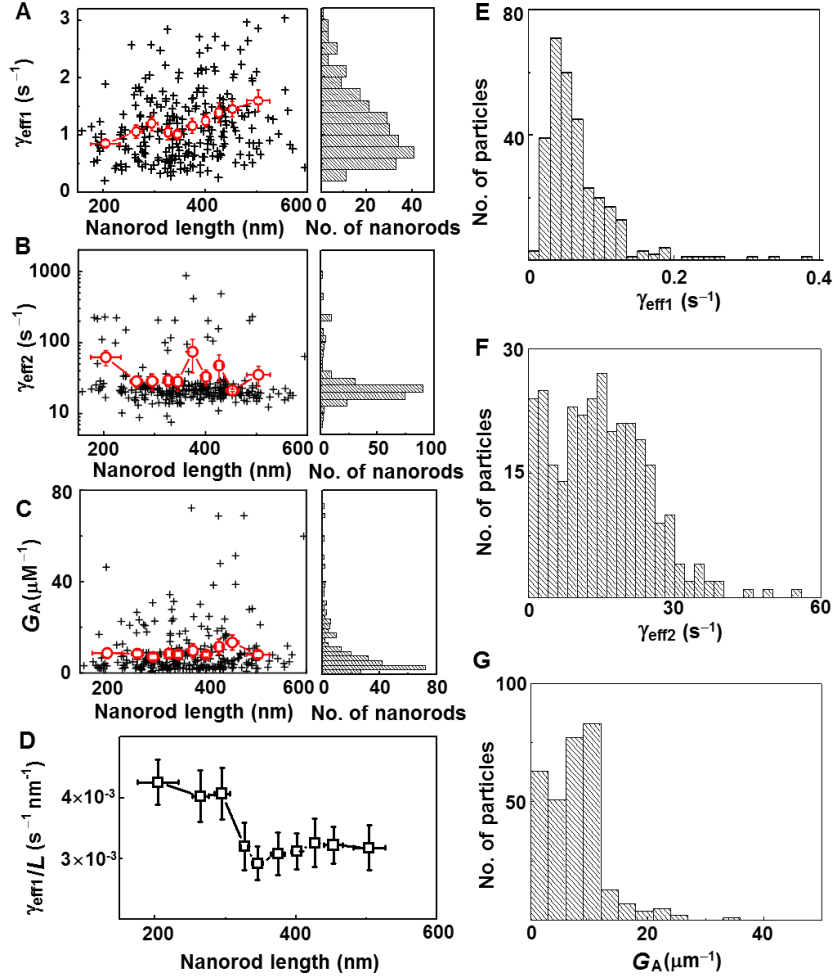


Figure 2.5 (A-C) Left: Scatter plots of γ_{eff1} , γ_{eff2} , and G_A versus the core length for individual Au@mSiO₂ nanorods. Each black cross represents one nanorod (total 257 nanorods). The nanorods are then binned every 25 nanorods according to their core length L and averaged to obtain the dependences of γ_{eff1} , γ_{eff2} , and G_A on L (red circles). Right, the corresponding histograms of γ_{eff1} , γ_{eff2} , and G_A . The averaged values are $\langle \gamma_{\text{eff1}} \rangle = 1.20 \pm 0.04 \text{ s}^{-1}$, $\langle \gamma_{\text{eff2}} \rangle = 38.4 \pm 4.7 \text{ s}^{-1}$, and $\langle G_A \rangle = 9.3 \pm 0.7 \mu\text{M}^{-1}$ (errors here are s.e.m). (D) Dependence of γ_{eff1}/L on nanorod length. Each point is an average of 25 nanorods. (E-G) Distributions of γ_{eff1} , γ_{eff2} and G_A for 5.3 nm pseudospherical Au nanoparticles. Their averaged values are $\langle \gamma_{\text{eff1}} \rangle = 0.068 \pm 0.003 \text{ s}^{-1}$, $\langle \gamma_{\text{eff2}} \rangle = 15.0 \pm 0.5 \text{ s}^{-1}$, and $\langle G_A \rangle = 8.4 \pm 0.7 \mu\text{M}^{-1}$. X error bars are s.d.; y error bars are s.e.m.

2.4 Conclusion

Using single-molecule fluorescence microscopy, we have studied the single-molecule kinetics of individual Au@mSiO₂ nanorods and bare 5.3 nm pseudospherical Au nanoparticles in catalyzing the oxidative deacetylation of amplex red to resorufin by H₂O₂. For both nanocatalysts, the distributions of the microscopic reaction time from a single catalyst particle clearly reveal a kinetic intermediate straddled by two rate-determining steps. This surface reaction intermediate is hidden when the data are averaged over many particles or only the time-averaged turnover rates are examined for a single particle, demonstrating the necessity of both single-turnover and single-particle resolution in unmasking this reaction intermediate. The kinetic (in)dependence of the two rate-determining steps on the reactant concentration allows for the formulation of a reaction mechanism that can describe quantitatively the catalytic kinetics, which, in combination with literature results, supports that the intermediate is likely a surface-adsorbed one-electron-oxidized amplex red radical. The quantitative kinetics also gives kinetic parameters of the reaction steps for each catalyst particle, allowing the evaluation of the large reactivity inhomogeneity among the individual nanorods and pseudospherical nanoparticles. Parallel SEM imaging further enables the correlation of each Au@mSiO₂ nanorod's reactivity with its length, uncovering its size-dependent reactivity in catalyzing the first one-electron oxidation of amplex red to the radical. We envision that such single-molecule kinetic studies should be broadly useful for dissecting reaction kinetics and mechanism in heterogeneous catalysis, where the catalyst heterogeneity is a ubiquitous challenge for which ensemble-averaging could mask the kinetic signatures of reaction intermediates.

2.5 References

1. Ertl, G.; Knözinger, H.; Weitkamp, J., *Handbook of heterogeneous catalysis*. VCH: 1997.
2. Following Single Molecules to a Better Understanding of Self-Assembled One-Dimensional Nanostructures. *The Journal of Physical Chemistry Letters* **2013**, 130828081634002.
3. Cook, P. F.; Cleland, W. W., *Enzyme kinetics and mechanism*. Garland Science: 2007.
4. Zaera, F., Probing catalytic reactions at surfaces. *Progress in Surface Science* **2001**, 69, 1-98.
5. Stavitski, E.; Weckhuysen, B. M., Infrared and Raman imaging of heterogeneous catalysts. *Chemical Society Reviews* **2010**, 39, 4615-4625.
6. Optical Tracking of Single Ag Clusters in Nanostructured Water Films. *The Journal of Physical Chemistry C* **2013**, 131113091254009.
7. Characterizing N-dimensional anisotropic Brownian motion by the distribution of diffusivities. *The Journal of Chemical Physics* **2013**, 139, 184105.
8. Wunder, S.; Polzer, F.; Lu, Y.; Mei, Y.; Ballauff, M., Kinetic Analysis of Catalytic Reduction of 4-Nitrophenol by Metallic Nanoparticles Immobilized in Spherical Polyelectrolyte Brushes. *The Journal of Physical Chemistry C* **2010**, 114, 8814-8820.
9. Jennings, P. A.; Wright, P. E., Formation of a Molten Globule Intermediate Early in the Kinetic Folding Pathway of Apomyoglobin. *Science* **1993**, 262, 892-896.
10. Khalifah, R. G., Carbon Dioxide Hydration Activation of Carbonic Anhydrase .1. Stop-Flow Kinetic Studies on Native Human Isoenzyme-B and Isoenzyme-C. *Journal of Biological Chemistry* **1971**, 246, 2561-&.
11. Bollinger, J. M.; Edmondson, D. E.; et al., Mechanism of Assembly of the Tyrosyl Radical-Dinuclear Iron Cluster Cofactor of Ribonucleotide Reductase. *Science* **1991**, 253, 292.
12. Licht, S.; Gerfen, G. J.; Stubbe, J. A., Thiyl radicals in ribonucleotide reductases. *Science* **1996**, 271, 477-481.
13. Cavalcanti, F. A. P.; Blackmond, D. G.; Oukaci, R.; Sayari, A.; Erdem-Senatalar, A.; Wender, I., In situ chemical trapping of COH₂ surface species. *Journal of Catalysis* **1988**, 113, 1-12.
14. Deluzarche, A.; Hindermann, J. P.; Kiennemann, A.; Kieffer, R., Application of Chemical Trapping to the Determination of Surface Species and to the Study of Their Evolution Under Reaction Conditions in Heterogeneous Catalysis. *Journal of Molecular Catalysis* **1985**, 31, 225-250.
15. Single-Molecule Study on Polymer Diffusion in a Melt State: Effect of Chain Topology. *Analytical Chemistry* **2013**, 130715150445008.

16. Single Molecules as Optical Nanoprobes for Soft and Complex Matter. *Angewandte Chemie International Edition* **2010**, 49, 854.
17. Tamarat, P.; Maali, A.; Lounis, B.; Orrit, M., Ten Years of Single-Molecule Spectroscopy. *The Journal of Physical Chemistry A* **1999**, 104, 1-16.
18. Xie, X. S.; Lu, H. P., Single-molecule Enzymology. *Journal of Biological Chemistry* **1999**, 274, 15967-15970.
19. De Cremer, G.; Sels, B. F.; De Vos, D. E.; Hofkens, J.; Roeffaers, M. B. J., Fluorescence micro(spectro)scopy as a tool to study catalytic materials in action. *Chemical Society Reviews* **2010**, 39, 4703-4717.
20. Chen, P.; Zhou, X.; Shen, H.; Andoy, N. M.; Choudhary, E.; Han, K.-S.; Liu, G.; Meng, W., Single-molecule fluorescence imaging of nanocatalytic processes. *Chemical Society Reviews* **2010**, 39, 4560.
21. Floyd, D. L.; Harrison, S. C.; van Oijen, A. M., Analysis of Kinetic Intermediates in Single-Particle Dwell-Time Distributions. *Biophysical Journal* **2010**, 99, 360-366.
22. Kulzer, F.; Xia, T.; Orrit, M., Einzelmoleküle als optische Nanosonden für weiche und komplexe Materie. *Angewandte Chemie* **2010**, 122, 866.
23. Cordes, T.; Blum, S. A., Opportunities and challenges in single-molecule and single-particle fluorescence microscopy for mechanistic studies of chemical reactions. *Nat Chem* **2013**, 5, 993-999.
24. Janssen, K. P. F.; De Cremer, G.; Neely, R. K.; Kubarev, A. V.; Van Loon, J.; Martens, J. A.; De Vos, D. E.; Roeffaers, M. B. J.; Hofkens, J., Single molecule methods for the study of catalysis: from enzymes to heterogeneous catalysts. *Chemical Society Reviews* **2014**, 43, 990-1006.
25. Somorjai, G. A.; Kliewer, C. J., Reaction selectivity in heterogeneous catalysis. *React. Kinet. Catal. Lett.* **2009**, 96, 191-208.
26. Bent, B. E., Mimicking Aspects of Heterogeneous Catalysis: Generating, Isolating, and Reacting Proposed Surface Intermediates on Single Crystals in Vacuum. *Chemical Reviews* **1996**, 96, 1361-1390.
27. English, B. P.; Min, W.; van Oijen, A. M.; Lee, K. T.; Luo, G.; Sun, H.; Cherayil, B. J.; Kou, S. C.; Xie, X. S., Ever-fluctuating single enzyme molecules: Michaelis-Menten equation revisited. *Nat Chem Biol* **2006**, 2, 87-94.
28. Terentyeva, T. G.; Hofkens, J.; Komatsuzaki, T.; Blank, K.; Li, C.-B., Time-Resolved Single Molecule Fluorescence Spectroscopy of an α -Chymotrypsin Catalyzed Reaction. *The Journal of Physical Chemistry B* **2013**, 117, 1252-1260.
29. Myong, S.; Bruno, M. M.; Pyle, A. M.; Ha, T., Spring-Loaded Mechanism of DNA Unwinding by Hepatitis C Virus NS3 Helicase. *Science* **2007**, 317, 513-516.
30. Floyd, D. L.; Ragains, J. R.; Skehel, J. J.; Harrison, S. C.; van Oijen, A. M., Single-particle kinetics of influenza virus membrane fusion. *Proceedings of the National Academy of Sciences*

2008, 105, 15382-15387.

31. Roeffaers, M. B. J.; Sels, B. F.; Uji-i, H.; De Schryver, F. C.; Jacobs, P. A.; De Vos, D. E.; Hofkens, J., Spatially resolved observation of crystal-face-dependent catalysis by single turnover counting. *Nature* **2006**, 439, 572-575.

32. Roeffaers, M.B.J; De Cremer, G.; Libeert, J.; Ameloot, R.; Dedecker, P.; Bons, A.; Bückins, M.; Martens, J.A.; Sels, B.F.; DeVos, D.E.; Hofkens, J., Super-Resolution Reactivity Mapping of Nanostructured Catalyst Particles, *J. Angew. Chem. Int. Ed.* **2009**, 48, 9285.

33. De Cremer, G.; Roeffaers, M. B. J.; Bartholomeeusen, E.; Lin, K.; Dedecker, P.; Pescarmona, P. P.; Jacobs, P. A.; De Vos, D. E.; Hofkens, J.; Sels, B. F., High-resolution Single-molecule Mapping Reveals Intraparticle Diffusion Limitation in Ti-MCM-41-catalyzed Epoxidation. *Angew. Chem. Int. Ed.* **2010**, 49, 908.

34. Xu, W.; Kong, J. S.; Yeh, Y.-T. E.; Chen, P., Single-molecule nanocatalysis reveals heterogeneous reaction pathways and catalytic dynamics. *Nat Mater* **2008**, 7, 992-996.

35. Xu, W.; Kong, J. S.; Chen, P., Probing the catalytic activity and heterogeneity of Au-nanoparticles at the single-molecule level. *Physical Chemistry Chemical Physics* **2009**, 11, 2767.

36. Xiaochun Zhou, W. X., Guokun Liu, Debashis Panda, and Peng Chen, Size-Dependent Catalytic Activity and Dynamics of Gold Nanoparticles at the Single-Molecule Level. *J. AM. CHEM. SOC.* **2010**, 132, 138-146.

37. Han, K. S.; Liu, G.; Zhou, X.; Medina, R. E.; Chen, P., How Does a Single Pt Nanocatalyst Behave in Two Different Reactions? A Single-Molecule Study. *Nano Letters* **2012**, 12, 1253-1259.

38. Zhou, X.; Andoy, N. M.; Liu, G.; Choudhary, E.; Han, K.-S.; Shen, H.; Chen, P., Quantitative super-resolution imaging uncovers reactivity patterns on single nanocatalysts. *Nat Nano* **2012**, 7, 237-241.

39. Andoy, N. M.; Zhou, X.; Choudhary, E.; Shen, H.; Liu, G.; Chen, P., Single-Molecule Catalysis Mapping Quantifies Site-Specific Activity and Uncovers Radial Activity Gradient on Single 2D Nanocrystals. *Journal of the American Chemical Society* **2013**, 135, 1845-1852.

40. Zhou, X.; Choudhary, E.; Andoy, N. M.; Zou, N.; Chen, P., Scalable Parallel Screening of Catalyst Activity at the Single-Particle Level and Subdiffraction Resolution. *ACS Catalysis* **2013**, 3, 1448-1453.

41. Wee, T.-L.; Schmidt, L. C.; Scaiano, J. C., Photooxidation of 9-Anthraldehyde Catalyzed by Gold Nanoparticles: Solution and Single Nanoparticle Studies Using Fluorescence Lifetime Imaging. *The Journal of Physical Chemistry C* **2012**, 116, 24373-24379.

42. Naito, K.; Tachikawa, T.; Fujitsuka, M.; Majima, T., Real-Time Single-Molecule Imaging of the Spatial and Temporal Distribution of Reactive Oxygen Species with Fluorescent Probes: Applications to TiO₂ Photocatalysts. *The Journal of Physical Chemistry C* **2008**, 112, 1048-1059.

43. Single molecule fluorescence microscopy investigations on heterogeneity of translational diffusion in thin polymer films. *Physical Chemistry Chemical Physics* **2011**, 13, 1770.

44. Tachikawa, T.; Yamashita, S.; Majima, T., Evidence for Crystal-Face-Dependent TiO₂ Photocatalysis from Single-Molecule Imaging and Kinetic Analysis. *Journal of the American Chemical Society* **2011**, 133, 7197-7204.
45. Heterogeneity in Single-Molecule Observables in the Study of Supercooled Liquids. *Annual Review of Physical Chemistry* **2013**, 64, 177.
46. Trajectory angle determination in one dimensional single molecule tracking data by orthogonal regression analysis. *Physical Chemistry Chemical Physics* **2011**, 13, 1827.
47. Xu, W.; Jain, P. K.; Beberwyck, B. J.; Alivisatos, A. P., Probing Redox Photocatalysis of Trapped Electrons and Holes on Single Sb-doped Titania Nanorod Surfaces. *Journal of the American Chemical Society* **2012**, 134, 3946-3949.
48. Ha, J. W.; Ruberu, T. P. A.; Han, R.; Dong, B.; Vela, J.; Fang, N., Super-Resolution Mapping of Photogenerated Electron and Hole Separation in Single Metal–Semiconductor Nanocatalysts. *Journal of the American Chemical Society* **2014**, 136, 1398-1408.
49. Weilin Xu, H. S., Yoon Ji Kim, Xiaochun Zhou, Guokun Liu, Jiwoong Park, and Peng Chen, Single-Molecule Electrocatalysis by Single-Walled Carbon Nanotubes. *Nano Letters* **2009**, 9, 3968-3973.
50. A novel method for automatic single molecule tracking of blinking molecules at low intensities. *Physical Chemistry Chemical Physics* **2013**, 15, 6196.
51. Diffusion Measurement by Monitoring Molecular Displacement. **2012**, 347.
52. Esfandiari, N. M.; Wang, Y.; Bass, J. Y.; Blum, S. A., Deconvoluting Subensemble Chemical Reaction Kinetics of Platinum–Sulfur Ligand Exchange Detected with Single-Molecule Fluorescence Microscopy. *Inorganic Chemistry* **2011**, 50, 9201-9203.
53. Zhang, Y.; Song, P.; Fu, Q.; Ruan, M.; Xu, W., Single-molecule chemical reaction reveals molecular reaction kinetics and dynamics. *Nat Commun* **2014**, 5.
54. Svoboda, K.; Mitra, P. P.; Block, S. M., FLUCTUATION ANALYSIS OF MOTOR PROTEIN MOVEMENT AND SINGLE ENZYME-KINETICS. *Proceedings of the National Academy of Sciences of the United States of America* **1994**, 91, 11782-11786.
55. Dawid, A.; Croquette, V.; Grigoriev, M.; Heslot, F., Single-molecule study of RuvAB-mediated Holliday-junction migration. *Proceedings of the National Academy of Sciences of the United States of America* **2004**, 101, 11611-11616.
56. Vilfan, I. D.; Lipfert, J.; Koster, D. A.; Lemay, S. G.; Dekker, N. H., *Magnetic Tweezers for Single-Molecule Experiments*. Springer: New York, 2009; p 371-395.
57. Howorka, S.; Movileanu, L.; Braha, O.; Bayley, H., Kinetics of duplex formation for individual DNA strands within a single protein nanopore. *Proceedings of the National Academy of Sciences of the United States of America* **2001**, 98, 12996-13001.
58. Strunz, T.; Oroszlan, K.; Schafer, R.; Guntherodt, H. J., Dynamic force spectroscopy of single DNA molecules. *Proceedings of the National Academy of Sciences of the United States of*

America **1999**, 96, 11277-11282.

59. Jana, N. R.; Gearheart, L.; Murphy, C. J., Wet Chemical Synthesis of High Aspect Ratio Cylindrical Gold Nanorods. *The Journal of Physical Chemistry B* **2001**, 105, 4065-4067.
60. Stöber, W.; Fink, A.; Bohn, E., Controlled growth of monodisperse silica spheres in the micron size range. *Journal of Colloid and Interface Science* **1968**, 26, 62-69.
61. Johnson, C. J.; Dujardin, E.; Davis, S. A.; Murphy, C. J.; Mann, S., Growth and form of gold nanorods prepared by seed-mediated, surfactant-directed synthesis. *Journal of Materials Chemistry* **2002**, 12, 1765-1770.
62. Gai, P. L.; Harmer, M. A., Surface Atomic Defect Structures and Growth of Gold Nanorods. *Nano Letters* **2002**, 2, 771-774.
63. Xu, W.; Kong, J. S.; Chen, P., Single-Molecule Kinetic Theory of Heterogeneous and Enzyme Catalysis. *The Journal of Physical Chemistry C* **2009**, 113, 2393-2404.
64. Cao, J.; Silbey, R. J., Generic Schemes for Single-Molecule Kinetics. 1: Self-Consistent Pathway Solutions for Renewal Processes. *The Journal of Physical Chemistry B* **2008**, 112, 12867-12880.
65. Zhuang, X.; Bartley, L. E.; Babcock, H. P.; Russell, R.; Ha, T.; Herschlag, D.; Chu, S., A Single-Molecule Study of RNA Catalysis and Folding. *Science* **2000**, 288, 2048-2051.
66. Diblock copolymer membranes investigated by single-particle tracking. *Physical Chemistry Chemical Physics* **2011**, 13, 2278.
67. Gopich, I. V.; Szabo, A., Theory of the statistics of kinetic transitions with application to single-molecule enzyme catalysis. *The Journal of Chemical Physics* **2006**, 124, -.
68. Satterfield, C. N., *Heterogeneous catalysis in practice*. McGraw-Hill: 1980.
69. Zhang, Z.; Berg, A.; Levanon, H.; Fessenden, R. W.; Meisel, D., On the Interactions of Free Radicals with Gold Nanoparticles. *Journal of the American Chemical Society* **2003**, 125, 7959-7963.
70. Zhang, Z.-F.; Cui, H.; Lai, C.-Z.; Liu, L.-J., Gold Nanoparticle-Catalyzed Luminol Chemiluminescence and Its Analytical Applications. *Analytical Chemistry* **2005**, 77, 3324-3329.
71. Corma, A.; Garcia, H., Supported gold nanoparticles as catalysts for organic reactions. *Chemical Society Reviews* **2008**, 37, 2096-2126.
72. Ionita, P.; Gilbert, B. C.; Chechik, V., Radical Mechanism of a Place-Exchange Reaction of Au Nanoparticles. *Angewandte Chemie* **2005**, 117, 3786-3788.
73. He, W.; Zhou, Y.-T.; Wamer, W. G.; Hu, X.; Wu, X.; Zheng, Z.; Boudreau, M. D.; Yin, J.-J., Intrinsic catalytic activity of Au nanoparticles with respect to hydrogen peroxide decomposition and superoxide scavenging. *Biomaterials* **2013**, 34, 765-773.
74. Suh, M.; Bagus, P. S.; Pak, S.; Rosynek, M. P.; Lunsford, J. H., Reactions of Hydroxyl

Radicals on Titania, Silica, Alumina, and Gold Surfaces. *The Journal of Physical Chemistry B* **2000**, 104, 2736-2742.

75. Baptista, L.; Clemente da Silva, E.; Arbilla, G., Oxidation mechanism of dimethyl sulfoxide (DMSO) by OH radical in liquid phase. *Physical Chemistry Chemical Physics* **2008**, 10, 6867-6879.

76. Rao, P. S.; Lubber Jr, J. M.; Milinowicz, J.; Lalezari, P.; Mueller, H. S., Specificity of oxygen radical scavengers and assessment of free radical scavenger efficiency using luminol enhanced chemiluminescence. *Biochemical and Biophysical Research Communications* **1988**, 150, 39-44.

77. Yamamoto, K.; Inoue, S.; Yamazaki, A.; Yoshinaga, T.; Kawanishi, S., Site-specific DNA damage induced by cobalt(II) ion and hydrogen peroxide: role of singlet oxygen. *Chemical Research in Toxicology* **1989**, 2, 234-239.

78. Gomes, A.; Fernandes, E.; Lima, J. L. F. C., Fluorescence probes used for detection of reactive oxygen species. *Journal of Biochemical and Biophysical Methods* **2005**, 65, 45-80.

79. Hanasaki, Y.; Ogawa, S.; Fukui, S., The correlation between active oxygens scavenging and antioxidative effects of flavonoids. *Free Radical Biology and Medicine* **1994**, 16, 845-850.

80. Tai, C.; Gu, X.; Zou, H.; Guo, Q., A new simple and sensitive fluorometric method for the determination of hydroxyl radical and its application. *Talanta* **2002**, 58, 661-667.

81. Gorris, H. H.; Walt, D. R., Mechanistic Aspects of Horseradish Peroxidase Elucidated through Single-Molecule Studies. *Journal of the American Chemical Society* **2009**, 131, 6277-6282.

82. Mishin, V.; Gray, J. P.; Heck, D. E.; Laskin, D. L.; Laskin, J. D., Application of the Amplex red/horseradish peroxidase assay to measure hydrogen peroxide generation by recombinant microsomal enzymes. *Free Radical Biology and Medicine* **2010**, 48, 1485-1491.

83. León, D.; Marín-García, P.; Sánchez-Nogueiro, J.; de la O, F. O.; García-Carmona, F.; Miras-Portugal, M. T., P2X agonist BzATP interferes with amplex-red-coupled fluorescence assays. *Analytical Biochemistry* **2007**, 367, 140-142.

2.6 Supporting Information

2.6.1 Au nanocatalysts preparation and characterization

2.6.1.1 Preparation of Au@mSiO₂ nanorods

Au@mSiO₂ nanorods were made by first synthesizing the Au nanorods via seeded growth (following Murphy *et al.*¹), then coating the nanorods with a silica shell, and then base etching the shell to make it mesoporous, as reported in detail by us previously.²

For the seeded growth to make Au nanorods, pseudospherical Au seeds were first prepared by adding 0.6 mL 0.1 M of ice cold NaBH₄ into 20 mL aqueous solution containing 2.5×10^{-4} M HAuCl₄ (Aldrich) and 2.5×10^{-4} M trisodium citrate (J. T. Baker). To grow the nanorods, 1 mL of the as-prepared seed solution was added into three identical growth solutions constituted by 2.5×10^{-4} M HAuCl₄, 0.1 M cetyltrimethylammonium (CTAB) (Aldrich), and 5.6×10^{-4} M ascorbic acid (EM Science) sequentially. The volumes of the growth solutions were 9, 18 and 180 mL, respectively, while the growth times were 15 s, 30 s, and overnight.

To grow the silica shell on the nanorods, a freshly prepared 150 μ L ethanol solution of 0.54 mM 3-mercaptopropyltrimethoxysilane (MPTMS) was added to 4 mL of the final Au nanorod solution with vigorous stirring. After 30 min, 150 μ L of 0.54% w/v aqueous Na₂SiO₃ solution was added and stirred for another 48 hours to form a thin layer of silica on Au nanorods. Further growth of the silica shell was done by adding 160 μ L, 10 v% tetraethyl orthosilicate (TEOS) (Aldrich) under stirring, following the procedure by Stöber *et al.*³ The silica-coated Au nanorods were then etched with NaOH in the presence of CTAB to make the shell mesoporous. 70 μ L 0.1 M NaOH and 140 μ L 0.1 M CTAB was added under stirring at room temperature for 15 min. The solution was then transferred to 363 K oil bath and left unstirred for 2 hours. After recovering the Au@mSiO₂ nanorods by centrifugation, they were first heated in air at 373 K for 2 hours, then

calcinated at 773 K for another 1 hour to remove the capping ligands and other organic components while the Au nanorod cores maintain their morphology as analyzed by TEM.²

2.6.1.2 Structural characterization of Au nanocatalysts

The Au nanocatalysts were structurally characterized by TEM. Figure S2.1A (same as Figure 2.1C in the main text) is the TEM of pseudospherical Au nanoparticles (Ted Pella JME1052). The averaged diameter is measured to be 5.3 ± 0.7 nm (Figure S2.1B). For the Au@mSiO₂ nanorods, the lengths of Au nanorod cores are poly-disperse, ranging from ~100 nm to 600-700 nm (Figure S2.1C, and Figure 2.1B in the main text), but their diameters are monodisperse, as we reported previously:² the averaged diameter of the Au core of samples used in this study is 21.4 ± 3.2 nm, with the mSiO₂ shell about 80 nm in thickness.² The Au@mSiO₂ sample usually is a mixture of nanorods, nanoparticles and nanoplates (Figure S2.1C), but the nanorods are easily identified in our single-molecule imaging measurements as well as in the parallel SEM images (e.g., Figure S2.2 below).⁴

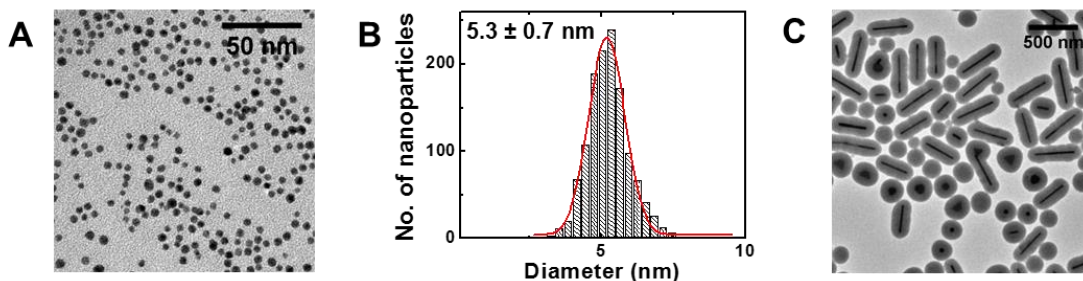


Figure S2.1 (A) TEM image of pseudospherical 5.3 nm Au nanoparticles. (B) Distribution of nanoparticle diameter from A. Red curve is a Gaussian fit. (C) TEM image of mSiO₂ coated Au nanorods coexisting with nanoplates and nanoparticles.

2.6.1.3 Determining the lengths of Au nanorod core from the SEM images of individual Au@mSiO₂ nanorods

The nanorod length used in the main text (Figure 2.5A-C and section 2.3.5) refers to the length of the Au nanorod core of a Au@mSiO₂ nanorod. It was determined from the SEM image (Figure S2.2) of the same sample after the single-molecule catalysis imaging measurements, from which the overall length (including the mSiO₂ shell) was directly determined. With the known mSiO₂ shell thickness (~80 nm) from TEM characterization, the length of the Au nanorod core was then deduced. The details about the combined TEM and SEM characterization of the Au@mSiO₂ nanorods were reported in our previous publication.²

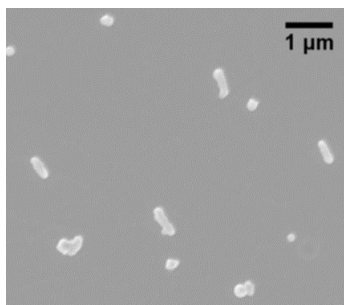


Figure S2.2 SEM image of Au@mSiO₂ nanorods after single-molecule catalysis imaging measurements. The individual nanorods are clearly identifiable.

2.6.2 Analysis procedures to extract the fluorescence intensity vs time trajectories during catalysis of single nanocatalysts

The 5.3 nm pseudospherical Au nanoparticles are invisible in fluorescence microscopy owing to their small size. Under catalysis, the detected emission signal comes entirely from the

laser-induced fluorescence of the catalytic reaction product resorufin. On the other hand, the Au nanorods within Au@mSiO₂ nanorods have intrinsic stable emission under laser excitation,^{2, 5-7} and the fluorescence of the reaction products during catalysis appears on top of a constant nanorod emission background. Therefore, two different analysis procedures were used to analyze the fluorescence movies to extract the fluorescence intensity versus time trajectories for individual 5.3 nm pseudospherical Au nanoparticle and Au@mSiO₂ nanorods, respectively. The analysis procedures are each described below.

2.6.2.1 Analysis procedures for 5.3 nm pseudospherical Au nanoparticles

A simple, low computational cost procedure was used here, as described previously.⁸⁻¹⁰ A home-written IDL program was used to extract fluorescence trajectories throughout the entire movie. Intensities of localized fluorescence spots were obtained by integrating the signal counts over a $\sim 7 \times 7$ pixel area (each pixel ~ 267 nm). Integration over different fluorescence spots were running parallel to each other, giving an output file containing all the fluorescence trajectories from the many individual nanoparticles in the movie. For each single trajectory, the microscopic reaction time τ was extracted as the time between a fluorescent burst and its subsequent one (reference Figures 2.2A and 2.3A in the main text).

2.6.2.2 Analysis procedures for Au@mSiO₂ nanorods

The analysis of the fluorescence signals from individual Au@mSiO₂ nanorods was described in detail in our previous publication.² Briefly, the fluorescence trajectory for each Au@mSiO₂ nanorod during catalysis was first obtained by integrating fluorescence counts within a $\sim 7 \times 7$ pixel area, which is sufficiently large to encompass the entire nanorod as well as the fluorescence signal of the catalytic product. A two-stage fluorescence intensity thresholding

procedure was used, as described in detail previously,² to select fluorescence signals from the catalytic products while suppressing nanorod emission contributions. The image frames corresponding to the selected fluorescence bursts were further analyzed. The intrinsic emission signal from the nanorod was first subtracted and the remaining fluorescence image (in a 13×13 pixel area) was fitted with a 2D Gaussian function (as an approximation to the fluorescence point spread function, PSF) on top of a sloping background. This fitting generates the center position (x_0 , y_0) of the fluorescent molecule, the errors/uncertainties (Er_x , Er_y) of the center position, and the widths (σ_x , σ_y) of the PSF. Based on the PSF fitting results, the fluorescence bursts selected from the prior intensity thresholding were further filtered by two criteria: (1) The errors of the center position in PSF fitting, Er_x , Er_y , should be less than 1000 nm; this removes the signals having poor signal-to-noise ratios. (The average Er_x and Er_y is about 10-20 nm.²) (2) σ_x and σ_y , the widths of the fitted PSF, should be $80 \text{ nm} < \sigma_{x \text{ or } y} < 1000 \text{ nm}$, as the rest are unreasonable for the fluorescence PSF of a single molecule. (The average σ_x and σ_y is about 180 nm.²) After these additional filtering, the final catalytic fluorescence events were registered, including the timing of each event and the location of each catalytic product molecule. The time separations, i.e., τ , between temporally neighboring events were determined.

2.6.2.3 Distribution of fluorescence burst on-time during catalysis by Au nanocatalysts

The duration (i.e., on-time) of each fluorescent bursts represents the waiting time for a product resorufin molecule to fully dissociate from the nanocatalyst. The average on-time for Au@mSiO₂ nanorods and 5.3 nm Au nanoparticles are around 100 ms and 50 ms, respectively (Figure S2.3A and B), which are much shorter than their respective average τ . In this study, on-time was not analyzed separately and was included in τ .

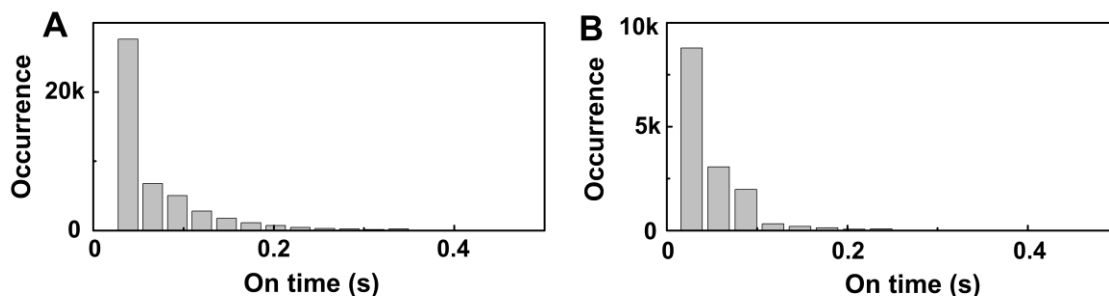


Figure S2.3 Distribution of fluorescence burst on-time from: (A) Compiled ~ninety Au@mSiO₂ nanorods at [AR] = 50 nM; (B) Compiled ~ninety 5.3 nm Au nanoparticles at [AR] = 1.2 μM. [H₂O₂] was kept at 60 mM for both (A) and (B).

2.6.3 The distributions of τ , once compiled from many nanocatalysts, lose the characteristic rise-followed-by-decay behavior from the kinetic intermediate

2.6.3.1 Distributions of τ compiled from many Au@mSiO₂ nanorods

Figure S2.4 shows the distributions of τ compiled from 90 Au@mSiO₂ nanorods at two different [AR]. Compared with the distribution of τ from a single Au@mSiO₂ nanorod (e.g., Figure 2.2B, C and D in the main text), the initial rise part of the τ distribution is indiscernible, and the distributions show apparent single-exponential decay behavior, which is most often seen in single-molecule kinetics. This indiscernibility results from the heterogeneity in catalytic kinetics among the nanorods, and it indicates that even with single-turnover resolution, single-particle level measurements are needed as well to unmask the kinetic intermediate.

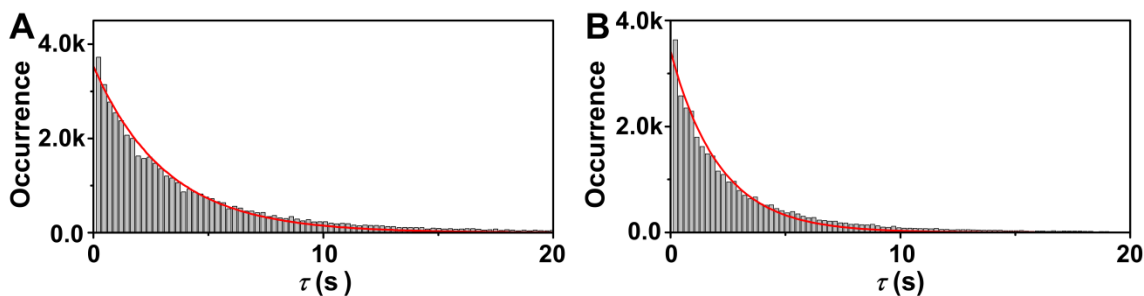


Figure S2.4 Distribution of τ compiled from 90 Au@mSiO₂ nanorods at [AR] = 50 nM (A) and [AR] = 100 nM (B). H₂O₂ concentration was kept at 60 mM. Solid red lines are fits with $y = A \cdot e^{-k\tau}$.

2.6.3.2 Distributions of τ compiled from many 5.3 nm Au nanoparticles

Figure S2.5 shows the distributions of τ compiled from two sets of 5.3 nm Au nanoparticles. Each set contains ~80 nanoparticles. Again the initial-rise-and-then-decay behavior observed from a single 5.3 nm Au nanoparticle (Figure 2.3B in the main text) cannot be clearly discerned in the compiled data. The distributions only contain the decay part, which can be well fitted with a single-exponential decay function.

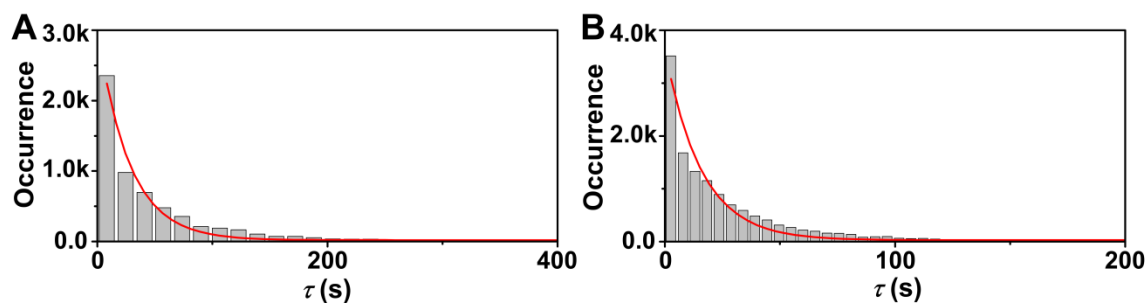
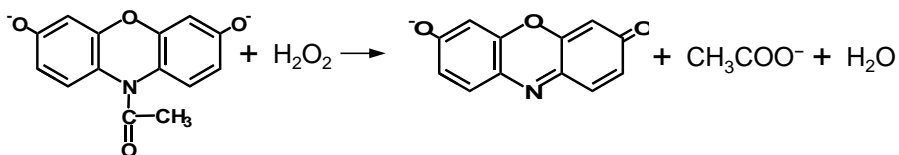


Figure S2.5 Distribution of τ compiled from ~eighty 5.3 nm Au nanoparticles at [AR] = 0.5 μ M (A) and [AR] = 1.2 μ M (B). H₂O₂ concentration was kept at 60 mM. Solid red lines are fits with $y = A \cdot e^{-k\tau}$.

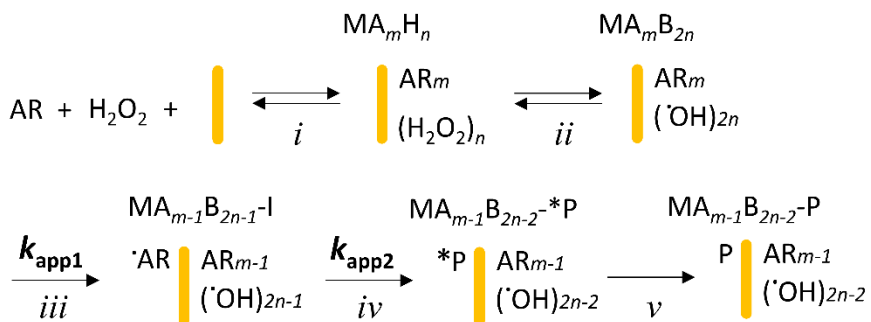
2.6.4 Kinetic mechanism and derivation of the probability density function $f(\tau)$ of the microscopic reaction time τ

Our previous study showed that amplex red oxidation by H_2O_2 generates the resorufin and acetate, in amplex-red: H_2O_2 :resorufin:acetate = 1:1:1:1 stoichiometry, which is described by the balanced chemical equation in Scheme S2.1.⁹ Overall, it involves a two-electron oxidation of amplex red.

Scheme S2.1 Balanced chemical equation of oxidative deacetylation of amplex red by H_2O_2 to generate resorufin, acetate, and water



Scheme S2.2 Possible mechanism of catalysis ^a



^a M: Au nanocatalyst; A: amplex red; H: H_2O_2 ; B: $\text{OH}\bullet$ radical; I: the intermediate $\text{AR}\bullet$;

P*: resorufin molecule in a *possibly* fluorescence-quenched state; P: fluorescent product

resorufin. MA_mB_{2n} represents a Au nanorod/nanoparticle having m adsorbed amplex red molecules and $2n$ $OH\bullet$.

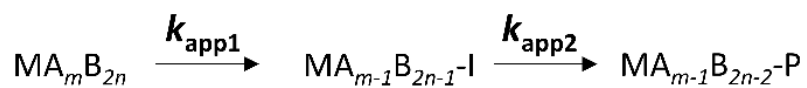
Scheme S2.2 presents a possible reaction sequence for surface-catalyzed oxidative deacetylation of amplex red to resorufin on Au nanocatalysts, which has 1:1 reaction stoichiometry between amplex red and H_2O_2 . The two reactants first adsorb reversibly to the Au surface (step *i*). The adsorbed H_2O_2 then undergoes a reversible homolytic O-O bond cleavage to generate surface-bound $OH\bullet$ radicals (step *ii*). The presence of $OH\bullet$ radicals in the reaction pathway is supported by our observation that the catalytic rate is strongly quenched by DMSO (Figure 2.4B in the main text), a known effective $OH\bullet$ quencher.¹¹⁻¹⁶ It is also known that Au surface can catalyze H_2O_2 decomposition to form $OH\bullet$ radicals,¹⁷⁻²³ and this reaction is likely reversible.²³ Then the reaction proceeds via a one-electron oxidation of AR by a surface bound $OH\bullet$ radical, generating a radical species $AR\bullet$ (step *iii*). A subsequent 2nd electron oxidation generates the product resorufin (step *iv*). The deacetylation could be accompanying the 1st or the 2nd oxidation step, or occur as a separate step that is not explicitly included here. Although our previous studies on small (≤ 15 nm in diameter) bare Au nanoparticles showed that we could directly detect the fluorescence of P on their surfaces, for the Au@mSiO₂ nanorods here, the generated P on the Au nanorod surface could potentially be fluorescently quenched (i.e., P*) due to the proximity to the Au surface, before desorbing from Au nanorod surface (step *v*) and getting temporarily trapped in the mSiO₂ shell of the Au@mSiO₂ nanorods. We will justify below that P*, the fluorescence-quenched species, either does not exist in the reaction pathway or at least does not exist in a kinetically relevant fashion (i.e., step *v* is very fast).

The distributions of the microscopic reaction time τ from our single-molecule catalysis measurements (Figures 2.2B-D and Figures 2.3B-C in the main text) have shown that the reaction kinetics contains two rate-determining steps straddling over one kinetic intermediate. In Scheme S2.2, step *i* can be assumed to follow a fast adsorption-desorption equilibrium, in which amplex red and H₂O₂ each follow a Langmuir adsorption behavior onto different types of surface sites, which would be consistent with the saturation kinetics observed with increasing reactant concentrations (Figure 2.2G, Figure 2.3F, Figure 2.4A and Equation (S2.16) later). The fluorescence-quenched P* species on the Au surface could not be the observed kinetic intermediate; otherwise, the desorption of P* to become P that is temporarily trapped in the mSiO₂ shell would be one of the rate-determining steps, but this step does not exist for the bare 5.3 nm Au nanoparticles for which the kinetic intermediate is still observed (Figure 2.3B-C in the main text). *Thus, step v in Scheme S2.2 is not a kinetically relevant step, and is not included in the mechanism in Scheme 2.1 in the main text.*

Therefore, the two rate-determining steps observed experimentally should come from the remaining three reaction steps in Scheme S2.2 (i.e., step *ii*, *iii*, and *iv*), involving two possible reaction intermediates, the one-electron-oxidized amplex radical AR• and the OH• radical. The involvement of the AR• radical in the oxidation of amplex red to form resorufin has been shown in the catalysis by the enzyme horseradish peroxidase.²⁴⁻²⁷ The involvement of OH• radical in the reaction is supported by our observation that DMSO can quench the reaction (Figure 2.4B in the main text). Below we will treat the two possibilities separately. And later we will present evidences that argue against OH• being the reaction kinetic intermediate observed in our single-molecule kinetics.

2.6.4.1 Mechanism 1: Surface-adsorbed AR• being the kinetic intermediate. Assuming the amplex red radical (AR•) being the observed reaction intermediate, steps *iii* and *iv* are then the two rate-determining steps, with all other steps being fast in Scheme S2.2. Consequently, the reaction mechanism reduces to the effective kinetic mechanism in Scheme S2.3 with only two kinetic steps:

Scheme S2.3 Reduced effective kinetic mechanism with AR• being the observed reaction intermediate



Here MA_mB_{2n} is a Au nanocatalyst (i.e., M) with surface adsorbed amplex red (i.e., A) and HO• radical (i.e., B) in rapid equilibrium with amplex red and H_2O_2 in solution. I stands for the amplex red radical AR•, P for the final product resorufin. m is the number of amplex red molecule adsorbed on the catalyst particle surface and $2n$ is the number of OH• radical adsorbed. k_{app1} and k_{app2} are the two corresponding apparent rate constants. The first step involves amplex red; its associated apparent rate constant k_{app1} is expected to be dependent on the concentration of amplex red on the catalyst surface and thus on its concentration in solution. The second step is expected to be independent of amplex red concentration. Our experimental results in Figure 2.2E-F and Figure 2.3D-E in the main text show that the amplex-red-concentration-independent step (which corresponds to k_{app2} here; see the derived Equation (S2.8) below) is one magnitude faster than the amplex-red-concentration-dependent step (which corresponds to k_{app1} here; see Equation (S2.7) below). Therefore, in Scheme S2.3, the formation of the intermediate I is slower, and it is followed

by a faster consumption step. Therefore, we assume no intermediate accumulation on catalytic surface.

The apparent rate constants k_{app1} and k_{app2} take the following forms:

$$k_{app1} = \gamma_1 m(2n) \quad (S2.1)$$

$$k_{app2} = \gamma_2(2n - 1)(1) \approx \gamma_2(2n) \quad (S2.2)$$

where γ_1 and γ_2 are rate constants.

Assuming noncompetitive adsorption between amplex red and $H_2O_2/HO\bullet$ on the nanoparticle surface (i.e., they adsorb onto different types of surface sites), Langmuir adsorption model gives:

$$m = n_A \theta_A \quad (S2.3)$$

$$2n = n_B \theta_B \quad (S2.4)$$

where n_A and n_B are the total number of adsorption sites for amplex red and $HO\bullet$ respectively; θ_A and θ_B are the respective fractions of surface sites occupied by amplex red and $OH\bullet$. For simple unimolecular Langmuir adsorption of amplex red, θ_A takes the form:²⁸

$$\theta_A = \frac{G_A[A]}{1+G_A[A]} \quad (S2.5)$$

where G_A is the adsorption equilibrium constant of amplex red and $[A]$ is the amplex red concentration in solution. On the other hand, $HO\bullet$ radical comes from the O-O bond cleavage of H_2O_2 upon adsorption, and each H_2O_2 molecules generates two $OH\bullet$; here θ_B takes the form:²⁸

$$\theta_B = \frac{G_B^{1/2}[H]^{1/2}}{1 + G_B^{1/2}[H]^{1/2}} \quad (S2.6)$$

In Equation (S2.6), G_B represents the equilibrium constant for H_2O_2 adsorbing to directly become two adsorbed $HO\bullet$ (i.e., steps *i* and *ii* in Scheme 2.2 collapse into one effective adsorption

equilibrium, with minimal H₂O₂ adsorbed as intact molecules on Au surfaces), and [H] is the H₂O₂ concentration in solution. Therefore,

$$k_{\text{app1}} = \gamma_1 n_A n_B \frac{G_A[A]}{1 + G_A[A]} \frac{G_B^{1/2}[H]^{1/2}}{1 + G_B^{1/2}[H]^{1/2}} \quad (\text{S2.7})$$

$$= \gamma_{\text{eff1}} \frac{G_A[A]}{1 + G_A[A]} \frac{G_B^{1/2}[H]^{1/2}}{1 + G_B^{1/2}[H]^{1/2}}$$

$$k_{\text{app2}} = \gamma_2 n_B \frac{G_B^{1/2}[H]^{1/2}}{1 + G_B^{1/2}[H]^{1/2}} = \gamma_{\text{eff2}} \frac{G_B^{1/2}[H]^{1/2}}{1 + G_B^{1/2}[H]^{1/2}} \quad (\text{S2.8})$$

where $\gamma_{\text{eff1}} = \gamma_1 n_A n_B$ and $\gamma_{\text{eff2}} = \gamma_2 n_B$. At saturating H₂O₂ concentrations, $\frac{G_B^{1/2}[H]^{1/2}}{1 + G_B^{1/2}[H]^{1/2}} \rightarrow 1$,

Equations (S2.7) and (S2.8) reduces to:

$$k_{\text{app1}} = \gamma_{\text{eff1}} \frac{G_A[A]}{1 + G_A[A]} \quad (\text{S2.9})$$

$$k_{\text{app2}} = \gamma_{\text{eff2}} \quad (\text{S2.10})$$

The single-molecule probabilistic rate equations for Scheme 2.3 are:

$$\frac{dP_{\text{MA}_m \text{B}_{2n}}}{dt} = -k_{\text{app1}} P_{\text{MA}_m \text{B}_{2n}} \quad (\text{S2.11})$$

$$\frac{dP_{\text{MA}_{m-1} \text{B}_{2n-1-I}}}{dt} = k_{\text{app1}} P_{\text{MA}_m \text{B}_{2n}} - k_{\text{app2}} P_{\text{MA}_{m-1} \text{B}_{2n-1-I}} \quad (\text{S2.12})$$

$$\frac{dP_{\text{MA}_{m-1} \text{B}_{2n-2-P}}}{dt} = k_{\text{app2}} P_{\text{MA}_{m-1} \text{B}_{2n-1-I}} \quad (\text{S2.13})$$

where P represents the probability of finding the nanoparticle at each state. The initial conditions are $P_{MA_mB_{2n}} = 1$, $P_{MA_{m-1}B_{2n-1-I}} = 0$, and $P_{MA_{m-1}B_{2n-2-P}} = 0$; and the boundary condition is $P_{MA_mB_{2n}} + P_{MA_{m-1}B_{2n-1-I}} + P_{MA_{m-1}B_{2n-2-P}} = 1$.

If $f(\tau)$ is the probability density function of the microscopic reaction time τ , $f(\tau)\Delta\tau$ is the probability of finding a particular τ . This probability is equal to the probability of switching from $P_{MA_{m-1}B_{2n-1-I}}$ to $P_{MA_{m-1}B_{2n-2-P}}$ between $t = \tau$ and $t = \tau + \Delta\tau$, which is $\Delta P_{MA_{m-1}B_{2n-2-P}}$. Thus the probability density function $f(\tau)$ equals to $\frac{d}{dt}P_{MA_{m-1}B_{2n-2-P}}|_{t=\tau}$. Solve equations (S2.11)-(S2.13) for $P_{MA_{m-1}B_{2n-2-P}}$, we have:

$$f(\tau) = \frac{k_{app1}k_{app2}}{k_{app2} - k_{app1}}(e^{-k_{app1}\tau} - e^{-k_{app2}\tau}) \quad (S2.14)$$

Note that Equation (S2.14) has the same form as the empirical equation $y = A \cdot (e^{-k_1\tau} - e^{-k_2\tau})$ (Equation (2.1) in the main text) used in fitting Figure 2.2B-D and Figure 2.3B-C in the main text. Therefore, k_{app1} and k_{app2} correspond to k_1 and k_2 for this mechanism.

Replacing k_{app1} and k_{app2} using equations (S2.7)-(S2.8):

$$f(\tau) = \frac{\gamma_{eff1}G_A[A]}{\gamma_{eff2} + (\gamma_{eff2} - \gamma_{eff1})G_A[A]} \cdot \frac{\gamma_{eff2}G_B^{1/2}[H]^{1/2}}{1 + G_B^{1/2}[H]^{1/2}} \cdot \left\{ \exp\left(-\gamma_{eff1} \frac{G_A[A]}{1 + G_A[A]} \frac{G_B^{1/2}[H]^{1/2}}{1 + G_B^{1/2}[H]^{1/2}} \tau\right) - \exp\left(-\gamma_{eff2} \frac{G_B^{1/2}[H]^{1/2}}{1 + G_B^{1/2}[H]^{1/2}} \tau\right) \right\} \quad (S2.15)$$

Then $\langle \tau \rangle^{-1}$, the time-averaged product formation rate, which is the equivalent to the rate of turnovers, for a single catalyst particle is:

$$\langle \tau \rangle^{-1} = 1 / \int_0^{\infty} \tau f(\tau) d\tau = \frac{\gamma_{\text{eff1}} G_A[A]}{\gamma_{\text{eff2}} + (\gamma_{\text{eff1}} + \gamma_{\text{eff2}}) G_A[A]} \cdot \frac{\gamma_{\text{eff2}} G_B^{1/2} [H]^{1/2}}{1 + G_B^{1/2} [H]^{1/2}} \quad (\text{S2.16})$$

When the H_2O_2 concentration is saturating (i.e., $[H] \rightarrow \infty$), which is our experimental condition for Figures 2.2 and 2.3 in the main text, $\frac{G_B^{1/2} [H]^{1/2}}{1 + G_B^{1/2} [H]^{1/2}} \rightarrow 1$. Equations (S2.15) simplifies to:

$$f(\tau) = \frac{\gamma_{\text{eff1}} G_A[A]}{1 + (1 - \frac{\gamma_{\text{eff1}}}{\gamma_{\text{eff2}}}) G_A[A]} \cdot \left\{ \exp\left(-\gamma_{\text{eff1}} \frac{G_A[A]}{1 + G_A[A]} \tau\right) - \exp(-\gamma_{\text{eff2}} \tau) \right\} \quad (\text{S2.17})$$

$f(\tau)$ is now a bi-exponential function, with one exponent dependent on $[A]$ (i.e., the amplex red concentration) and the other one independent of $[A]$, as we observed experimentally (Figure 2.2E-F and Figure 2.3D-E in the main text).

For $\langle \tau \rangle^{-1}$, at $[H] \rightarrow \infty$, it becomes

$$\langle \tau \rangle^{-1} = \frac{\gamma_{\text{eff1}} G_A[A]}{1 + (1 + \frac{\gamma_{\text{eff1}}}{\gamma_{\text{eff2}}}) G_A[A]} \xrightarrow{\gamma_{\text{eff2}} \gg \gamma_{\text{eff1}}} \frac{\gamma_{\text{eff1}} G_A[A]}{1 + G_A[A]} \quad (\text{S2.18})$$

$\langle \tau \rangle^{-1}$ represents simple saturation kinetics, and it equals $\gamma_{\text{eff1}} / (1 + \gamma_{\text{eff1}} / \gamma_{\text{eff2}})$ when $[A] \rightarrow \infty$. And when $[A] \rightarrow \infty$ and $\gamma_{\text{eff2}} \gg \gamma_{\text{eff1}}$, $\langle \tau \rangle^{-1} = \gamma_{\text{eff1}}$.

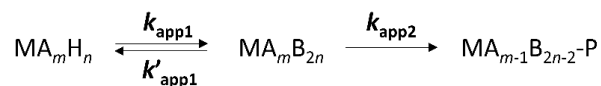
When $[H] \rightarrow \infty$ and $[A] \rightarrow \infty$, $\frac{G_A[A]}{1 + G_A[A]} \rightarrow 1$ and $\frac{G_B^{1/2} [H]^{1/2}}{1 + G_B^{1/2} [H]^{1/2}} \rightarrow 1$. We have then:

$$f(\tau) = \frac{\gamma_{\text{eff1}} \gamma_{\text{eff2}}}{\gamma_{\text{eff2}} - \gamma_{\text{eff1}}} \cdot \{ \exp(-\gamma_{\text{eff1}} \tau) - \exp(-\gamma_{\text{eff2}} \tau) \} \quad (\text{S2.19})$$

$$\langle \tau \rangle^{-1} = \frac{\gamma_{\text{eff1}}\gamma_{\text{eff2}}}{\gamma_{\text{eff2}} + \gamma_{\text{eff1}}} \xrightarrow{\gamma_{\text{eff2}} \gg \gamma_{\text{eff1}}} \gamma_{\text{eff1}} \quad (\text{S2.20})$$

2.6.4.2 Mechanism 2: Surface-adsorbed OH• being the kinetic intermediate. In the last section, we presented the mechanism assuming the amplex red radical being the observed reaction intermediate. Here we present the alternative mechanism assuming OH• radical being the observed reaction intermediate. Then, in Scheme S2.2, the two rate-determining steps would be steps *ii* and *iii*, i.e., the O-O bond cleavage of H₂O₂ to form two OH• radicals that would be independent of amplex red, and the first 1-electron oxidation of amplex red by OH• that would be dependent on the amplex red concentration on the catalyst surface, before eventually generating the product resorufin. Consequently, the kinetic scheme simplifies to having only two kinetic steps (Scheme S2.4), where MA_mH_n is a Au nanocatalyst (i.e., M) with surface adsorbed amplex red (i.e., A) and H₂O₂ (i.e., H) in rapid equilibrium with amplex red and H₂O₂ in solution.

Scheme S2.4 Reduced kinetic mechanism with OH• being the observed reaction intermediate



In this mechanism, as the O-O bond cleavage is assumed to be one of the rate-determining steps (i.e., relatively slow), only part of the adsorbed H₂O₂ (i.e., H) will convert into OH• radical (i.e., B). In another word, the adsorption sites for H₂O₂ will now either be occupied by H₂O₂, or OH•, or be vacant. The formation of OH• would require a surface adsorbed H₂O₂ and a nearby vacant site. Therefore, the apparent rate constant k_{app1} would take the following form:²⁸

$$k_{app1} = \gamma_1 \cdot n_H \theta_H \cdot n_H (1 - \theta_H - \theta_B) \quad (S2.21)$$

Here n_H is the total number of adsorption sites for H_2O_2 and $OH\bullet$; θ_H and θ_B are the fractions of sites occupied by H_2O_2 and $OH\bullet$ radical respectively, and γ_1 is a rate constant.

The apparent rate constants k'_{app1} , and k_{app2} take the following forms:

$$k'_{app1} = \gamma' (n_H \theta_B)^2 \quad (S2.22)$$

$$k_{app2} = \gamma_2 n_H \theta_B n_A \theta_A \quad (S2.23)$$

Here γ' and γ_2 are two rate constants. n_A and θ_A are the number of adsorption sites for amplex red and their fractional occupation, as defined previously, and $\theta_A = \frac{G_A[A]}{1+G_A[A]}$ as in Equation (S2.5). Note for k_{app2} , we assume this rate-determining step is first order to the surface concentration of the $OH\bullet$ radical because the overall 2-electron oxidation of amplex red likely goes through two sequential 1-electron processes with the 1st one being the rate-determining as described in Scheme S2.2 and Mechanism 1 earlier.

Applying steady-state approximation for the surface concentration of the intermediate $OH\bullet$, $[OH\bullet]_s$, we have:

$$\frac{d[OH\bullet]_s}{dt} = 2\gamma_1 n_H^2 \theta_H (1 - \theta_H - \theta_B) - \gamma' (n_H \theta_B)^2 - \gamma_2 n_H \theta_B n_A \theta_A = 0 \quad (S2.24)$$

As H_2O_2 is assumed to be in rapid adsorption/desorption equilibrium between in solution and on the catalyst surface, we have

$$k_{ads}[H]n_H(1 - \theta_H - \theta_B) = k_{des}n_H\theta_H \quad (S2.25)$$

Here k_{ads} and k_{des} are the adsorption and desorption rate constants for H_2O_2 , respectively, and $[H]$ is the concentration of H_2O_2 in solution. Combine (S2.24) and (S2.25), and let $G_H = k_{ads}/k_{des}$, we have:

$$\gamma' n_H^2 \theta_B^2 + \gamma_2 n_A n_H \theta_A \theta_B = 2\gamma_1 n_H^2 \frac{G_H[H]}{(1 + G_H[H])^2} (1 - \theta_B)^2 \quad (\text{S2.26})$$

Let $a = 2\gamma_1 n_H^2 \frac{G_H[H]}{(1 + G_H[H])^2}$, $b = \gamma' n_H^2$, and $c = \gamma_2 n_A n_H \theta_A = \gamma_2 n_A n_H \frac{G_A[A]}{1 + G_A[A]}$, Equation (S2.26)

becomes:

$$(a - b)\theta_B^2 - (2a + c)\theta_B + a = 0 \quad (\text{S2.27})$$

Considering θ_B represents the fraction of active sites covered by OH• radical, then $0 < \theta_B < 1$.

Solving Equation (S2.27) gives:

$$\theta_B = \frac{2a + c - \sqrt{4ac + 4ab + c^2}}{2a - 2b} \quad (\text{S2.28})$$

Substitute into Equation (S2.25), we have:

$$\theta_H = \frac{G_H[H]}{1 + G_H[H]} \cdot \frac{2b + c - \sqrt{4ac + 4ab + c^2}}{2b - 2a} \quad (\text{S2.29})$$

Therefore, for k_{app1} , k'_{app1} , and k_{app2} in Scheme S2.4, they are:

$$k_{\text{app1}} = \frac{a(2b + c - \sqrt{4ac + 4ab + c^2})^2}{8(a - b)^2} \quad (\text{S2.30})$$

$$k'_{\text{app1}} = \frac{b(2a + c - \sqrt{4ac + 4ab + c^2})^2}{4(a - b)^2} \quad (\text{S2.31})$$

$$k_{\text{app2}} = \frac{c(2a + c - \sqrt{4ac + 4ab + c^2})}{2a - 2b} \quad (\text{S2.32})$$

The probability density function $f(\tau)$ for the microscopic reaction time τ corresponding to Scheme S2.4 has been derived in our previous publication²⁹ and earlier by others as well.³⁰⁻³²

$$f(\tau) = \frac{k_{\text{app1}}k_{\text{app2}}}{2\alpha} [e^{(\beta+\alpha)\tau} - e^{(\beta-\alpha)\tau}] \quad (\text{S2.33})$$

where $\alpha = \sqrt{\frac{1}{4}(k_{\text{app1}} + k'_{\text{app1}} + k_{\text{app2}})^2 - k_{\text{app1}}k_{\text{app2}}}$ and $\beta = -(k_{\text{app1}} + k'_{\text{app1}} + k_{\text{app2}})/2$.

$f(\tau)$ here is again a bi-exponential function, and the two exponents are $\beta+\alpha$ and $\beta-\alpha$. If mechanism 2 is the correct mechanism for interpreting our data, $\beta+\alpha$ and $\beta-\alpha$ would correspond to k_1 and k_2 in Equation (2.1) in the main text that was used to empirically fit Figure 2.2B-D and Figure 2.3B-C in the main text, respectively.

Based on the expression of $f(\tau)$ in Equation (S2.33), this alternative mechanism of assuming OH• being the observed reaction intermediate is disfavored for two reasons. First, since $c = \gamma_2 n_A n_H \frac{G_A[A]}{1+G_A[A]}$, k_{app1} , k'_{app1} and k_{app2} are all dependent on the amplex red concentration in solution. These dependences stem from the dependence of the three apparent rate constants on θ_B (Equation (S2.30)-(S2.32)), the site occupation fraction of OH• radical; and this θ_B is in turn dependent on the amplex red concentration [A] (Equation (S2.28)), as the surface adsorbed amplex red reacts with surface OH• to eventually generate the product resorufin. Therefore, the two exponents, $\beta+\alpha$ and $\beta-\alpha$, of $f(\tau)$ are both dependent on the amplex red concentration in solution. This prediction is in conflict with our experimental observation, because the faster-decay exponent in the distribution of τ is independent of amplex red concentration (Figure 2.2F and 2.3E in the main text).

Second, in this alternative mechanism, the O-O bond cleavage of H₂O₂ to generate OH• on Au surface is assumed to be slow enough to be rate-determining. However, previous work by Lunsford *et al.*²³ has shown that the H₂O₂ to hydroxyl radical conversion is fast on Au surfaces. They measured the rate of H₂O₂ decomposition on Au, in which the hydroxyl radical formation was part

of the decomposition pathways. The overall rate was measured to be $0.1 \mu\text{mol cm}^{-2} \text{s}^{-1}$. This rate would correspond to $\sim 10^7$ molecules per nanorod per second for Au@mSiO₂ catalyzed reaction (assuming on average a diameter of 21 nm and a length of 350 nm for the nanorod core) or 10^5 molecules per particle per second for the pseudospherical 5.3 nm Au particle. These predicted rates would be orders of magnitude faster than the highest reaction rates ($\sim 2 \text{s}^{-1} \text{particle}^{-1}$ for Au@mSiO₂ nanorods and $\sim 0.04 \text{s}^{-1} \text{particle}^{-1}$ for 5.3 nm Au nanoparticles, Figure 2.2G and 2.3F in the main text) observed experimentally. Based on these two reasons, this alternative mechanism assuming surface-adsorbed OH• being the observed reaction intermediate is disfavored.

2.6.5. References

1. Jana, N. R.; Gearheart, L.; Murphy, C. J., Wet Chemical Synthesis of High Aspect Ratio Cylindrical Gold Nanorods. *The Journal of Physical Chemistry B* **2001**, 105, 4065-4067.
2. Zhou, X.; Andoy, N. M.; Liu, G.; Choudhary, E.; Han, K.-S.; Shen, H.; Chen, P., Quantitative super-resolution imaging uncovers reactivity patterns on single nanocatalysts. *Nat Nano* **2012**, 7, 237-241.
3. Stöber, W.; Fink, A.; Bohn, E., Controlled growth of monodisperse silica spheres in the micron size range. *Journal of Colloid and Interface Science* **1968**, 26, 62-69.
4. Zhou, X.; Choudhary, E.; Andoy, N. M.; Zou, N.; Chen, P., Scalable Parallel Screening of Catalyst Activity at the Single-Particle Level and Subdiffraction Resolution. *ACS Catalysis* **2013**, 3, 1448-1453.
5. Eustis, S.; El-Sayed, M., Aspect Ratio Dependence of the Enhanced Fluorescence Intensity of Gold Nanorods: Experimental and Simulation Study. *The Journal of Physical Chemistry B* **2005**, 109, 16350-16356.
6. Geddes, C. D.; Parfenov, A.; Gryczynski, I.; Lakowicz, J. R., Luminescent blinking of gold nanoparticles. *Chemical Physics Letters* **2003**, 380, 269-272.
7. Tcherniak, A.; Dominguez-Medina, S.; Chang, W.-S.; Swanglap, P.; Slaughter, L. S.; Landes, C. F.; Link, S., One-Photon Plasmon Luminescence and Its Application to Correlation Spectroscopy as a Probe for Rotational and Translational Dynamics of Gold Nanorods. *The Journal of Physical Chemistry C* **2011**, 115, 15938-15949.
8. Xu, W.; Kong, J. S.; Yeh, Y.-T. E.; Chen, P., Single-molecule nanocatalysis reveals heterogeneous reaction pathways and catalytic dynamics. *Nat Mater* **2008**, 7, 992-996.
9. Han, K. S.; Liu, G.; Zhou, X.; Medina, R. E.; Chen, P., How Does a Single Pt Nanocatalyst Behave in Two Different Reactions? A Single-Molecule Study. *Nano Letters* **2012**, 12, 1253-1259.
10. Xiaochun Zhou, W. X., Guokun Liu, Debashis Panda, and Peng Chen, Size-Dependent Catalytic Activity and Dynamics of Gold Nanoparticles at the Single-Molecule Level. *J. AM. CHEM. SOC.* **2010**, 132, 138-146.
11. Rao, P. S.; Lubner Jr, J. M.; Milinowicz, J.; Lalezari, P.; Mueller, H. S., Specificity of oxygen radical scavengers and assessment of free radical scavenger efficiency using luminol enhanced chemiluminescence. *Biochemical and Biophysical Research Communications* **1988**, 150, 39-44.
12. Yamamoto, K.; Inoue, S.; Yamazaki, A.; Yoshinaga, T.; Kawanishi, S., Site-specific DNA damage induced by cobalt(II) ion and hydrogen peroxide: role of singlet oxygen. *Chemical Research in Toxicology* **1989**, 2, 234-239.
13. Gomes, A.; Fernandes, E.; Lima, J. L. F. C., Fluorescence probes used for detection of reactive oxygen species. *Journal of Biochemical and Biophysical Methods* **2005**, 65, 45-80.
14. Hanasaki, Y.; Ogawa, S.; Fukui, S., The correlation between active oxygens scavenging and antioxidative effects of flavonoids. *Free Radical Biology and Medicine* **1994**, 16, 845-850.

15. Tai, C.; Gu, X.; Zou, H.; Guo, Q., A new simple and sensitive fluorometric method for the determination of hydroxyl radical and its application. *Talanta* **2002**, 58, 661-667.
16. Baptista, L.; Clemente da Silva, E.; Arbilla, G., Oxidation mechanism of dimethyl sulfoxide (DMSO) by OH radical in liquid phase. *Physical Chemistry Chemical Physics* **2008**, 10, 6867-6879.
17. Zhang, Z.-F.; Cui, H.; Lai, C.-Z.; Liu, L.-J., Gold Nanoparticle-Catalyzed Luminol Chemiluminescence and Its Analytical Applications. *Analytical Chemistry* **2005**, 77, 3324-3329.
18. Zhang, Z.; Berg, A.; Levanon, H.; Fessenden, R. W.; Meisel, D., On the Interactions of Free Radicals with Gold Nanoparticles. *Journal of the American Chemical Society* **2003**, 125, 7959-7963.
19. Corma, A.; Garcia, H., Supported gold nanoparticles as catalysts for organic reactions. *Chemical Society Reviews* **2008**, 37, 2096-2126.
20. Ionita, P.; Gilbert, B. C.; Chechik, V., Radical Mechanism of a Place-Exchange Reaction of Au Nanoparticles. *Angewandte Chemie* **2005**, 117, 3786-3788.
21. He, W.; Zhou, Y.-T.; Wamer, W. G.; Hu, X.; Wu, X.; Zheng, Z.; Boudreau, M. D.; Yin, J.-J., Intrinsic catalytic activity of Au nanoparticles with respect to hydrogen peroxide decomposition and superoxide scavenging. *Biomaterials* **2013**, 34, 765-773.
22. Yadav, D.; Pospíšil, P., Role of chloride ion in hydroxyl radical production in photosystem II under heat stress: Electron paramagnetic resonance spin-trapping study. *J Bioenerg Biomembr* **2012**, 44, 365-372.
23. Suh, M.; Bagus, P. S.; Pak, S.; Rosynek, M. P.; Lunsford, J. H., Reactions of Hydroxyl Radicals on Titania, Silica, Alumina, and Gold Surfaces. *The Journal of Physical Chemistry B* **2000**, 104, 2736-2742.
24. Zhao, B.; Summers, F. A.; Mason, R. P., Photooxidation of Amplex red to resorufin: Implications of exposing the Amplex red assay to light. *Free Radical Biology and Medicine* **2012**, 53, 1080-1087.
25. Gorris, H. H.; Walt, D. R., Mechanistic Aspects of Horseradish Peroxidase Elucidated through Single-Molecule Studies. *Journal of the American Chemical Society* **2009**, 131, 6277-6282.
26. León, D.; Marín-García, P.; Sánchez-Nogueiro, J.; de la O, F. O.; García-Carmona, F.; Miras-Portugal, M. T., P2X agonist BzATP interferes with amplex-red-coupled fluorescence assays. *Analytical Biochemistry* **2007**, 367, 140-142.
27. Mishin, V.; Gray, J. P.; Heck, D. E.; Laskin, D. L.; Laskin, J. D., Application of the Amplex red/horseradish peroxidase assay to measure hydrogen peroxide generation by recombinant microsomal enzymes. *Free Radical Biology and Medicine* **2010**, 48, 1485-1491.
28. Satterfield, C. N., *Heterogeneous catalysis in practice*. McGraw-Hill: 1980.
29. Xu, W.; Kong, J. S.; Chen, P., Single-Molecule Kinetic Theory of Heterogeneous and

Enzyme Catalysis. *The Journal of Physical Chemistry C* **2009**, 113, 2393-2404.

30. Kou, S. C.; Cherayil, B. J.; Min, W.; English, B. P.; Xie, X. S., Single-Molecule Michaelis–Menten Equations. *The Journal of Physical Chemistry B* **2005**, 109, 19068-19081.

31. Xie, S., Single-Molecule Approach to Enzymology. *Single Molecules* **2001**, 2, 229-236.

32. Bent, B. E., Mimicking Aspects of Heterogeneous Catalysis: Generating, Isolating, and Reacting Proposed Surface Intermediates on Single Crystals in Vacuum. *Chemical Reviews* **1996**, 96, 1361-1390.

CHAPTER THREE

VISUALIZING GRAPHENE OXIDE SHEETS AND STUDYING THEIR ELECTROCHEMISTRY BY FLUORESCENCE MICROSCOPY

3.1 Introduction

Graphene, a single layer of sp^2 hybridized carbon atoms in a honeycomb lattice, features extraordinary thermal, chemical, mechanical and electrical properties.¹⁻⁶ Since the exfoliation of graphite into graphene sheets using the scotch tape method in 2004, much attention has been attracted onto this novel material.⁷⁻¹⁰ Researchers are actively improving the method of its synthesis, studying its properties and exploring its applications. Among these efforts, one branch of graphene research focuses on the chemical derivatives of graphene, which differ in properties from the pristine graphene sheet due to the existence of chemical moieties. Graphene oxide (i.e., GO), being one of the most well-known graphene derivatives, has many advantages.¹¹⁻¹⁸ The precursor for GO is graphite, which is ubiquitous and inexpensive; the exfoliation of graphite oxide is efficient with high yield, leading to simple and scalable production. With its oxygen functionalities, GO is hydrophilic, which facilitates its dispersion in various solvents. For making electronic devices, the van der Waal force between GO and the substrate is strong, which facilitates the integration of GO into electronic devices. Although properties of pristine graphene such as high carrier mobility and linear energy dispersion are absent in GO, its abundant oxygen containing functionalities enable subsequent functionalization. As a result, GO has versatility in electrochemical, optoelectronic and mechanical related applications.

Although being a promising material, there are still many major challenges in order to better utilize GO. Efforts have been made in studying the electrochemistry of GO.^{11-12, 18} However,

the inherent structure diversity among GOs requires study at the single sheet level, because each individual GO differs in size, shape, number of layers, and density of defect sites. In addition, the electrochemical process could take place at the basal plane, edges of the sheets, or the internal defect sites. For instance, Kern et al. reported the electronic transport properties of individual GO, and they found that the second layer in a bilayer GO is more conducting.¹⁴ Strano et al. discovered that the edges of single-layer graphene are more reactive in electron-transfer chemistry than the basal plane.¹⁹ These past researches all emphasize the importance of studying the graphene related materials in a spatially resolved fashion. Stemming from the few-layer nature, one of the common challenges for graphene and its related derivatives is to visualize the morphologies, for which scanning probe microscopies are usually employed, yet they all have certain limitations. For example, atomic force microscopy (AFM) requires a smooth substrate, such as freshly cut mica or silicon wafer, in order to obtain accurate thickness values on the nanometer scale.¹⁵ As a consequence, it is not suitable for large area, quick examinations. Scanning electron microscopy (SEM), although much faster, needs operation under vacuum and the exposed region is usually contaminated or partially destroyed because of the high-energy electron beam.²⁰⁻²¹ Raman spectroscopy²²⁻²³ and scanning electrochemical microscopy (SECM)²⁴⁻²⁵ contain rich chemical information, yet suffer from relatively low throughput and lower spatial resolution. On the other hand, optical microscopy with the advantages of being rapid and non-destructive, becomes an easy access to visualize graphene based materials. For example, Jung and coworkers used high-contrast optical imaging to characterize the graphene-based sheets, while Kim et al. developed the fluorescence quenching microscopy (FQM).²⁶⁻²⁷

GO is electrically insulating due to the abundant oxygen containing functionalities. To apply it in electronic or optoelectronic related areas, it must be reduced to become conductive. Various reduction methods have been reported in previous work, including exposing GO to reductive chemicals, such as hydrazine,^{14-15, 28} sodium borohydride,²⁹⁻³⁰ and hydroquinone,³⁰⁻³¹

thermally reducing GO in inert atmosphere;³²⁻³⁵ and electrochemical reduction.³⁶⁻³⁹ The electrochemical reduction involves no hazardous chemicals and eliminates the generation of byproducts.³⁵ Since it is a promising method in generating reduced graphene oxide (rGO), understanding the electrochemical reduction dynamics of GO is thus critical to optimizing the final performances in electrochemical applications.

This chapter focuses on the electrochemical catalysis of GO at the single sheet level. By using fluorescence microscopy and designing an electrochemical reaction, multiple GOs were studied simultaneously. The in-situ generated fluorescent molecules mapped out the activity distribution of each individual sheet, which helps to assign the boundaries, folded regions and wrinkles. Therefore, we propose this approach *might* also have potential applications in visualizing the morphology of graphene based materials. By sequentially applying reduction potential on a piece of GO and monitoring the activity changes, the reduction dynamics was studied.

3.2 Materials and Methods

3.2.1 Synthesis of Graphene Oxide (GO)

The GO used in our study was provided by Jaemyung Kim in Huang lab in Material Science and Engineering Department, Northwestern University. It was prepared using a modified Hummers and Offeman's methods by oxidizing the graphite powder (Bay carbon, SP-1).⁴⁰⁻⁴² 0.5 g graphite powder, 0.5 g NaNO₃, and 23 mL of concentrated H₂SO₄ were mixed and stirred in ice bath, while a total of 3 g of solid KMnO₄ was slowly added. Once completely mixed, the reaction solution is quickly transferred to 35 °C water bath and kept stirring for 1 h, resulting a thick paste. 40 mL of warm water was then added, and the solution was stirred for another 30 min. After that, another 100 mL of warm water was added, followed by slow addition of 3 mL of 30% H₂O₂. Upon adding

H₂O₂, the color of solution turned from dark brown to yellow. The warm solution was then filtered and rinsed with distilled water. The filter cake was re-dispersed in water by mechanical agitation. Centrifugation was carried out at low speed (1000 rpm) first and repeated 2 to 3 times to remove the visible particles. Followed that was high speed centrifugation at 8000 rpm for 15 min to remove the small GO piece and other byproducts. The final sediment was re-dispersed in water by mild sonication, resulting in a solution with exfoliated GO.

3.2.2 Modified Fluorescence Quenching Microscopy (FQM)

A modified fluorescence quenching microscopy method was used to characterize the as-received GO. It was performed on an Olympus IX71 inverted microscope with 532 nm LED illumination (Thorlabs, M530L2). An air 10X objective was used (Olympus UPlanFLN 10x/0.30 NA) with two filters in the detection path (HQ550LP, HQ580m60). GO solution was first diluted by 10X in 5:1 methanol/water solution (v/v), and drop casted on a piece of 1 x 3 inch glass microscope slide. Once completely dried under room temperature, 2 mL 4.5 mM rhodamine B (Sigma Aldrich, R6626) aqueous solution was spin coated onto the slide at 10,000 rpm. To image the GOs, a piece of blank slide was place under microscope first as the blank sample. 500 frames were captured with 1 s exposure time for each frame, and later averaged into one as the background image. Another 500 frames were captured for the GOs slide, which was later averaged into one and subtracted by the background image.

3.2.3 Ensemble Electrochemical Catalysis

Ensemble electrochemistry was performed using an electrochemical analyzer (CHI1200A, CH Instruments, Inc.) with a three-electrode configuration. A Ag/AgCl electrode was used as the reference electrode and a Pt foil was used as the counter electrode. The working electrode was a 2

mm diameter gold working electrode (CHI101). 10 μL of as-received GO solution was drop-casted on the gold electrode and dried at room temperature. The drop casting was repeated 1 to 2 times to have sufficient GO on the electrode. The supporting electrolyte used was 50 mM phosphate buffer at pH 7.3.

3.2.4 Fluorescence Enabled Electrochemical Microscopy

Fluorescence measurements were performed on a homebuilt prism-type total internal reflection (TIR) fluorescence microscope based on an Olympus IX71 inverted microscope. A continuous wave circularly polarized 532 nm laser beam (CrystaLaser, GCL-025-L-0.5%) of 3-6 mW was focused onto an area of $\sim 90 \times 45 \mu\text{m}^2$ on the sample to directly excite the fluorescence of product molecule resorufin. The fluorescence of resorufin was collected by a 60X NA 1.2 water-immersion objective (Olympus UPLSAPO60XW), optically filtered (HQ550LP) to reject laser scattering, and projected onto a camera (Andor iXon EMCCD), which is controlled by an Andor IQ software and operated at 50 ms frame rate. Sometimes an additional filter (HQ580m60) was also used in the detection path. All optical filters are from Chroma Technology Corp. All experiments were done at room temperature.

A flow cell (height \times length \times width = 100 $\mu\text{m} \times 2 \text{ cm} \times 5 \text{ mm}$), formed by double-sided tapes sandwiched between a glass slide and a borosilicate coverslip (Gold Seal[®]), was used to hold aqueous sample solutions for electrochemical fluorescence measurements. Part of the glass slide was cut to inset an ITO-coated quartz slide, which was used as the working electrode. Before assembled into a flow cell, as-received GO solution was diluted by 10X in 5:1 methanol/water (v/v) solution, and 10 μL of the final solution was drop casted on ITO-coated quartz slide. On the quartz slide, three holes were drilled. Two of them were used to connect to polyethylene tubing and a syringe pump for continuous solution flow to supply the reactants. The third one was used to place

the Ag/AgCl reference electrode. A Pt foil was sandwiched between the coverslip and the quartz slide as counter electrode; care was taken to avoid contact between the Pt foil and the ITO surface to prevent short circuit.

3.2.5 Normalization of Laser Intensity within Electrochemical Cell

The 532 nm laser was unevenly distributed within the excitation region, therefore fluorescent molecules at different locations may have variable emission intensities due to the different exciting laser intensities. To correct for this difference, at the end of each experiment a high concentration of resorufin solution (10~50 μM) was flowed into the electrochemical cell. 2000 frames of images were recorded at 50 ms resolution, which was later averaged into one single frame. After applying a Gaussian mask to smooth out the noisy pixels (detailed in section 3.2.6.1), this image was further normalized by the brightest pixel, generating an image that scales with the laser intensity spatial profile. All the fluorescence-intensity-related images in this work were normalized by dividing the laser profile image pixel by pixel.

3.2.6 Algorithm of Canny Edge Detection

The collected fluorescence images were sometime processed by edge detection. Edges are groups of pixels that have the most of the intensity jumps to the nearby pixels. Edge detection preserves the structural information of a given image, while reducing the total amount of data by eliminating the useless information. Therefore, it is considered as fundamentally important in image processing.⁴³ There are many algorithms in edge detection, most of which are based on taking derivatives along the x and y direction and find out the local maxima of the derivatives, thus edges. Among these algorithms, the Canny method is usually considered the optimal one and used as default in many commercial software.⁴³⁻⁴⁴ A typical Canny workflow processes the grayscale

images. It contains the following sub-routines: (1) smoothing the entire image; (2) taking the derivative along both x and y axes; (3) determining the gradient; (4) non-maximum suppression; and (5) two threshold filtering. The procedures for these sub-routines are detailed below.

3.2.6.1 Smooth the Entire Image by Applying a Gaussian Mask

The derivatives are usually sensitive to noises. All edge detection methods require a pre-smoothing in preventing taking the noises as edges. Here a Gaussian conventional mask (Eq3.4) is applied. The kernel of this Gaussian mask has a standard deviation of $\sigma = 1.4$ pixels.

$$\frac{1}{115} \begin{bmatrix} 2 & 4 & 5 & 4 & 2 \\ 4 & 9 & 12 & 9 & 4 \\ 5 & 12 & 15 & 12 & 5 \\ 4 & 9 & 12 & 9 & 4 \\ 2 & 4 & 5 & 4 & 2 \end{bmatrix} \quad (\text{Eq3.4})$$

3.2.6.2 Sobel-Operator Determined Derivative and Gradient

After smoothing, the next step is to find the gradient magnitude (G_M) by applying the Sobel-operator (e.g. a first derivative mask). The Sobel-operators along the x-axis and the y-axis take the following forms:

$$G_x = \begin{bmatrix} -1 & 0 & +1 \\ -2 & 0 & +2 \\ -1 & 0 & +1 \end{bmatrix} \quad (\text{Eq3.5})$$

$$G_y = \begin{bmatrix} +1 & +2 & +1 \\ 0 & 0 & 0 \\ -1 & -1 & -1 \end{bmatrix} \quad (\text{Eq3.6})$$

These operators assign each pixel with a gradient magnitude (G_M in Eq3.7) and a gradient direction (θ in Eq3.8).

$$G_M = \sqrt{G_x^2 + G_y^2} \quad (\text{Eq3.7})$$

$$\theta = \arctan\left(\frac{|G_y|}{|G_x|}\right) \quad (\text{Eq3.8})$$

Because images are pixelated, the gradient direction θ has to be rounded to the nearest 45° , as pointing to the 8 neighboring pixels. For example, if θ falls into the range from 112.5° - 157.5° ; it will be rounded to 135° ; as the gradient at that pixel is pointing to the top right corner (Figure 3.1).

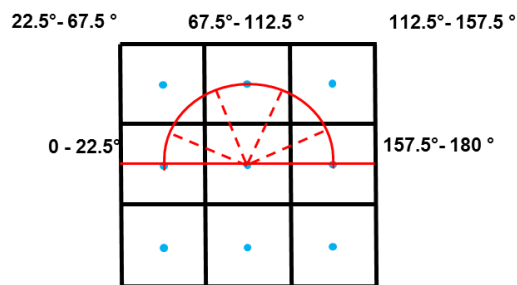


Figure 3.1 Rounding the gradient direction θ to the nearest 45° . Each square here represents a single pixel with the blue dot marking out its center position.

3.2.6.3 Applying Non-Maximum Suppression

Images composited by the gradient magnitudes have thick edges. To sharpen them, the non-maximum suppression is applied to select out the maximum magnitude along the gradient direction. In this step, each pixel's gradient magnitude is compared with its neighboring pixels

along the gradient direction. The gradient magnitude will be retained if the gradient magnitude of the current pixel is the largest; if otherwise, it will be set to zero. For example, one pixel has respectively $G_M = 7$ and $\theta = 135^\circ$ as the gradient magnitude and gradient direction. This pixel will be compared with pixels on its top right corner and bottom left corner (i.e. pixels in its 135° direction). It only gets retained when 7 is the largest G_M among the three. If not, its G_M value is mandatorily set to zero.

3.2.6.4 Edge Filtering by Low and High Thresholding

The non-maximum suppression selects out pixels that have largest intensity gradients. However, not all of the retained pixels are qualified as true edges. In the Canny method, a simple two-threshold-filter method is applied to further pick out the real edge pixels. Pixels with gradient magnitudes above the high threshold are considered the highly reliable ones, while pixels below the low threshold are considered artifacts and removed from further processing. For those pixels that fall into the range of the two thresholds, their spatial information are taken into consideration. They are retained if they are adjacent to a highly reliable edge pixel; they are removed if none of the 8 neighboring pixels is a highly reliable one. Among all steps of the Canny detection, the thresholding is usually the most critical one that determines the quality and reliability of detected edges. In this study, the thresholds for each fluorescent image was set differently, and the criterion in setting thresholds is discussed in section 3.3.5.

3.3 Results and Discussion

3.3.1 Morphology of As-Received GO under Fluorescence Quenching Microscope (FQM)

FQM was first introduced by Huang and his coworkers in studying GO, chemically reduced GO (rGO), and pristine graphene sheets.²⁶ Three different dyes, 4-(dicyanomethylene)-2-methyl-6-(4-dimethylaminostyryl)-4H-pyran (DCM), fluorescein sodium salt and 2,5-bis(5-tert-butyl-2-benzox-azolyl)thiophene (BBOT) were tested in their study, all of which were strongly quenched by GO, rGO and graphene sheet, yielding high contrast fluorescence images. Here in this study, rhodamine B was used for FQM, which has strong emission around 565 nm.⁴⁵ Figure 3.2A shows a typical fluorescence image from FQM. The spin coated rhodamine B yielded uniform emission in the blank area (i.e. places with no GO), with an average intensity around 120 (Figure 3.2B-D). The emission was quenched by GO, leading to sudden intensity drops. Much as in SEM, the absolute intensity value in FQM does not provide information about the number of GO layers. However, multiplayer GO can quench rhodamine B more effectively, resulting in higher contrasts.²⁶ It is obvious that the smallest step change is corresponding to the monolayer (Figure 3.2B), so that larger intensity changes can be assigned accordingly. For example, in Figure 3.2 monolayer GO caused an intensity change around 20 (Figure 3.2B), therefore step sizes of 40 and 60 were assigned to double layers and triple layers, respectively (Figure 3.2C and D). Moreover, because fluorescence quenching is sensitive to thickness, a piece of GO with homogeneous intensity from edge to edge is more likely monolayer, because all layers have to be perfectly aligned if being multilayer, whose probability is very low. Almost all GO examined by FQM appeared to be monolayer, with a few sheets that contained islands of multilayers. Folded sheets and wrinkles were commonly seen, as shown in Figure 3.2A.

It is worth noting that in Huang's work, the quenched emission was explained by energy transfer from the excited dye molecule to the nearby graphitic carbon. Specifically for GO, it was due to the residual graphitic domains in the basal plane that survived chemical oxidation.^{26, 46-47} However, it might not be the case for rhodamine B, because the quenching effect was absent if rhodamine B was pre-dissolved in pH 7 buffer and flow on top of GO. This observation suggests

that quenching in this study is likely due to the protonation of rhodamine B by the hydrogen containing moieties on GO.⁴⁸ This observation is critical here. Because if the energy transfer mechanism was universal to all dyes, then the resorufin molecule (**P**), product of the electrochemical reaction, will also be quenched, which would have forbidden the in situ fluorescence observation of electrocatalysis. To the contrary, no obvious quenching was observed for resorufin, regardless being flowed in with pH 7.3 phosphate buffer or spin coated on GO.

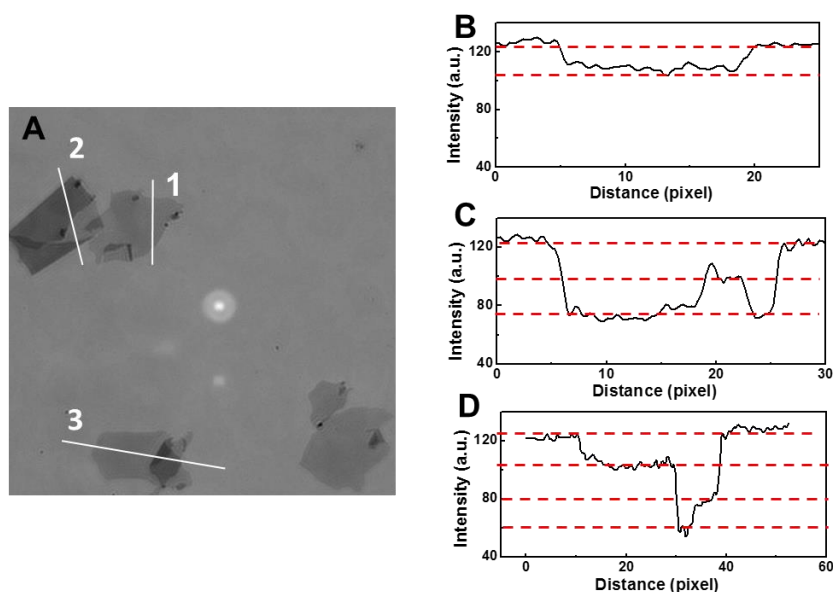


Figure 3.2 Visualizing GO by fluorescence quenching microscopy (FQM). (A) Fluorescence image of spin coated rhodamine B on a piece of glass slide with GO immobilized. 2 mL 4.5 mM rhodamine B was spin coated at 10000 rpm. A piece of clean glass slide was imaged as the background, which has been subtracted from the original image. (B, C and D) Line profiles extracted from 1, 2 and 3 from (A).

3.3.2 Ensemble GOs Electrocatalyzed Reduction of Resazurin

Our fluorogenic reaction is based on the well-known two-stage electro-reduction of the nonfluorescent molecule resazurin in aqueous solution (Figure 3.3A).⁴⁹ The first stage reduces resazurin (**S**) irreversibly to the fluorescent resorufin (**P**); the second stage reduces resorufin to the nonfluorescent dihydroresorufin (**PH₂**) and is reversible. The intense fluorescence of resorufin enables its ready detection under fluorescence microscopy at the single molecule level, as shown previously.⁴⁹⁻⁵¹

To test that GO can indeed electrochemically catalyze these transformations, cyclic voltammetry (CV) of **S** was performed on a GO coated Au electrode (Figure 3.3B). The CV of **S** shows two reduction peaks and one oxidation peak in the range of +0.3 to -0.7 V, as expected (All potentials in this chapter are referenced to the Ag/AgCl electrode). The first reduction peak does not have a corresponding oxidation peak and can be assigned as the irreversible **S** → **P** electro-reduction. The second reduction peak has a corresponding oxidation peak, thus can be assigned as the reversible **P** ↔ **PH₂** redox. Their peak separation (33 mV) at low scan rate further supports their assignments as reversible two-electron redox processes.⁵²

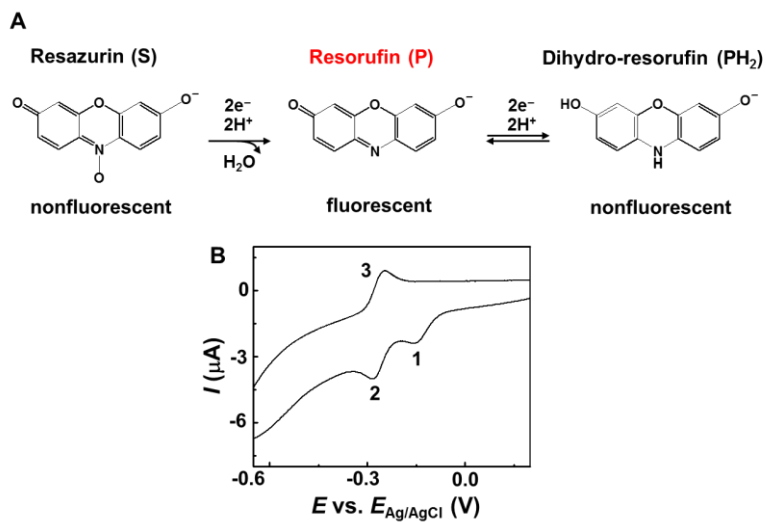


Figure 3.3 GO-catalyzed electrochemistry of resazurin. (A) Redox chemistry of resazurin in aqueous solutions. (B) Cyclic voltammogram of 50 μM resazurin in 50 mM pH 7.3 phosphate buffer with a GO-coated Au electrode at 10 mV s^{-1} scan rate.

3.3.3 Electrochemistry of GOs by Observing the Fluorescent Product Molecules

To monitor the electrocatalysis by GO at the single sheet level, an electrochemical flow cell and a wide-field total internal reflection fluorescence microscope was used. The diluted GO suspensions were deposited on a piece of ITO-coated quartz slide, which acts as the working electrode, and reaction solution containing **S** was flowed on top at a constant flow rate. The GOs were initially emissive with 532 nm laser excitation possibly due to the local conjugation structures within each sheet.⁵³⁻⁵⁴ This emission is quickly photobleached, but it enables the localization of GOs within the electrochemical flow cell. A Ag/AgCl reference electrode and a Pt counter electrode were also placed in the flow cell. The applied potential on the ITO-working electrode can effectively change the chemical potential of GOs due to their small quantum capacitances.⁵⁵⁻⁵⁹ The triangular potential waveform applied between the working electrode and reference electrode was between + 0.3 V to – 0.3 V to avoid possible electrochemical reduction of GO, because previous work by Zhou and coworkers showed that the reduction of GO on ITO substrate start from -0.6 V.³⁶ The scan rate was set at 10 mV/s, at which a complete cycle takes a total of 120 s to finish. However, by repeating the scan cycles over a long period of time, and divided the total time by the number of scans, the actual cycle time was measured at 116 s (Figure 3.4B). This cycle time was also confirmed by the synchronized fluorescence intensity response coming from GOs (Figure 3.4C). The applied potential drives the $\mathbf{S} \rightarrow \mathbf{P} \leftrightarrow \mathbf{PH}_2$ transformations as shown in Figure 3.3A. Being the only fluorescent species in this electrochemical reaction, the surface concentration of **P** is constantly changing as the potential sweeps, leading to the periodic fluctuation of fluorescence intensity on GO (Figure 3.4C), whose cycle time can be completely synchronized to the applied potential.

To test the stability of GOs, cyclic potential was applied to GOs for a total of 5 hours. The pixel-averaged fluorescence time trajectories from each individual GO all had similar shape as in Figure 3.4C. The maximum intensity within each cycle (e.g., at 116 s in Figure 3.4C) was extracted

and arranged sequentially. They were later normalized by the maximum intensity of the first cycle. The distribution of normalized maxima intensity from 20 pieces of GOs was shown in Figure 3.4D, which is symmetric around 1, and can be fitted with a Gaussian function (center at 1.00, fwhm = 0.02). This symmetric and sharp distribution indicates the maximal amount of **P** molecules on the GO in each cycle was similar and the electrochemical activity of GOs was stable for a long period of time.

Because the fluorescence response in each cycle behaved similarly to each other, the integrated fluorescent intensity from a piece of GO was averaged over many cycles to obtain an average fluorescence response in one cycle to suppress the noise (Figure 3.5B). The averaging is necessary here because the following step of taking the time derivative to generate the “fluorescence current” is sensitive to noise. The resulted fluorescence intensity versus time trajectory features two peaks and a valley in between as shown in Figure 3.5B. In the cathodic branch, initially the fluorescence intensity on GO increased slightly (on the left side, before the red circle), possibly due to some non-faradic process such as the adsorption of fluorescent species in flow.⁶⁰ As approaching the peak potential for **S** → **P** reduction (−0.159 V, Figure 3.3B), the fluorescence intensity increased dramatically as a result of **S** → **P** transformation (e.g, around 35-55 s). And eventually, the applied driving force was large enough to trigger the further reduction of **P** → **PH₂**. The first peak at 54 s in Figure 3.5B marked out the point where the **P** formation (**S** → **P**) equaled **P** consumption (**P** → **PH₂**). Beyond the first maximum point, the rate for **P** → **PH₂** surpassed the rate for **S** → **P**, leading to the decrease in fluorescence intensity. At 58 s, the potential sweep reverses in direction. But the potential was still quite negative, which made **P** → **PH₂** reaction faster than the generation of **P** (**PH₂** → **P** and **S** → **P**). As the potential became more positive, the **P** consumption rate (**P** → **PH₂**) reached an equal rate as generation, reaching the valley point at 60.5 s in fluorescence intensity trajectory. As the potential increased further, eventually all **PH₂** were converted back to **P**. The fluorescence intensity reached another peak at 72 s as there is

no corresponding reversible reaction for $\mathbf{S} \rightarrow \mathbf{P}$ (i.e. \mathbf{P} cannot be electrochemically oxidized to a nonfluorescent state within our scan range). The further decrease of fluorescent intensity was possibly due to desorption and photobleaching of \mathbf{P} .

The fluorescence intensity from a piece of GO is proportional to the total number of resorufin molecules generated, which is also proportional to the total charge passed through GO by Faraday's law. Therefore, the time derivative of the fluorescence counts could generate a response that is similar to the faradic current response.⁶⁰⁻⁶² This approach of generating "fluorescence current" has been employed by Barbara and coworkers in studying organic dye molecules,⁶¹⁻⁶² and later employed by Zhang et al in studying the resazurin/resorufin electrochemical transformation in a bipolar electrode system.⁶⁰ We, again, used the same approach to generate the "fluorescence current" by taking the time derivative of the fluorescence intensity trajectory, and the result is shown in Figure 3.5C. The time derivative represents the rate of \mathbf{P} generation on GO, which featured a valley with its lowest point at the switching potential (i.e., at 58 s). On both cathodic and anodic sides, there existed a peak, which marked out the fastest rate for $\mathbf{S} \rightarrow \mathbf{P}$ or $\mathbf{PH}_2 \rightarrow \mathbf{P}$, respectively. The positive part (i.e., $dI/dt > 0$) in Figure 3.5C stands for the period when the total amount of \mathbf{P} on GO was increasing; while the negative part (i.e., $dI/dt < 0$) stands for the period when the total amount of \mathbf{P} was decreasing. The three squares in Figure 3.5C mark out the positions where the net rate of \mathbf{P} generation equals to zero. The red square aligned with the maximum in Figure 3.5B, where the rate for $\mathbf{S} \rightarrow \mathbf{P}$ equaled that for $\mathbf{P} \rightarrow \mathbf{PH}_2$; the green square aligned with the valley point in Figure 3.5B, where the total rate of $\mathbf{S} \rightarrow \mathbf{P}$ and $\mathbf{PH}_2 \rightarrow \mathbf{P}$ equaled the rate of $\mathbf{P} \rightarrow \mathbf{PH}_2$. The purple square was when all \mathbf{PH}_2 were converted to \mathbf{P} , where no more electrochemical oxidation could take place. The validity of fluorescence current curve was further confirmed by comparing the peak positions to the conventional faraday current. The ensemble CV (Figure 3.3B) measured the peak potentials for $\mathbf{S} \rightarrow \mathbf{P}$ and $\mathbf{PH}_2 \rightarrow \mathbf{P}$ respectively at -0.159 V and -0.238 V (at the scan rate 10 mV/s). In the fluorescence current curve (Figure 3.5C), we averaged the peak potential (e.g. potentials at the red

and purple circle in Figure 3.5A) under the same scan rate from 28 pieces of individual GO sheets, and the resulted values were -0.154 V and -0.246 V respectively, which agreed with the ensemble CV reasonably well. It should be noted that the reduction peak of $\mathbf{P} \rightarrow \mathbf{PH}_2$ does not have a corresponding peak in the “fluorescence current” curve, because the resulting \mathbf{PH}_2 is nonfluorescent and thus does not respond to the electrochemical potential changes.

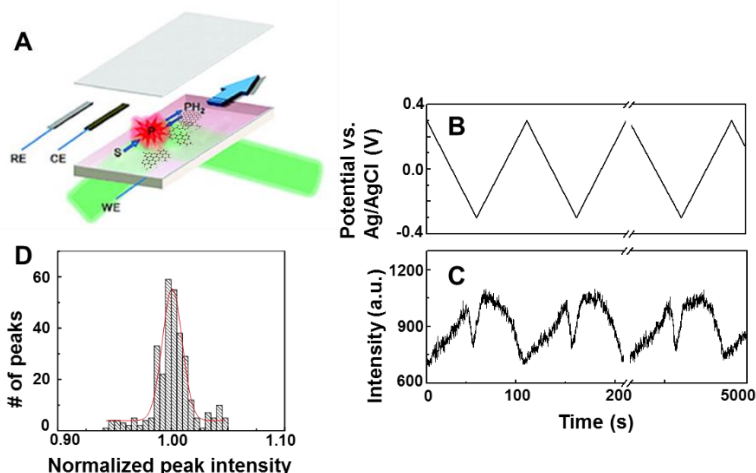


Figure 3.4 (A) Experimental scheme for the use of total internal reflection fluorescence microscopy and a flow cell to image the electrocatalysis of individual GOs. GOs are immobilized on the ITO-quartz slide with reaction solution containing **S** flowed on top. WE, RE, CE: working, reference, counter electrodes. (B) Illustration of sweeping potential versus time. The triangular potential waveform was between + 0.3 V to -0.3 V (vs. Ag/AgCl). (C) Fluorescence time trajectory. The fluorescent intensity was averaged over a 7×7 pixel area from a piece of GO. The time axes in (B) and (C) are synchronized with each other. (D) Histogram of maximum fluorescence intensity from each cycle. Data were collected from a total of 20 individual GO. For each GO, the fluorescence time trajectory was first extract as in (C). The maximum intensity was then extracted for each cycle and normalized by the first maximum. Solid red line on top is a Gaussian fit centered at 1.008. (A) is adapted from Xu et al.⁴⁹ Copy right 2009 American Chemical Society.

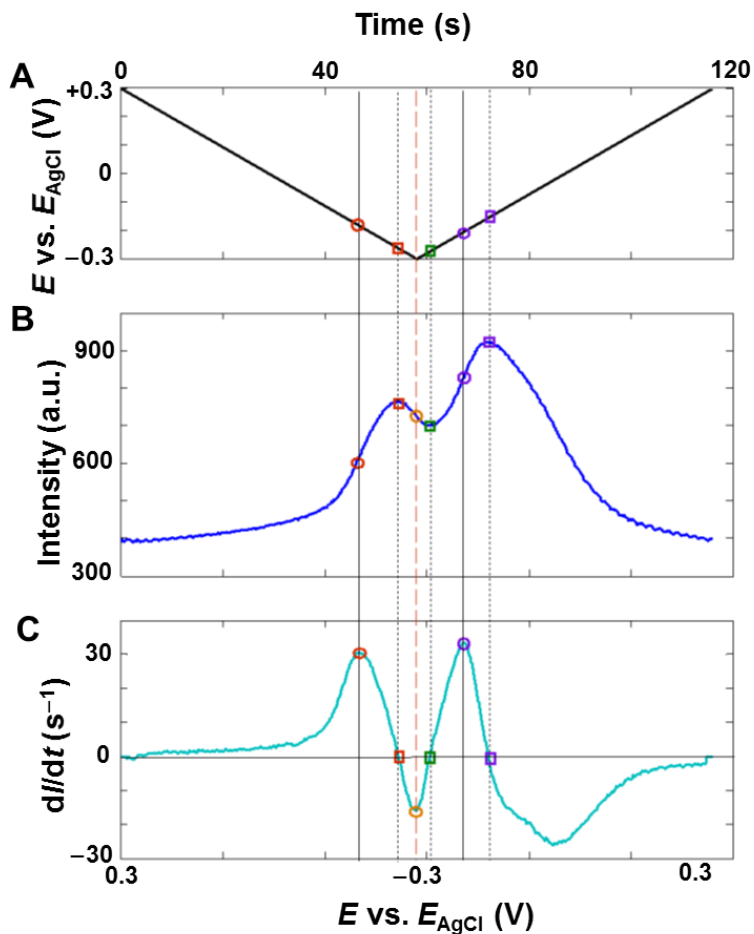


Figure 3.5 (A) Triangular potential waveform (+0.3 V to -0.3 V vs. Ag/AgCl, 10 mV/s). (B) The fluorescence intensity response from a piece of GO as the potential in (A) was applied. The integrated intensity from the entire GO was first averaged for 22 complete scans, and then averaged by the number of pixels within the GO. (C) The time derivative of fluorescence intensity shown in (B).

3.3.4 Electrochemical Fluorescence Imaging of GOs and Mapping The Sub-Structures

In the previous section, fluorescence time trajectory and its time derivative were extracted from a piece of GO. The same approach can be applied at the single pixel level to reconstruct the electrochemical activity map. In brief, the fluorescence intensity versus time trajectory was extracted from each camera pixel. The pixel based trajectories all have similar shapes as in Figure 3.5B, which featured two peaks; and the maximum value for the second peak was used to generate the reconstructed image. Figure 3.6A shows one example of the reconstructed fluorescence image, in which a piece of GO is clearly seen. The high contrast in the reconstructed image indicates that first the intensity from ITO and GO were distinctly different; moreover, more **P** molecules were generated within wrinkles and folded-over regions than the single sheet region. In other words, the wrinkles and folds are electrochemically more active. The fluorescence time trajectory contained two peaks and one valley (Figure 3.5B). Both peaks and valley can be used to generate the reconstructed fluorescence images and they resulted in similar images. The intensity from the second peak was chosen mainly because it has the greatest absolute value among the three, thus highest contrast versus the ITO area can be achieved.

To map out features within the reconstructed fluorescence image, Canny edge detection was applied. In this method, two thresholds were set in order to differentiate the true edge from the artifacts. Although the absolute value for the two thresholds varied from GO to GO, a consistent standard was used to ensure the reproducibility in edge detection. Since the GO was immobilized on ITO, each GO should have a distinct boundary line that differentiates the sheet from the ITO substrate. The purpose of the high threshold is to select out the most reliable edges. It was set as large as possible, while maintaining the successful detection of boundary lines. Figure 3.6B is an example with inappropriate high-threshold. The value was set too high that part of the boundary line is missing. On the other hand, the purpose of the low threshold is to filter out the artifacts while maintaining enough of the details. Its value was set as small as possible until non-existing features from the blank ITO area are picked (Figure 3.6D). Shown in Figure 3.6C is an example of proper

thresholding: the high threshold displayed majority of the boundary line while the low threshold filtered out the noise signal from the ITO area.

Due to the diffraction limit, the real edge (e.g. boundary of GO, wrinkles) could be anywhere within the range of a point spread function (PSF). Therefore, the detected edge lines from the reconstruction fluorescence image might not be the physical edges of GOs. To account for this diffraction limit induced difference, each pixel within the detected edges was expanded so that the true physical edges are included in this range. The theoretical Rayleigh criterion for our microscope is $\text{Resolution}_{x,y} = 0.61 \times \frac{\lambda}{\text{N.A.}} \approx 280 \text{ nm}$ (λ : 550–610 nm; N.A.: 1.2), roughly equal to the pixel size of our camera (266.7 nm under 60X objective). However, using 6 nm Au nanoparticle as a point object, our measurement suggested the real optical resolution for our microscope was $\sim 430 \text{ nm}$.⁶³ Under this resolution, a single pixel would have been expanded into a 3 by 3 area (Figure 3.6E, within the inner circle). On the safe end, we expanded each pixel to 1.5x of the optical resolution (Figure 3.6E, outer circle), and the final expansion pattern for each pixel is shown in Figure 3.6F, colored in gray. By applying the pixel expansion to the entire edge, the slim edge lines were expanded to edge regions. The outer most part was considered as the boundary region (Figure 3.6G); the inner part was considered as the wrinkle region (Figure 3.6H); and the remaining part was considered as the sheet region (Figure 3.6I). It is worth noting that the physical boundary of GO, once folded over, is considered part of the wrinkle in our region definition, because GOs usually have complex morphology on substrate and our method lacks enough resolution to further dissect the features within them. The sheet region might contain the monolayers, multilayers and folded-over GO for the same reason.

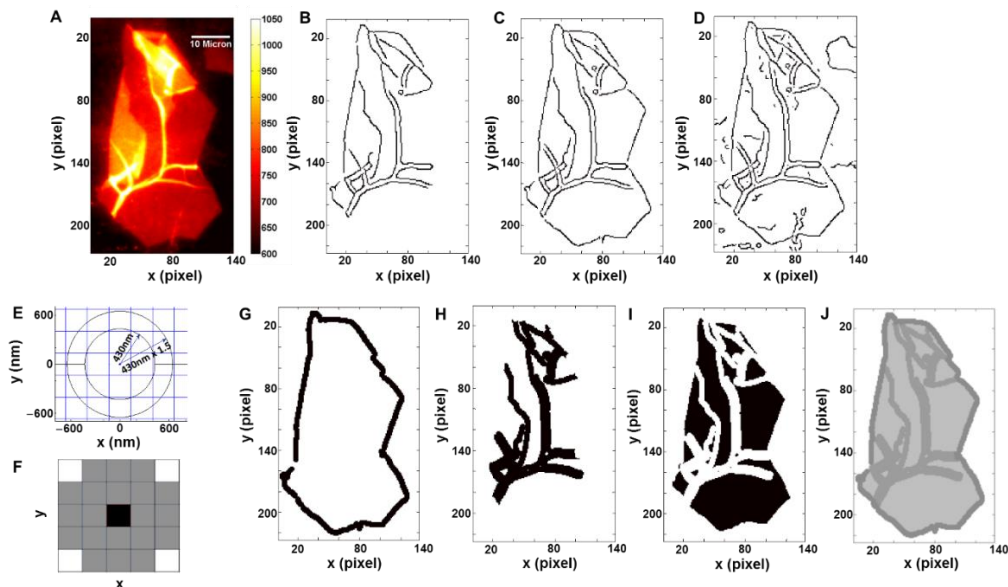


Figure 3.6 Electrochemical fluorescence imaging of GO. (A) Reconstructed fluorescence image of GO. (B-D) Illustration of double thresholding in Canny edge detection. (B, D) Examples of inappropriate thresholding. Real edges were missed when the high-threshold was too high (B); and noise signal picked up in the ITO region when the low-threshold was too low (D). (C) An example of setting both thresholds properly. (E) Illustration of diffraction limit on a pixelated image. (F) Pattern of pixel expansion based on the diffraction limit. Black: the real pixel; Gray: the surrounding pixels possibly covered because of diffraction limit. (G-J) Expanding the detected edges into boundary region (G), wrinkle region (H) and sheet region (I). The region-divided GO is shown in (J) with sheet region in pale gray and boundary/wrinkle in dark gray.

3.3.5 Electrochemical Reduction and Activity change

The as-synthesized GOs usually have carbon/oxygen ratio around 2/1, thus behave like insulators.^{11, 18} To use them in electronic related applications, the common strategy is to reduce GO into reduced graphene oxide (rGO), which is a conductive material.⁵ Here we studied the electrocatalytic activity changes of GO upon electrochemical reduction. As detailed in previous section, the electrochemical fluorescence imaging was first applied to as-received GO by applying triangular wave potential between +0.3 V to -0.3 V. This process is referred as stage 1 in later paragraphs, which generates the reconstructed image of GOs. This image might reflect the density of active sites within each GO sheet, since the reconstruction is based on the peak intensity of each pixel, and the intensity is proportional to the number of on-site generated **P** molecules. In stage 2, a constant potential was applied for 1 h to partially reduce the GO; and followed by stage 3, where another triangular wave potential (+0.3 V to -0.3 V) was applied to obtain the reconstructed fluorescent image after the electrochemical reduction. Three reduction potential (-0.7 V, -0.8 V and -0.9 V) were examined for stage 2 treatment, with each applied to a different set of GOs.

The fluorescence-intensity-represented-activity-change was analyzed region by region, because sub-populations, if present, may be concealed since the intensity for an entire GO usually distribute over a wide range. Depending on the reduction potential, the reconstructed images for partially reduced GO were distinctly different. Reduction under -0.7 V for 1 h did not affect the intensity reconstructed image much; and as a result, pixels within boundary, wrinkle and sheet regions (Figure 3.7B, C and D) all fell into the diagonal line in the intensity scatter plot (i.e. maximum intensity after the electrochemical reduction almost remained the same). The intensity histograms in stage 1 and 3 clearly show that there are subpopulations. They were separated by fitting the histograms with Gaussian peaks and divided at the crossing points. Each of the subpopulations was colored with an individual color, and surprisingly, pixels within the same subpopulation were continuous over space rather than intermingled with other subpopulations. Based on the absolute fluorescent intensity after electrochemical reduction (i.e. the absolute

intensity value in stage 3), subpopulations across the boundary, wrinkle and sheet regions were regrouped, forming domains (Figure 3.7E).

On the other hand, intensity reconstructed images of GOs behave drastically different when reduction was carried out at -0.8 V or -0.9 V. Shown in Figure 3.7(F)-(J) is a piece of GO reduced under -0.9 V for 1 h. The majority of the pixels showed a clear intensity drop after the reduction, which corresponds to the distance shifted away from the diagonal line in the scatter plot, and the subpopulations were divided based on the amount of intensity shifts (Figure 3.7G, H and I). Again, continuous domains were formed by grouping the subpopulations across different regions based on their absolute intensities in stage 3 (Figure 3.7J). The domain definition here for Figure 3.7J, however, is different from Figure 3.7E. In Figure 3.7E domains are groups of pixels that have similar intensities, while in Figure 3.7J domains represent pixels that have similar resistance to the electrochemical reduction. For example, the red-colored domain in Figure 3.7J represents the part of GO that can resist the electrochemical reduction the most, since they shift the least from the diagonal line, while the blue-colored domain represents the part of GO that has been affected the most, since they have the largest shift from the diagonal line. At this moment, it is still unclear to us how these domains were initially formed on GO and what are their chemical nature. One possibility here is that the division lines between the neighboring domains are the grain boundaries. However, correct assignments would require correlation with structural measurements on the same piece of GO.

The fluorescence time trajectory for a single pixel was usually very noisy. Consequently, its time derivative, the “fluorescence current” became unreliable. However, by averaging all pixels that belong to the same region, the final fluorescence time trajectories were smooth which enabled the extraction of the “fluorescence current”. Thus we analyzed the region-based fluorescence current change upon electrochemical reduction, and the results are shown in Table 1. In general, the initial peak potential for boundary, wrinkle and sheet regions were similar to each other, except for the $S \rightarrow P$ reduction potential of boundary region. This is possibly because regions were defined

by expanding the edge lines, which lacks the spatial resolution so that the wrinkle region would also include large portion of sheets and result in similar peak potential for both regions. As for the boundary region, part of the ITO substrate was also included in averaging, which might cause the shift in peak potential. Moreover, the cathodic peak potential became more negative while anodic peak potential became more positive, indicating larger driving forces were needed after the electrochemical reduction. The increment in driving force was also dependent on the reduction potential, where -0.7 V reduction resulted in relatively smaller shifts and -0.9 V reduction resulted in the largest shifts. The potential shifts here could be due to the change of chemical nature of active sites on GOs.

Opposite to the decrease behavior of maximum fluorescence intensity (Figure 3.7), the magnitude in time derivative increased for the majority of GOs. This is probably because the maximum fluorescence intensity is proportional to the density of active sites, while the time derivation, reflecting the rate of **P** generation, not only dependent on the active site density, but also dependent on the per-site reactivity. The electrochemical reduction although decreased the active site density, may have increased the reactivity of each site.

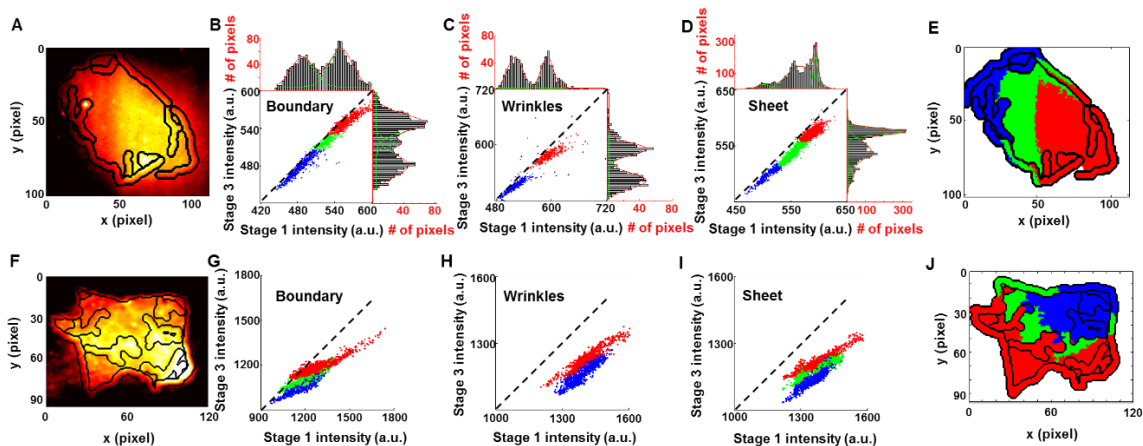


Figure 3.7 Fluorescence intensity represented electrocatalytic activity change upon electrochemical reduction. (A)-(E) A piece of GO reduced under a steady -0.7 V potential for 1 h. (F)-(J) Another piece of GO reduced under a steady -0.9 V potential for 1 h. Dotted lines in B-D and G-I are diagonal lines. (A, F) The reconstructed fluorescence image of GO. Solid black lines on top are the expanded edge lines that separate the boundary, wrinkle and sheet regions. (B-D and G-I) 2D scatter plots of peak intensity before (x-axis) and after (y-axis) the electrochemical reduction respectively for the pixels within the boundary region (B, G), wrinkle region (C, H) and sheet region (E, J). Sub-population in each regions are colored in blue, green and red. (E, J) False color image of GO correspond to (A) and (F). Each color represents a different domain, which is composed by combining sub-population from boundary, wrinkle and sheet regions as described in the text. The pixel size in (A, E, F and J) is 267 nm.

Table 1. Peak potential changes upon electrochemical reduction from the fluorescence current curve as in Figure 3.5^a

Region	Stage 1	Stage 3 peak potential (V)		
	Peak potential (V)	-0.7 V	-0.8 V	-0.9 V
Boundary	-0.164±0.004	-0.162±0.007	-0.183±0.004	-0.173±0.005
	-0.248±0.002	-0.207±0.009	-0.193±0.007	-0.191±0.002
Wrinkles	-0.151±0.005	-0.154±0.009	-0.177±0.006	-0.167±0.008
	-0.246±0.002	-0.204±0.010	-0.195±0.006	-0.185±0.006
Sheet	-0.154±0.005	-0.153±0.007	-0.180±0.004	-0.168±0.004
	-0.247±0.002	-0.205±0.010	-0.197±0.005	-0.189±0.002

^a Column 1 specifies each region. Column 2 shows the original peak potentials, and column 3-5 are the peak potentials after electrochemical reduction. Peak potential for **S** → **P** are shown on top in each cell, while **PH₂** → **P** are shown on bottom. Errors are s.e.m.

3.3.6 The Electrochemical Activity Changes of GO in Multistage Reduction

To observe the changes of electrocatalytic activity more closely, multistage reduction treatments were performed on GO. The fluorescence intensity reconstructed image was first generated to represent the initial electrochemical activity of as-received GO (Figure 3.8B). Then, a constant -0.9 V potential was applied for 20 minutes every time, with each followed by another cyclic voltammetry to obtain the intensity reconstructed image. Four reduction stages were carried out on GO, which gave a total of 80 min reduction time and generated 5 reconstructed images. In these reconstructed images, the fluorescence intensity at each image pixel followed an exponential decay behavior (Figure 3.8A). An empirical equation $I = A \cdot e^{-kt} + I_0$ was used to fit each pixel, where the A is a prefactor, k is the decay constant, t is the number of electrochemical reduction and I_0 is the intensity offset. A decay map for entire GO was generated by reconstructing the decay constant k from every single pixel (Figure 3.8C). It turned out that there exist discrete sites where the decay rates were much faster than the rest of the sheet. And by examining the spatial locations of these discrete sites, it seems that electrochemical reduction preferentially started from boundaries and wrinkles.

3.3.7 Raman Spectrum Correlated Activity Measurement

Raman spectra were measured at various different locations on GOs to better understand the structure-activity correlation. The same pieces of sheets were later put under our optical microscope to correlate with electrocatalytic activity measurements. The high-intensity laser used in Raman destroyed the GO at focus points, leaving dark spots in intensity reconstructed images, which can facilitate the spatial correlation of Raman spectra with the activity measurements. The typical Raman spectrum of GO contains two groups of peaks. One is around $1300\sim 1600$ cm^{-1} (G and D band), and the other is around $3200\sim 3400$ cm^{-1} (2D band). It is reported that the increase of oxygen functionalities causes the shift of Raman G band to lower wavenumbers. In our

measurements, the boundary regions redshift the most from the pristine graphene sheets, while wrinkles and flat sheets had almost the same Raman frequencies. These results indicate that the GO boundary region is most abundant in oxygen containing functionalities, as expected.

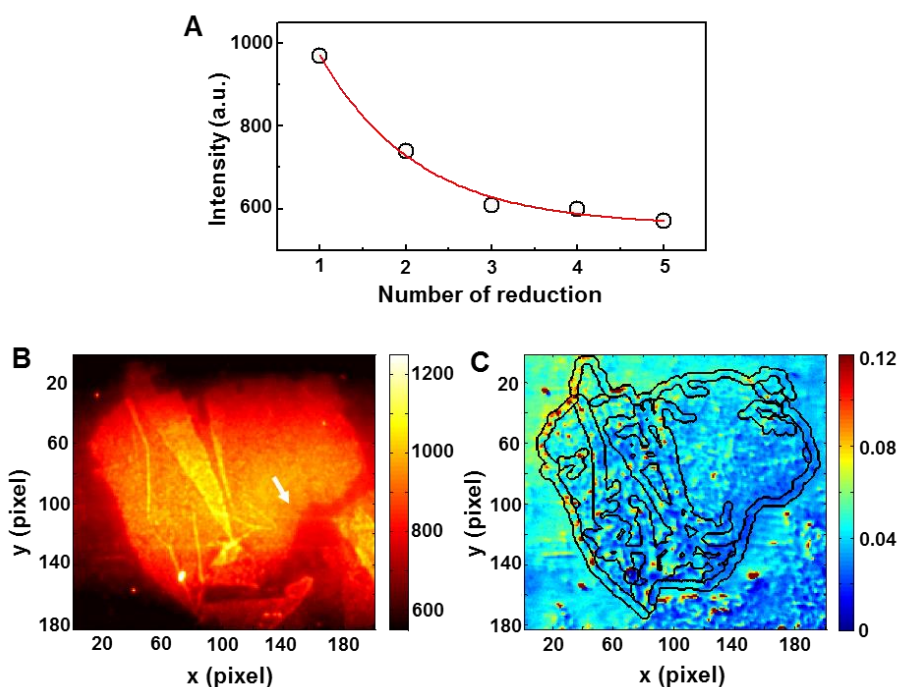


Figure 3.8 The electrochemical activity change of GO by stepwise reduction. (A) Maximum intensity change of a single pixel versus the number of reduction steps. Solid red line is a fit with the empirical equation $I = A \cdot e^{-kt} + I_0$. (B) The fluorescent intensity reconstructed image of as-received GO. Trace in (A) is extracted from the pixel marked out by the white arrow in (B). (C) The reconstructed image using the decay constant k . Solid black lines separate the boundary region and wrinkle region from the sheet.

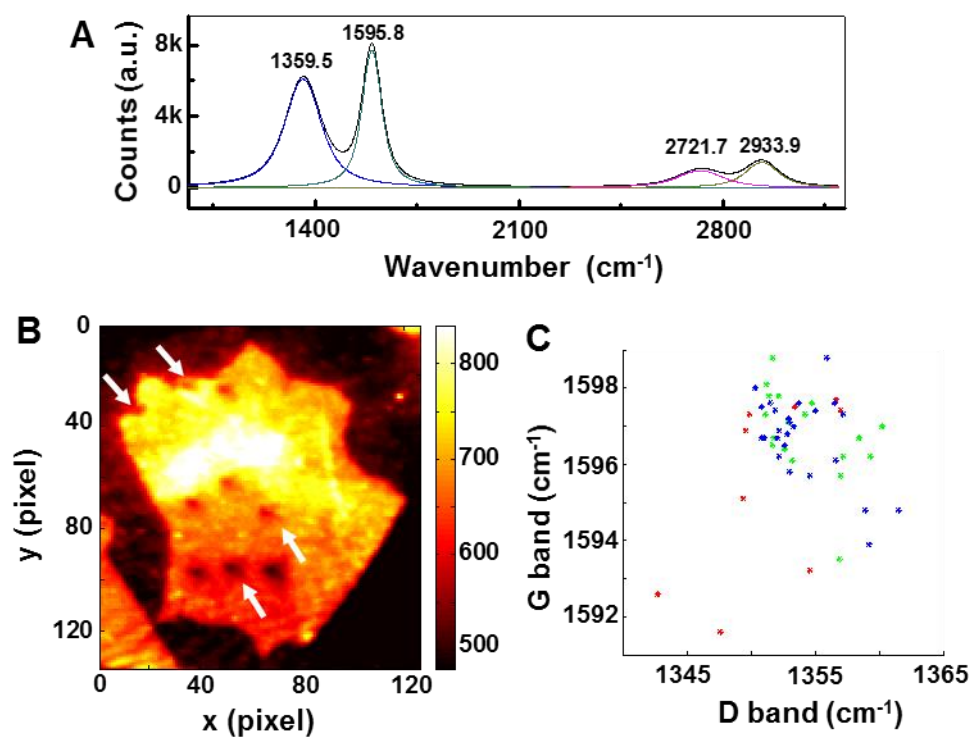


Figure 3.9 (A) Typical Raman spectrum from GO. (B) The intensity reconstructed image of GO after taking micro-Raman spectra at multiple locations. Spectra were collected from the positions of the spherical dark spots (e.g. positions marked by white arrows). (C) Scatter plot of G band versus D band. The red, green and blue color represent boundary, wrinkle and sheet respectively.

3.4 References

1. Rao, C. N. R.; Sood, A. K.; Subrahmanyam, K. S.; Govindaraj, A., Graphene: The New Two-Dimensional Nanomaterial. *Angewandte Chemie International Edition* **2009**, *48* (42), 7752-7777.
2. Geim, A. K.; Novoselov, K. S., The rise of graphene. *Nat Mater* **2007**, *6* (3), 183-191.
3. Sykes, E. C. H., Surface assembly: Graphene goes undercover. *Nat Chem* **2009**, *1* (3), 175-176.
4. Li, D.; Kaner, R. B., Graphene-Based Materials. *Science* **2008**, *320* (5880), 1170-1171.
5. Huang, X.; Yin, Z.; Wu, S.; Qi, X.; He, Q.; Zhang, Q.; Yan, Q.; Boey, F.; Zhang, H., Graphene-Based Materials: Synthesis, Characterization, Properties, and Applications. *Small* **2011**, *7* (14), 1876-1902.
6. Pumera, M., Graphene-based nanomaterials and their electrochemistry. *Chemical Society Reviews* **2010**, *39* (11), 4146-4157.
7. Novoselov, K. S.; Geim, A. K.; Morozov, S. V.; Jiang, D.; Zhang, Y.; Dubonos, S. V.; Grigorieva, I. V.; Firsov, A. A., Electric Field Effect in Atomically Thin Carbon Films. *Science* **2004**, *306* (5696), 666-669.
8. Novoselov, K. S., Two-dimensional atomic crystals. *Proceedings of the National Academy of Sciences* **2005**, *102* (30), 10451-10453.
9. Castro Neto, A. H.; Guinea, F.; Peres, N. M. R.; Novoselov, K. S.; Geim, A. K., The electronic properties of graphene. *Reviews of Modern Physics* **2009**, *81* (1), 109-162.
10. Geim, A. K., Graphene: Status and Prospects. *Science* **2009**, *324* (5934), 1530-1534.
11. Chen, D.; Feng, H.; Li, J., Graphene Oxide: Preparation, Functionalization, and Electrochemical Applications. *Chemical Reviews* **2012**, *112* (11), 6027-6053.
12. Dreyer, D. R.; Park, S.; Bielawski, C. W.; Ruoff, R. S., The chemistry of graphene oxide. *Chemical Society Reviews* **2010**, *39* (1), 228-240.
13. Eda, G.; Chhowalla, M., Chemically Derived Graphene Oxide: Towards Large-Area Thin-Film Electronics and Optoelectronics. *Advanced Materials* **2010**, *22* (22), 2392-2415.
14. Gómez-Navarro, C.; Weitz, R. T.; Bittner, A. M.; Scolari, M.; Mews, A.; Burghard, M.; Kern, K., Electronic Transport Properties of Individual Chemically Reduced Graphene Oxide Sheets. *Nano Letters* **2007**, *7* (11), 3499-3503.
15. Stankovich, S.; Dikin, D. A.; Piner, R. D.; Kohlhaas, K. A.; Kleinhammes, A.; Jia, Y.; Wu, Y.; Nguyen, S. T.; Ruoff, R. S., Synthesis of graphene-based nanosheets via chemical reduction of exfoliated graphite oxide. *Carbon* **2007**, *45* (7), 1558-1565.
16. Scheuermann, G. M.; Rumi, L.; Steurer, P.; Bannwarth, W.; Mülhaupt, R., Palladium

Nanoparticles on Graphite Oxide and Its Functionalized Graphene Derivatives as Highly Active Catalysts for the Suzuki–Miyaura Coupling Reaction. *Journal of the American Chemical Society* **2009**, *131* (23), 8262-8270.

17. Wang, Y.; Li, Z.; Wang, J.; Li, J.; Lin, Y., Graphene and graphene oxide: biofunctionalization and applications in biotechnology. *Trends in Biotechnology* **2011**, *29* (5), 205-212.
18. Zhu, Y.; Murali, S.; Cai, W.; Li, X.; Suk, J. W.; Potts, J. R.; Ruoff, R. S., Graphene and Graphene Oxide: Synthesis, Properties, and Applications. *Advanced Materials* **2010**, *22* (35), 3906-3924.
19. Sharma, R.; Baik, J. H.; Perera, C. J.; Strano, M. S., Anomalously Large Reactivity of Single Graphene Layers and Edges toward Electron Transfer Chemistries. *Nano Letters* **2010**, *10* (2), 398-405.
20. Ding, W.; Dikin, D. A.; Chen, X.; Piner, R. D.; Ruoff, R. S.; Zussman, E.; Wang, X.; Li, X., Mechanics of hydrogenated amorphous carbon deposits from electron-beam-induced deposition of a paraffin precursor. *Journal of Applied Physics* **2005**, *98* (1), -.
21. Vldar, A.; Postek, M., Electron Beam-Induced Sample Contamination in the SEM. *Microscopy and Microanalysis* **2005**, *11* (SupplementS02), 764-765.
22. Yu, Q.; Jauregui, L. A.; Wu, W.; Colby, R.; Tian, J.; Su, Z.; Cao, H.; Liu, Z.; Pandey, D.; Wei, D.; Chung, T. F.; Peng, P.; Guisinger, N. P.; Stach, E. A.; Bao, J.; Pei, S.-S.; Chen, Y. P., Control and characterization of individual grains and grain boundaries in graphene grown by chemical vapour deposition. *Nat Mater* **2011**, *10* (6), 443-449.
23. Ferrari, A. C.; Basko, D. M., Raman spectroscopy as a versatile tool for studying the properties of graphene. *Nat Nano* **2013**, *8* (4), 235-246.
24. Azevedo, J.; Bourdillon, C.; Derycke, V.; Campidelli, S.; Lefrou, C.; Cornut, R., Contactless Surface Conductivity Mapping of Graphene Oxide Thin Films Deposited on Glass with Scanning Electrochemical Microscopy. *Analytical Chemistry* **2012**, *85* (3), 1812-1818.
25. Rodríguez-López, J.; Ritzert, N. L.; Mann, J. A.; Tan, C.; Dichtel, W. R.; Abruña, H. D., Quantification of the Surface Diffusion of Tripodal Binding Motifs on Graphene Using Scanning Electrochemical Microscopy. *Journal of the American Chemical Society* **2012**, *134* (14), 6224-6236.
26. Kim, J.; Cote, L. J.; Kim, F.; Huang, J., Visualizing Graphene Based Sheets by Fluorescence Quenching Microscopy. *Journal of the American Chemical Society* **2009**, *132* (1), 260-267.
27. Jung, I.; Pelton, M.; Piner, R.; Dikin, D. A.; Stankovich, S.; Watcharotone, S.; Hausner, M.; Ruoff, R. S., Simple Approach for High-Contrast Optical Imaging and Characterization of Graphene-Based Sheets. *Nano Letters* **2007**, *7* (12), 3569-3575.
28. Gilje, S.; Han, S.; Wang, M.; Wang, K. L.; Kaner, R. B., A Chemical Route to Graphene for Device Applications. *Nano Letters* **2007**, *7* (11), 3394-3398.
29. Si, Y.; Samulski, E. T., Synthesis of Water Soluble Graphene. *Nano Letters* **2008**, *8* (6),

1679-1682.

30. Bourlinos, A. B.; Gournis, D.; Petridis, D.; Szabó, T.; Szeri, A.; Dékány, I., Graphite Oxide: Chemical Reduction to Graphite and Surface Modification with Primary Aliphatic Amines and Amino Acids. *Langmuir* **2003**, *19* (15), 6050-6055.
31. Wang, G.; Yang, J.; Park, J.; Gou, X.; Wang, B.; Liu, H.; Yao, J., Facile Synthesis and Characterization of Graphene Nanosheets. *The Journal of Physical Chemistry C* **2008**, *112* (22), 8192-8195.
32. Wang, X.; Zhi, L.; Müllen, K., Transparent, Conductive Graphene Electrodes for Dye-Sensitized Solar Cells. *Nano Letters* **2007**, *8* (1), 323-327.
33. Becerril, H. A.; Mao, J.; Liu, Z.; Stoltenberg, R. M.; Bao, Z.; Chen, Y., Evaluation of Solution-Processed Reduced Graphene Oxide Films as Transparent Conductors. *ACS Nano* **2008**, *2* (3), 463-470.
34. Zhu, Y.; Stoller, M. D.; Cai, W.; Velamakanni, A.; Piner, R. D.; Chen, D.; Ruoff, R. S., Exfoliation of Graphite Oxide in Propylene Carbonate and Thermal Reduction of the Resulting Graphene Oxide Platelets. *ACS Nano* **2010**, *4* (2), 1227-1233.
35. Pei, S.; Cheng, H.-M., The reduction of graphene oxide. *Carbon* **2012**, *50* (9), 3210-3228.
36. Zhou, M.; Wang, Y.; Zhai, Y.; Zhai, J.; Ren, W.; Wang, F.; Dong, S., Controlled Synthesis of Large-Area and Patterned Electrochemically Reduced Graphene Oxide Films. *Chemistry – A European Journal* **2009**, *15* (25), 6116-6120.
37. An, S. J.; Zhu, Y.; Lee, S. H.; Stoller, M. D.; Emilsson, T.; Park, S.; Velamakanni, A.; An, J.; Ruoff, R. S., Thin Film Fabrication and Simultaneous Anodic Reduction of Deposited Graphene Oxide Platelets by Electrophoretic Deposition. *The Journal of Physical Chemistry Letters* **2010**, *1* (8), 1259-1263.
38. Ramesha, G. K.; Sampath, S., Electrochemical Reduction of Oriented Graphene Oxide Films: An in Situ Raman Spectroelectrochemical Study. *The Journal of Physical Chemistry C* **2009**, *113* (19), 7985-7989.
39. Wang, Z.; Zhou, X.; Zhang, J.; Boey, F.; Zhang, H., Direct Electrochemical Reduction of Single-Layer Graphene Oxide and Subsequent Functionalization with Glucose Oxidase. *The Journal of Physical Chemistry C* **2009**, *113* (32), 14071-14075.
40. Cote, L. J.; Kim, F.; Huang, J., Langmuir–Blodgett Assembly of Graphite Oxide Single Layers. *Journal of the American Chemical Society* **2008**, *131* (3), 1043-1049.
41. Hummers, W. S.; Offeman, R. E., Preparation of Graphitic Oxide. *Journal of the American Chemical Society* **1958**, *80* (6), 1339-1339.
42. Stankovich, S.; Dikin, D. A.; Dommett, G. H. B.; Kohlhaas, K. M.; Zimney, E. J.; Stach, E. A.; Piner, R. D.; Nguyen, S. T.; Ruoff, R. S., Graphene-based composite materials. *Nature* **2006**, *442* (7100), 282-286.
43. Canny, J., A Computational Approach to Edge Detection. *IEEE Trans. Pattern Anal. Mach.*

Intell. **1986**, 8 (6), 679-698.

44. Mai, F.; Hung, Y. S.; Zhong, H.; Sze, W. F., A hierarchical approach for fast and robust ellipse extraction. *Pattern Recognition* **2008**, 41 (8), 2512-2524.
45. Kubin, R. F.; Fletcher, A. N., Fluorescence quantum yields of some rhodamine dyes. *Journal of Luminescence* **1982**, 27 (4), 455-462.
46. Nakajima, T.; Mabuchi, A.; Hagiwara, R., A new structure model of graphite oxide. *Carbon* **1988**, 26 (3), 357-361.
47. Lerf, A.; He, H.; Forster, M.; Klinowski, J., Structure of Graphite Oxide. *The Journal of Physical Chemistry B* **1998**, 102 (23), 4477-4482.
48. Moreno-Villoslada, I.; Jofré, M.; Miranda, V.; González, R.; Sotelo, T.; Hess, S.; Rivas, B. L., pH Dependence of the Interaction between Rhodamine B and the Water-Soluble Poly(sodium 4-styrenesulfonate). *The Journal of Physical Chemistry B* **2006**, 110 (24), 11809-11812.
49. Xu, W.; Shen, H.; Kim, Y. J.; Zhou, X.; Liu, G.; Park, J.; Chen, P., Single-Molecule Electrocatalysis by Single-Walled Carbon Nanotubes. *Nano Letters* **2009**, 9 (12), 3968-3973.
50. Xu, W.; Kong, J. S.; Yeh, Y.-T. E.; Chen, P., Single-molecule nanocatalysis reveals heterogeneous reaction pathways and catalytic dynamics. *Nat Mater* **2008**, 7 (12), 992-996.
51. Han, K. S.; Liu, G.; Zhou, X.; Medina, R. E.; Chen, P., How Does a Single Pt Nanocatalyst Behave in Two Different Reactions? A Single-Molecule Study. *Nano Letters* **2012**, 12 (3), 1253-1259.
52. Bard, A. J.; Faulkner, L. R., *Electrochemical Methods: Fundamentals and Applications*. Wiley: 2000.
53. Cushing, S. K.; Li, M.; Huang, F.; Wu, N., Origin of Strong Excitation Wavelength Dependent Fluorescence of Graphene Oxide. *ACS Nano* **2013**, 8 (1), 1002-1013.
54. Thomas, H. R.; Valles, C.; Young, R. J.; Kinloch, I. A.; Wilson, N. R.; Rourke, J. P., Identifying the fluorescence of graphene oxide. *Journal of Materials Chemistry C* **2013**, 1 (2), 338-342.
55. Xu, H.; Zhang, Z.; Wang, Z.; Wang, S.; Liang, X.; Peng, L.-M., Quantum Capacitance Limited Vertical Scaling of Graphene Field-Effect Transistor. *ACS Nano* **2011**, 5 (3), 2340-2347.
56. Heller, I.; Kong, J.; Heering, H. A.; Williams, K. A.; Lemay, S. G.; Dekker, C., Individual Single-Walled Carbon Nanotubes as Nanoelectrodes for Electrochemistry. *Nano Letters* **2004**, 5 (1), 137-142.
57. Heller, I.; Kong, J.; Williams, K. A.; Dekker, C.; Lemay, S. G., Electrochemistry at Single-Walled Carbon Nanotubes: The Role of Band Structure and Quantum Capacitance. *Journal of the American Chemical Society* **2006**, 128 (22), 7353-7359.
58. Trung, T. Q.; Tien, N. T.; Kim, D.; Jang, M.; Yoon, O. J.; Lee, N.-E., A Flexible Reduced Graphene Oxide Field-Effect Transistor for Ultrasensitive Strain Sensing. *Advanced Functional*

Materials **2014**, *24* (1), 117-124.

59. Standley, B.; Mendez, A.; Schmidgall, E.; Bockrath, M., Graphene–Graphite Oxide Field-Effect Transistors. *Nano Letters* **2012**, *12* (3), 1165-1169.

60. Guerrette, J. P.; Percival, S. J.; Zhang, B., Fluorescence Coupling for Direct Imaging of Electrocatalytic Heterogeneity. *Journal of the American Chemical Society* **2012**, *135* (2), 855-861.

61. Andre J. Gesquiere, S.-J. P., and Paul F. Barbara, F-V/SMS: A New Technique for Studying the Structure and Dynamics of Single Molecules and Nanoparticles. *J. Phys. Chem. B* **2004**, *108* 10301-10308.

62. Andre J. Gesquiere, T. U., Tsuyoshi Asahi, Hiroshi Masuhara, and Paul F. Barbara, Single Molecule Spectroscopy of Organic Dye Nanoparticles. *Nano Lett.* **2005**, *5*, 1321-1325.

63. Zhou, X.; Andoy, N. M.; Liu, G.; Choudhary, E.; Han, K.-S.; Shen, H.; Chen, P., Quantitative super-resolution imaging uncovers reactivity patterns on single nanocatalysts. *Nat Nano* **2012**, *7* (4), 237-241.

CHAPTER FOUR

SINGLE-MOLECULE ELECTROCATALYSIS ON ALIGNED ARRAYS OF SINGLE-WALLED CARBON NANOTUBES

4.1 Introduction

Single-walled carbon nanotubes (SWNTs), since first discovered by Iijima and Bethune in 1993,¹⁻² received great attention for their extraordinary structural, mechanical and electronic properties. The applications of SWNTs in the past two decades include nano-sized electronics, opto-electronics, catalysis, and sensors.³⁻⁹ Among these applications, the energy related electrochemistry and electrocatalysis became promising because of the one-dimensional nature of SWNTs leading to high specific surface area and large enhancement in the rate of mass transport and electron transfer.¹⁰⁻¹⁴ Therefore, the fundamental understanding of SWNTs in electrochemical processes is important for tailoring their structures for optimal performances.

Synthesizing monodispersed SWNTs is a persistent challenge.^{9, 15} The current preparation methods always generate SWNTs with chirality dispersion. The chirality dispersion leads to dispersion in electronic properties, which increases the difficulties in quantitatively characterizing the SWNTs electrochemical and electrocatalytic properties. To circumvent this problem, Crooks, Dekker and coworkers have studied the electrochemical properties of carbon nanotubes at the single-nanotube level, by directly measuring the electrical current passing through.^{10-12, 16} This electrical current measurement, although powerful in studying the property of a particular carbon nanotube, suffers from certain drawbacks. First, the measurement at single-nanotube level requires delicate engineering, which limits the possibility for multiplexed observations. Moreover, the electrical current measurement lacks the spatial information, so that it does not differentiate

electrocatalytic reactions occurring at different locations. It is critical to know whether the sidewalls, tube ends, defect sites, or the remaining catalyst particles are responsible for the electrocatalytic properties. This question, however, cannot be answered by the electrical current measurements.

Based on the previous study of chemical catalysis of single metal nanoparticles, our group has established a single-molecule fluorescence approach to interrogate the electrocatalysis of SWNTs in situ.²⁶ By designing a fluorogenic electrocatalytic reaction and using wide-field fluorescence microscopy, multiple SWNTs during electrocatalysis were studied simultaneously at the single-turnover, single-reactive-site level. Super-resolution (SR) imaging techniques, such as Stochastic Optical Reconstruction Microscopy (STORM) and Photoactivation Localization Microscopy (PALM),¹⁷⁻²⁰ can spatially resolve and localize the position of individual fluorescent molecules with sub-diffraction limit resolution. Because the fluorescent product molecules are generated onsite, by applying SR imaging to SWNT electrocatalysis, the reactive sites have been resolved down to ~20 nm spatial precision. The single-molecule kinetic analysis led to an electrocatalysis mechanism of SWNTs, and the reactivity heterogeneity among reactive sites was quantified.

This chapter focuses on the electrocatalysis of arrays of aligned SWNTs on a quartz substrate. Large arrays of aligned SWNTs can be integrated into electronic devices as field effect transistors or biosensors; therefore many different methods have been reported to control the growth direction of SWNTs, such as using electric field²¹, gas flow²² or on patterned SiO₂²³. In this study, the SWNTs were synthesized through chemical vapor deposition (CVD) on a piece of quartz slide. The van der Waals interaction between SWNTs and quartz crystalline guided the growth direction of SWNTs, leading to large arrays of aligned SWNTs.²⁴⁻²⁵ Electrocatalysis was performed on these aligned SWNTs with SR imaging. The localizations of active sites were further correlated to AFM and SEM images, generating the spatial distribution of active sites along SWNTs. With these combined imaging techniques, questions such as whether the tube ends or defect sites are

responsible for the electrocatalytic activity, and whether multiple reactive sites on the same nanotube behave similarly might be answered. In addition, the potential-dependent kinetics are studied at the single nanotube, single active site level, which might help to understand the electron transfer process at the SWNT-solution interface in future.

4.2 Materials and Methods

4.2.1 Fabrication of Aligned SWNTs

Quartz slides with aligned SWNTs samples were designed and fabricated by Michael Segal in the Park group in the Department of Chemistry and Chemical Biology at Cornell. These samples were $\sim 25 \text{ mm} \times 20 \text{ mm} \times 0.5 \text{ mm}$ quartz chips, on which aligned SWNTs were grown and were further deposited gold electrodes to make electrical contacts with the SWNTs. The procedures for sample fabrication are summarized below.

4.2.1.1 Etching Mapping Features on Quartz Wafer

In order to precisely locate the sample area for single-molecule electrocatalysis imaging, $\sim 5 \mu\text{m} \times 5 \mu\text{m}$ markers with different shapes were etched on a piece of quartz wafer with 10 cm diameter using photolithography and O_2 plasma etching. The quartz wafer was first placed in a Yield Engineering Systems (YES) LP-III for vapor priming, using hexamethyldisilazane (HMDS) as adhesion promoter. SPR700-1.2 photoresist was then spin coated on wafer at 3,000 RPM for 30 s. The wafer was baked at $115 \text{ }^\circ\text{C}$ for 90 s before exposed under UV light for marker mapping. After exposure, the quartz wafer was baked for another 90 s at $115 \text{ }^\circ\text{C}$ and then transferred to a Hamatech processor to develop the photoresist. Later on, wafer was transferred to Oxford 82 etcher, where sample was treated by O_2 plasma for 1 min, CHF_3/O_2 for 15 min and another O_2 plasma for

1 min. Once etched, wafer was placed on hot strip bath for 2 hours and then transferred to commercial 1165 solution soaking for 2 days at room temperature.

4.2.1.2 Depositing Fe Catalyst for SWNT Growth

2 Å thick Fe catalyst strips were patterned on quartz wafer, each strip of ~ 5 μm in width. In this step, wafer was treated through YES vapor prime, SPR700-1.2, 115 °C baking and auto-stepping. The detailed condition was the same as the mapping feature etching step described above. After that, wafer was placed in Oxford 82 for O₂ plasma treatment for 1 min and then transferred to evaporator to deposit Fe. The ~10 cm wafer was cut into 25 mm × 20 mm × 0.5 mm quartz chips after patterning the Fe catalyst. Each wafer could generate about 12 pieces of samples.

4.2.1.3 The Growth of SWNTs

SWNTs growth was done in a tube furnace (Thermo Scientific), with CH₄ as carbon source. Two pieces of 25 mm × 20 mm × 0.5 mm quartz chips were placed in furnace each time, and pretreated at 900 °C in air for 2 hours to remove the remaining photoresist. The temperature was then lowered to 880 °C with Ar flow for 5 min. After that, H₂ was flowed in for another 5 min followed by the H₂/CH₄ feed gas for nanotube growth. The final SWNTs density on chip was largely controlled by the growth time. Most of the samples used for electrochemical activity measurements had growth time between 15 min ~ 30 min. Figure 4.1A shows the SEM image of the sample after the nanotube growth. After growth, sample was cooled down to room temperature in H₂ and Ar flow.

4.2.1.4 Depositing Au electrodes

A final step of patterning gold electrodes needs to be done before using the sample for electrochemical activity measurements. The gold electrodes serve two purposes: 1) to make electrical contact with SWNTs, and enable easy access for macro-sized working electrode; 2) to cover the Fe catalyst zone, where lots of carbon residues remained; these carbon residues can interfere with the electrochemical activity measurement on the SWNTs. In order to fulfill these purposes, the Au electrode was lithographed right on top of the Fe catalyst strips, so that carbon residues were blocked while all of the tubes are in contact (Figure 4.1B and C). In this step, quartz chips with nanotubes were first baked at 100 °C for 30 min, followed by spin coating the lift-off resist at 5000 RPM for 45 s. The alignment was done in an ABM contact aligner, and exposed under UV for 5 s. Prior to depositing Au, a 7 nm Cr layer was deposit first to make the quartz surface adhesive, and Au deposition was done immediately after, with final thickness ~ 60 nm.

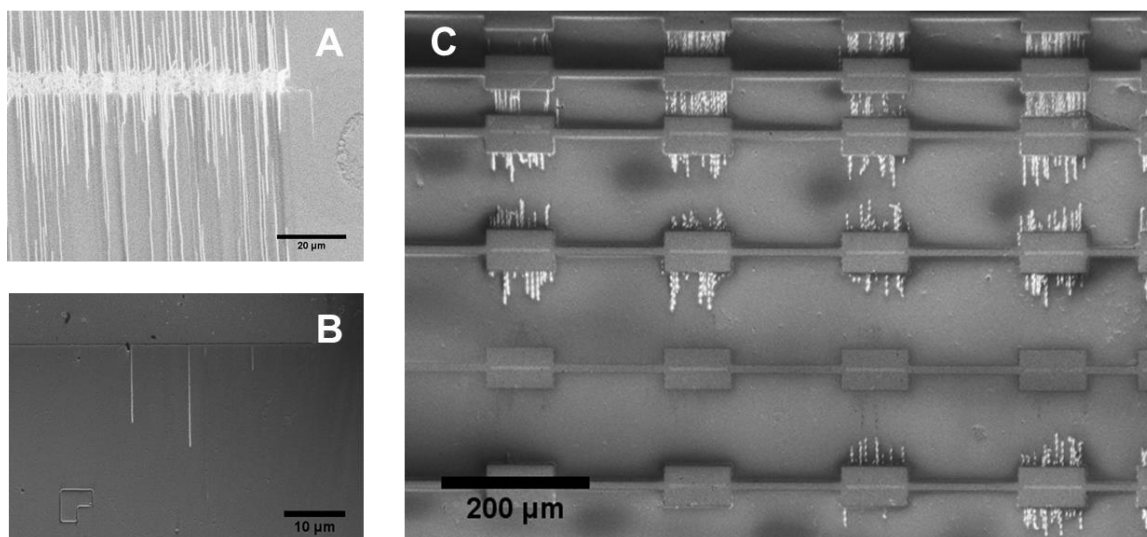


Figure 4.1 SEM of SWNTs on quartz chip. (A) SWNTs grown out of Fe catalyst strips. The bright horizontal line is the Fe catalyst strip, and the vertical lines are SWNTs. (B) SWNTs with deposited Au electrodes. The square on top is Au, bright vertical lines are SWNTs and the “U” shape on the lower left corner is the mapping feature. (C) Zoom out view that contains many blocks of SWNTs.

4.2.2 Sample Preparation for Single-Molecule Electrocatalysis Imaging

4.2.2.1 Cleaning the Quartz Slide with Aligned SWNTs

The as-synthesized samples may contain organic residues from lithography. Without proper cleaning, the EMCCD camera (Andor iXon, DV887DCS-BV) would be easily saturated by the fluorescent species remained on the quartz substrate under the light illumination conditions for single-molecule fluorescence imaging. Since the SWNTs were held on the quartz via van der Waals forces, acidic or basic solutions were not suitable for sample cleaning; SEM showed that soaking the quartz slide with aligned SWNTs in 1 M NaOH for 10 min resulted in the SWNTs to fall off from the quartz substrate. Therefore, to remove the amorphous carbon as well as other organic species, the sample was first annealed in H₂ atmosphere at 300 °C for 30 min. After annealing, the sample was sequentially soaked for 30 min in acetone, pure ethanol and water under sonication. Sample was then thoroughly rinsed with nanopure water, and placed under a 532 nm LED lamp (Thorlabs) for 1 hour to completely photobleach the remaining potentially fluorescent species. The final sample examined by EMCCD camera had background fluorescence intensity close to the camera dark counts, suggesting that the cleaning procedure was sufficient.

4.2.2.2 Electrochemical Flow Cell and Probing Reaction for Single-Molecule Electrocatalysis

The design of the flow micro-reactor for aligned SWNTs was similar to the one used in GOs study (Chapter 3, section 3.2.4 and Figure 3.4A). In brief, the flow cell (50 μm × 2 cm × 5 mm) was formed by double-sided tapes sandwiched between a glass slide and a borosilicate coverslip (Gold Seal[®]). Part of the glass slide was cut to insert the quartz slide with aligned SWNTs. On the glass slide, three holes were drilled. Two of them were used as in-and-out lets through polyethylene tubing for continuous solution flow driven by a syringe pump at 15 μL/minute. The third one was used to place the Ag/AgCl reference electrode. A Pt foil was sandwiched between

the coverslip and the quartz slide as the counter electrode. The fluorogenic probing reaction used for this study is once again the two-stage electro-reduction of resazurin (Figure 3.3A, Chapter 3). The first stage reduces resazurin irreversibly to the fluorescent resorufin; the second stage reduces resorufin to the nonfluorescent dihydroresorufin and is reversible. 50 mM phosphate buffer was used all times to maintain the pH at 7.3.

4.2.3 Single-Molecule Fluorescence Microscopy

Single-molecule fluorescence measurements were performed on a homebuilt prism-type total internal reflection (TIR) fluorescence microscope based on an Olympus IX71 inverted microscope. A continuous wave circularly polarized 532 nm laser beam (CrystaLaser, GCL-025-L-0.5%) of 3-6 mW was focused onto an area of $\sim 90 \times 45 \mu\text{m}^2$ on the sample to directly excite the fluorescence of resorufin. The fluorescence of resorufin was collected by a 60X NA1.2 water-immersion objective (UPLSAPO60XW, Olympus), optically filtered (HQ550LP) to reject laser scattering, and projected onto a camera (Andor iXon EMCCD, DV887DCS-BV), which is controlled by the Andor IQ software. Sometimes an additional filter (HQ580m60) was also used in the detection path. An additional 1.6X magnification on the microscope was also used when the SWNTs density was high. All optical filters are from Chroma Technology Corp. All experiments were done at room temperature.

4.2.4 Super-Resolution Imaging of Reactive Sites

Fluorescence time trajectories obtained from aligned SWNTs contained the similar features as the Au catalyzed amplex red reaction (Chapter 2 section 2.3.2, 2.3.3 and Figure 2.2, 2.3), where clear two-stage on and off behaviors were observed. Procedure for super-resolution imaging was described in detail in our previous publication²⁶. Briefly, the fluorescence image of a single

resorufin molecule at a SWNT reactive site spreads over a few pixels (Figure 4.2A) as a point spread function (PSF, each pixel = 267 nm). Fitting this PSF with a two-dimensional Gaussian function localizes its central position down to ± 4.5 nm accuracy (Figure 4.2B). The center localizations obtained by fitting the PSFs from many τ_{on} periods in a single fluorescence trajectory show a spread (Figure 4.2C), typical of super-resolution imaging results.^{17-18, 27-28} The spatial distribution of these localizations follows a two-dimensional Gaussian; its fwhm gives the spatial resolution of ~ 20 nm (Figure 4.2), comparable to what was achieved in PALM and STORM imaging,^{17-20, 27-28} but much higher resolution as compared with the diffraction-limited wide-field fluorescence image (Figure 4.2A).

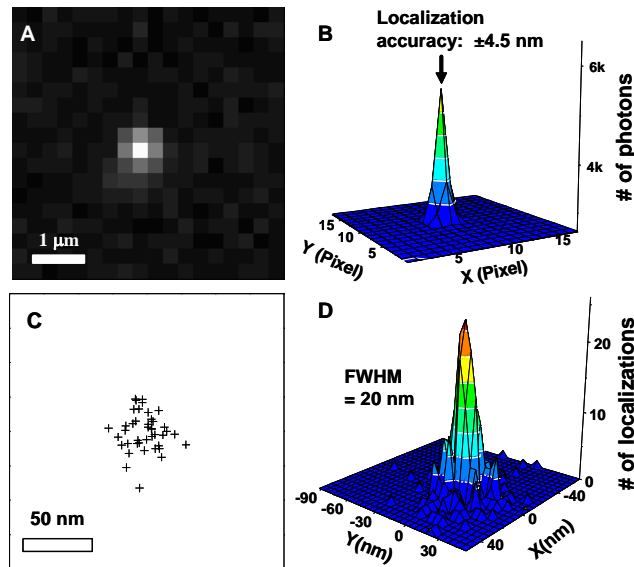


Figure 4.2 Super-resolution imaging of SWNT reactive sites. (A) Conventional wide-field fluorescence image of a single P at a reactive site during one τ_{on} period. Pixel size = 267 nm. (B) A two-dimensional Gaussian fit to the PSF function from the image in (A). The fwhm of the fit is ~ 410 nm. The center localization is determined to ± 4.5 nm. (C) The center localizations determined from the many τ_{on} periods of one fluorescence trajectory. (D) Two-dimensional histogram of the localization distribution. A Gaussian fit gives fwhm ~ 20 nm. To increase statistics, the localizations from 25 reactive sites are combined, for which the center mass of the localizations from each reactive site was used for alignment, as done in STORM imaging.¹⁷ Figure adapted from Xu et al.²⁶

4.3 Results and Discussion

4.3.1 Morphologies of aligned SWNTs

Figure 4.3A shows the AFM image of as-fabricated SWNTs on quartz substrate. In this image, SWNTs were perpendicular to the Fe catalyst strips and parallel to each other, forming arrays of aligned nanotubes. The straightness of the SWNTs indicates that their being pristine and low-defect (Figure 4.3A).²⁵ The grown SWNTs have lengths ranging from a few tens up to a hundred microns. The average diameter measured by AFM for as-grown SWNTs was ~ 1.4 nm, which suggests them being single-walled²⁹. The maximum density of aligned SWNTs on quartz can be as high as 10~20 SWNTs / μm . However, high SWNTs density prohibits the precise overlap of active sites from single-molecule catalysis imaging on nanotubes, therefore the SWNTs growth time was carefully controlled to lower the SWNT density. The growth time for the samples used in this study was set to 5 min and the resulted quartz substrates had less than 20 nanotubes per 100 μm .

Figure shows an AFM image of one block of SWNTs. During the electrochemical activity measurements, these SWNTs were used as working electrodes and a constant negative potential was applied on them. Figure 4.3B and C are the AFM and SEM images of the same array after applying -0.7 V (vs. Ag/AgCl reference electrode) potential for ~ 7 hours. The AFM measured averaged diameter for as-fabricated SWNTs was 1.3 ± 0.4 nm (Figure 4.3A), and 1.3 ± 0.6 nm after the electrocatalysis (Figure 4.3B). However in both AFM and SEM images, SWNTs after electrocatalysis showed more bends, which are probably due to the generation of defects in the hexagonal lattice by the applied potential.³⁰⁻³¹

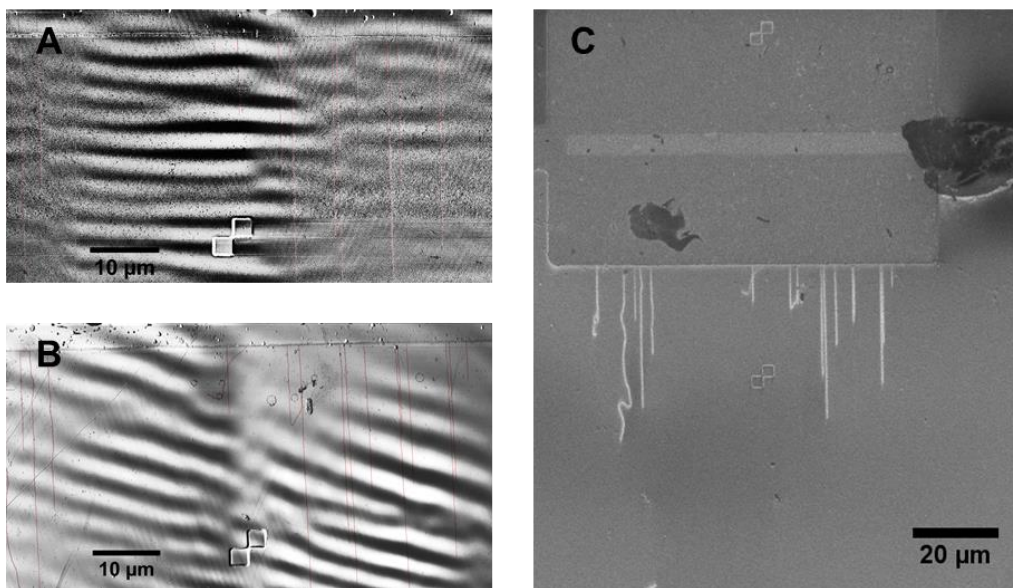


Figure 4.3 AFM phase images of one block of aligned SWNTs before (A) and after (B) applying a constant -0.7 V (vs. Ag/AgCl) potential for 7 hours. Red false color is used in (A) and (B) to better visualize SWNTs. (C) The SEM image of the same block after the electrochemical measurement.

4.3.2 Selection of Possible Active Sites in Single-Molecule Electrocatalysis

The SWNTs are invisible under optical microscope. Fluorescent bursts were only observed when a constant reductive potential (e.g., -0.2 V to -1.0 V vs. Ag/AgCl) was applied on SWNTs, where electrochemical transformation took place forming resorufin. Because the fluorescent molecules were generated onsite, locations with repetitive fluorescent bursts are likely the active sites. Three criteria were used in our analysis in order to select out the possible active sites from artifacts such as random adsorption of the resorufin molecule from the solution. The procedures for these criteria are detailed below.

4.3.2.1 Extraction of Fluorescence Time Trajectory

A homemade IDL program was used to track the coordinates of all fluorescent bursts within each image frame. The intensity versus time trajectory was then extracted at the location of each bursts by integrating over the surrounding area of $\sim 1 \times 1 \mu\text{m}^2$ (i.e., 7×7 pixel, Chapter 2 section 2.4.2.1) throughout the image stacks of the entire movie. Figure 4.4A is an exemplary fluorescence trajectory. To register as a possible active site, this trajectory needs to contain the following features: (1) the fluorescent bursts are continually reoccurring; (2) the total intensity counts for individual bursts are similar, which is a signature of single resorufin molecule detection; (3) fluorescent bursts are digital where the on time (τ_{on} , the duration of each burst) and off time (τ_{off} , the time separation between temporally neighboring bursts) are clear; (4) the averaged τ_{on} is significantly shorter than the time scale for the known photoblinking kinetics of resorufin.³²

4.3.2.2 Correlating the Locations of Fluorescent Bursts with SEM Image

Figure 4.4 Single-turnover detection of aligned SWNTs electrochemical catalysis. (A) Fluorescence trajectory from a local spot on the quartz substrate. (B) The enlarged view of one segment of A. (C) Locations of extracted fluorescence time trajectories overlaid on the SEM image. In the SEM image, the bright horizontal line on top is the edge of the Au electrode, vertical bright lines are SWNTs, and the “ Γ ” shape in the center is the etched mapping feature on the quartz. Red circles point out the locations, one of which (site 1) gives the fluorescence trajectory in (A). Shows the locations of fluorescence time trajectories overlapped on a SEM image taken after single-molecule electrocatalysis measurements. Each black dot marks a location whose fluorescence time trajectory fulfills the single-molecule criteria (section 4.3.2.1). The overlapping was achieved by aligning the etched markers and defects on Au electrodes (Figure 4.4C, white horizontal line in SEM), as well as the pre-deposit 100 nm spherical Au nanoparticles (Figure 4.4C, bright dots), which were visible in both optical microscope and SEM. It is usually difficult to precisely assign the locations of fluorescence time trajectories to individual SWNTs (Figure 4.4C, bright vertical lines), because some SWNTs lost interaction with the quartz substrate during electrocatalysis measurements (~14 hours) and their shapes changed in the end. Therefore, locations that overlaid with or close by SWNTs were all retained as possible active sites. On the other hand, locations far away from SWNTs were considered artifacts and discarded for later analysis. These artifacts are formed possibly because of the residues of photolithography that survived from the sample cleaning procedure. The resorufin molecule in flow may preferentially bind to these residues, giving bursts similar to single-molecule catalysis events.

4.3.2.3 Further Filtering of the Possible Active Sites with Super-Resolution Imaging

The spatial localizations of the fluorescence trajectories (Figure 4.4C, black dots) suggest that the electrocatalysis occurs at discrete sites rather than on the entire sidewall of the SWNTs. This observation agrees with our earlier study on ITO supported commercial SWNTs.²⁶ As a

consequence, the center localizations for fluorescent bursts coming from a true active site should spread in an area with its size close to 15~40 nm (e.g., the spatial resolution of super-resolution imaging).^{19, 26, 33-44} On the other hand, the in-flow resorufin binding should be random on the quartz substrate; or if they preferentially bind to residues of photolithography, their center localizations perhaps should scatter over a much larger area. Therefore, super-resolution imaging technique was applied to all possible candidates for active sites. Trajectories with scattered center localizations were considered artifacts and removed from further analysis.

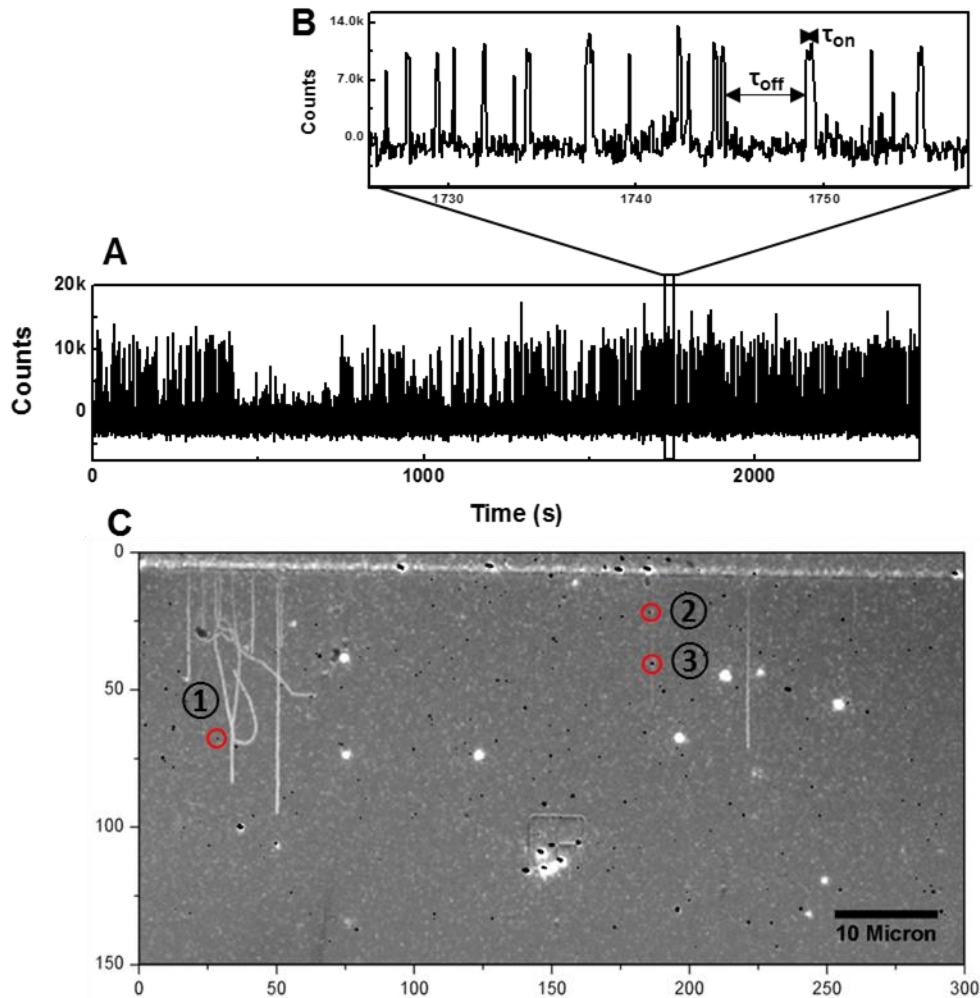


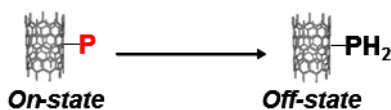
Figure 4.4 Single-turnover detection of aligned SWNTs electrochemical catalysis. (A) Fluorescence trajectory from a local spot on the quartz substrate. (B) The enlarged view of one segment of A. (C) Locations of extracted fluorescence time trajectories overlaid on the SEM image. In the SEM image, the bright horizontal line on top is the edge of the Au electrode, vertical bright lines are SWNTs, and the “ Γ ” shape in the center is the etched mapping feature on the quartz. Red circles point out the locations, one of which (site 1) gives the fluorescence trajectory in (A).

4.3.3 Resazurin Concentration Titration on Aligned SWNTs

Resazurin concentration titration was carried out under a steady -0.35 V potential (vs. Ag/AgCl). Each localized spots that generated fluorescent bursts were systematically analyzed using the above procedures to select out the possible active sites. Site 2 and 3 were qualified as the active sites for electrocatalysis and they were on the same SWNT (Figure 4.4C, circled in red). The fluorescence trajectory of site 3 occasionally showed a second on-level (Figure 4.5A), which is likely due to the formation of an additional resorufin molecule at the same location³². However, having two product molecules at the same time was very rare and statistically insignificant. Figure 4.5B shows the 2D histogram of center localizations for fluorescent bursts from site 3. These localizations were corrected for sample drifting by tracking the movements of pre-deposited 100 nm Au nanoparticles throughout the entire movie (~ 14 hours). The 2D histogram was fitted with a Gaussian function with fwhm ~ 27 nm, which is close to the spatial resolution of super-resolution imaging. Therefore site 3 is very likely a real active site for electrocatalysis.

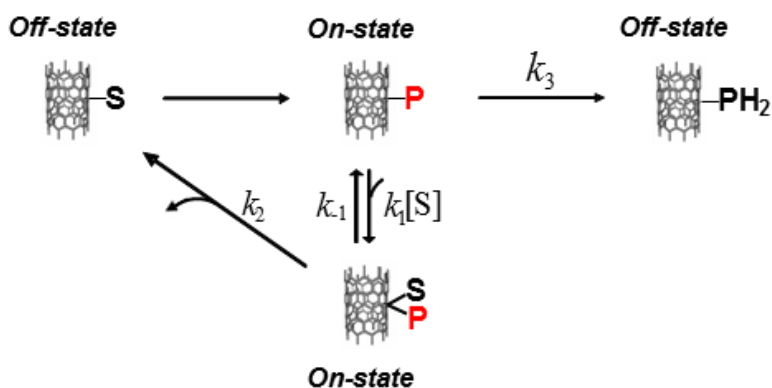
Our previous work of ITO supported commercial SWNTs showed that the on-time were independent of resazurin concentration (Figure 4.5D).²⁶ We attributed the on-time process to be dominated by a simple reduction reaction from resorufin to non-fluorescent dihydroresorufin (Scheme 4.1), where resazurin does not participate in.

Scheme 4.1 On-time kinetics for ITO supported commercial SWNTs. P stands for resorufin and PH_2 stands for dihydroresorufin.



Surprisingly, the $\langle\tau_{\text{on}}\rangle^{-1}$ of site 2 and 3 on aligned SWNTs showed a clear increase then saturation behavior versus the resazurin concentration (Figure 4.5C), which suggests that the reactant resazurin is involved in the on-time process, for example a reactant assisted substitution (Scheme 4.2).^{32, 45 32, 45} In this possible scheme, two parallel pathways exist for the on-site resorufin molecule: one is the direct reduction, forming the non-fluorescent dihydroresorufin. The associated rate constant for this pathway is k_3 . For the alternative pathway, a resazurin molecule coming from the surrounding solution first undergoes a reversible adsorption to the same site of resorufin, which can then lead to the desorption of resorufin with a rate constant k_2 . For ITO supported commercial SWNTs, it is likely that $k_2 = k_3$ (i.e. molecules have no preferences on these two pathways), or $k_1/(k_1 + k_2) = 0$ (i.e. alternative pathway is effectively shut down).⁴⁶⁻⁴⁷ On the other hand, the aligned SWNTs would have $k_2 > k_3$ (i.e. the resazurin assisted dissociation is more preferred), resulting in a resazurin concentration dependent behavior in $\langle\tau_{\text{on}}\rangle^{-1}$ (Chapter 1, section 1.3 and Figure 1.2).

Scheme 4.2 Possible on-time kinetics on aligned SWNTs. S stands for resazurin.



There are several possibilities which might cause the differences between ITO supported SWNTs and aligned SWNTs. The ITO supported commercial SWNTs were refluxed at 80 °C for

24 hours to remove the residual metal catalysts.⁴⁸ It is reported that the residual metal or the impurities within the residual metal catalysts were responsible for some electrochemical reactions.⁴⁹⁻⁵¹ In our SWNTs catalyzed resazurin reduction to resorufin and further to dihydroresorufin reaction, the electrocatalytic activity of nitric acid purified SWNTs was higher than the unpurified ones. Whether promoting or prohibiting, it seems that the metal residue can affect the electrocatalytic activity. For the aligned SWNTs, the Fe catalyst strips remained during the electrochemical catalysis, and instead of refluxing in nitric acid, which provides a strong oxidation environment, the aligned SWNTs were annealed in H₂ at 300 °C, which is a strong reduction environment. The different purification procedure as well as the metal residue inevitably resulted in structural differences between commercial SWNTs and aligned SWNTs, which in turn may affect the reaction kinetics. In addition, the commercial SWNTs were directly deposited on a piece of ITO substrate, while the aligned SWNTs have only one end in contact with the Au electrode. And it is obvious that the contact between the electrodes and SWNTs would vary for these two types of sample. It is worth noting that for this specific example, site 2 and 3 were located on the same SWNT. Their $\langle\tau_{on}\rangle^{-1}$ changes versus resazurin concentration were almost identical here (Figure 4.5C).

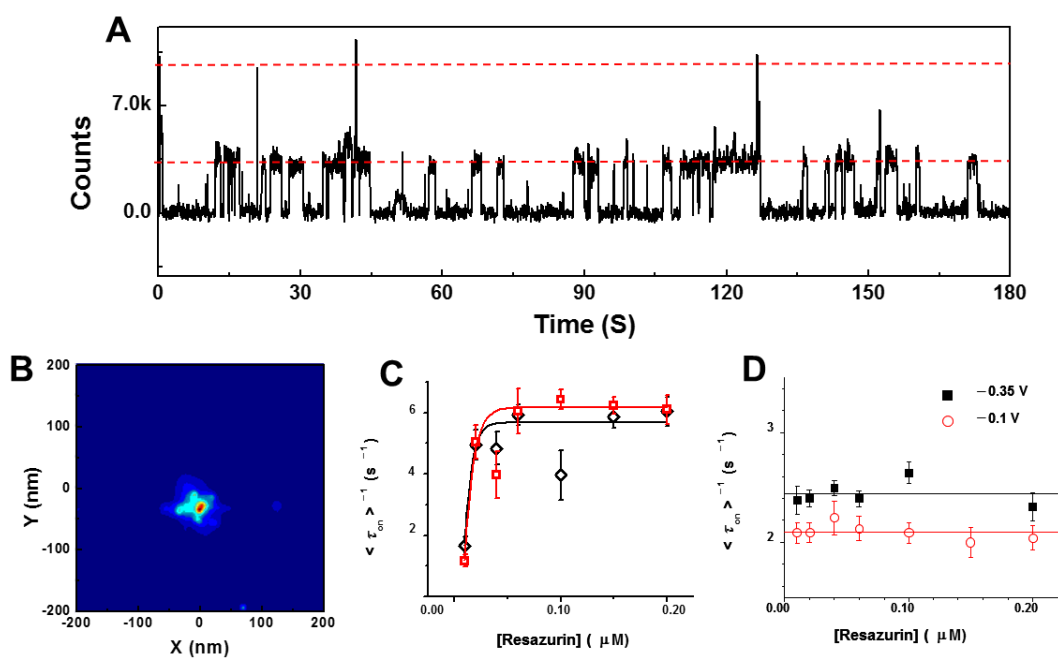


Figure 4.5 Resazurin concentration dependence from two individual active sites. (A) A segment of fluorescence trajectory from site 3 in Figure 4.4C. (B) Two-dimensional histogram of the center localization of bursts detected from site 3. Gaussian fit gives fwhm ~ 27 nm. (C) The resazurin concentration dependence of $\langle \tau_{on} \rangle^{-1}$ at site 2 (black) and 3 (red) under -0.35 V potential (vs. Ag/AgCl). They were on the same SWNT. (D) The $\langle \tau_{on} \rangle^{-1}$ dependence at two different potentials for ITO supported commercial SWNTs. Each data points were averaged over more than 50 reactive sites. (D) Adapted from Xu et al.²⁶

4.3.4 Potential Titration on Aligned SWNTs

In scheme 4.2, k_3 is the rate constant that involves the electron transfer. Previous study by Heller and coworkers used Gerischer-Marcus model to predict the electron transfer kinetics at the SWNT-solution interface.¹² According to their study, the electron transfer rate is dependent on the applied potential and the density of states (DOS) of SWNTs. For instance, semi-conducting and metallic SWNTs have different DOS (Figure 4.6A) and consequently, their potential-dependent electron transfer rates should be different. Here in this study, the on-time process for aligned SWNTs is composed by two parallel pathways: the electron transfer to resorufin (k_3) and the resazurin assisted resorufin dissociation (k_2). By tuning the applied potential, thus the electron transfer rate, k_3 is expected to be different from tube to tube depending on their structures. Although this electron transfer pathway is less preferred for aligned SWNTs (section 4.3.3), $\langle\tau_{on}\rangle^{-1}$ is likely to change according to the applied potential. Therefore, the potential dependence of $\langle\tau_{on}\rangle^{-1}$ was examined for multiple active sites on aligned SWNTs. Shown in Figure 4.6B are the dependences for site 2 and 3. Their absolute values in $\langle\tau_{on}\rangle^{-1}$ were close to each other under various potentials, and neither of them showed clear potential dependence. This independence behavior versus the applied potential is consistent with the resazurin concentration titration in section 4.3.3, where the electron transfer is less preferred for on-time process. However, no conclusions can be made at this moment, because of lacking enough statistics.

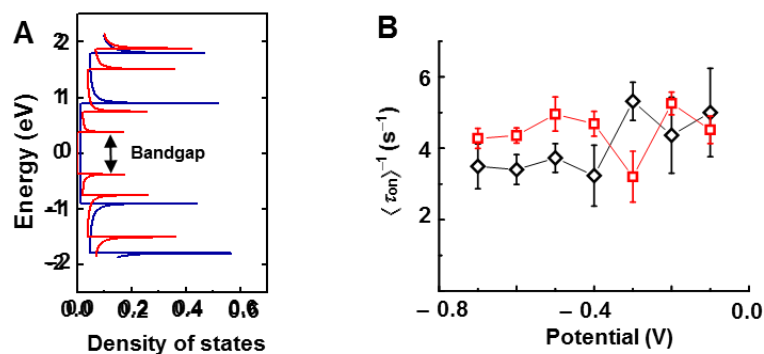


Figure 4.6 Potential dependence of $\langle \tau_{on} \rangle^{-1}$. (A) Simulated density of states (DOS) for metallic (9, 9) and semi-conducting (8, 6) nanotube.⁵² (B) The potential dependence of $\langle \tau_{on} \rangle^{-1}$ at site 2 (black) and 3 (red). 50 nM resazurin was dispersed in 50 mM pH 7.3 phosphate buffer.

4.3.5 Proton Concentration Titration on ITO Supported Commercial SWNTs

The fluorescent probing reaction used in this study is the same as in Chapter 3, the electrocatalysis of GOs. From the chemical equation in Figure 3.3A in Chapter 3, both the reduction of resazurin to resorufin and that of resorufin to dihydroresorufin involve two protons. This reaction represents a large category of chemical transformations, namely proton coupled electron transfer (PCET). To gain information on the proton involvement in the reaction kinetics of SWNT-catalyzed electroreduction of resorufin to dihydroresorufin, here we performed pH titration of the electrocatalysis by the commercial SWNTs deposited on ITO slides.

Our analysis focuses on the on-time process, because previous study suggests that the off-time involves the resazurin substitution aside from PT and ET,⁴⁶ thus being much more complicated. The proton concentration dependence of $\langle \tau_{on} \rangle^{-1}$ from individual reactive sites show four types of behaviors (Figure 4.7A-D): 12% of the active sites decrease with increasing $[H^+]$ and flattens; 7% increases with increasing $[H^+]$ and eventually saturates; 67% were independent and 14% increases

initially and then decreases. Among these four types, the ones that are independent of pH were dominating. Therefore the averaged trend for all active sites also appeared to be independent (Figure 4.7E).

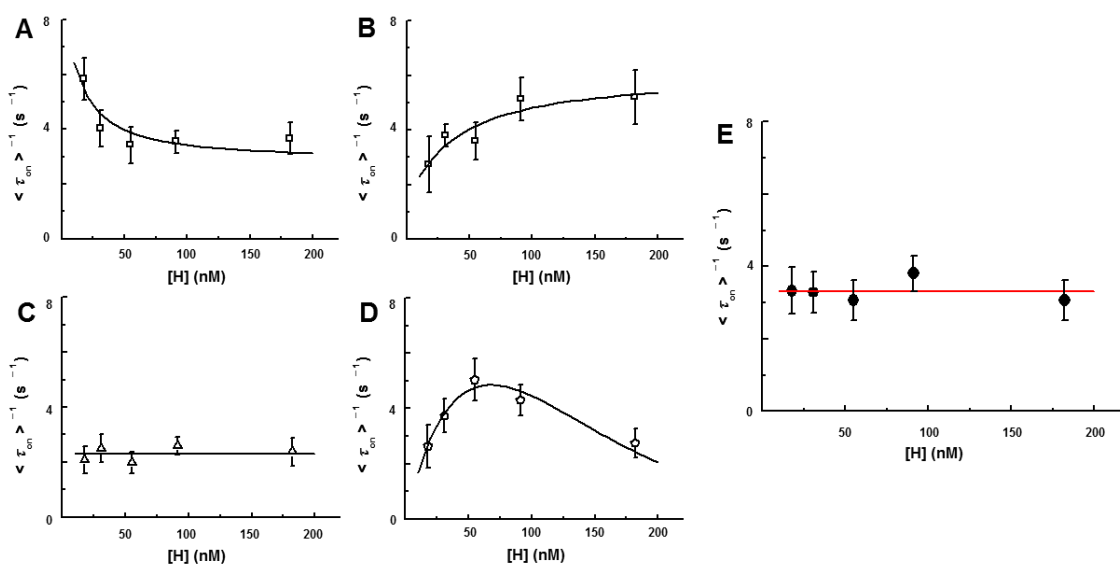


Figure 4.7 (A-D) Proton concentration dependence of $\langle \tau_{on} \rangle^{-1}$ in 50 mM phosphate buffer. Four types of behaviors are observed. Resazurin concentration was maintained at 50 nM, and potential fixed at -0.4 V (vs. Ag/AgCl). (E) The averaged $\langle \tau_{on} \rangle^{-1}$ for all reactive sites versus proton concentration. All error bars in the the graphs are S.D.

4.4 References

1. Iijima, S.; Ichihashi, T., Single-shell carbon nanotubes of 1-nm diameter. *Nature* **1993**, *363* (6430), 603-605.
2. Bethune, D. S.; Klang, C. H.; de Vries, M. S.; Gorman, G.; Savoy, R.; Vazquez, J.; Beyers, R., Cobalt-catalysed growth of carbon nanotubes with single-atomic-layer walls. *Nature* **1993**, *363* (6430), 605-607.
3. Ajayan, P.; Zhou, O., Applications of Carbon Nanotubes. In *Carbon Nanotubes*, Dresselhaus, M.; Dresselhaus, G.; Avouris, P., Eds. Springer Berlin Heidelberg: 2001; Vol. 80, pp 391-425.
4. Dresselhaus, S.; Dresselhaus, G.; Avouris, P., *Carbon Nanotubes: Synthesis, Structure, Properties, and Applications*. Springer: 2001.
5. O'Connell, M. J., *Carbon Nanotubes: Properties and Applications*. Taylor & Francis: 2006.
6. Lu, W.; Lieber, C. M., Nanoelectronics from the bottom up. *Nat Mater* **2007**, *6* (11), 841-850.
7. Dai, H., Carbon Nanotubes: Synthesis, Integration, and Properties. *Accounts of Chemical Research* **2002**, *35* (12), 1035-1044.
8. Carlson, L. J.; Krauss, T. D., Photophysics of Individual Single-Walled Carbon Nanotubes. *Accounts of Chemical Research* **2008**, *41* (2), 235-243.
9. Hersam, M. C., Progress towards monodisperse single-walled carbon nanotubes. *Nat Nano* **2008**, *3* (7), 387-394.
10. Campbell, J. K.; Sun, L.; Crooks, R. M., Electrochemistry Using Single Carbon Nanotubes. *Journal of the American Chemical Society* **1999**, *121* (15), 3779-3780.
11. Heller, I.; Kong, J.; Heering, H. A.; Williams, K. A.; Lemay, S. G.; Dekker, C., Individual Single-Walled Carbon Nanotubes as Nanoelectrodes for Electrochemistry. *Nano Letters* **2004**, *5* (1), 137-142.
12. Heller, I.; Kong, J.; Williams, K. A.; Dekker, C.; Lemay, S. G., Electrochemistry at Single-Walled Carbon Nanotubes: The Role of Band Structure and Quantum Capacitance. *Journal of the American Chemical Society* **2006**, *128* (22), 7353-7359.
13. Gooding, J. J., Nanostructuring electrodes with carbon nanotubes: A review on electrochemistry and applications for sensing. *Electrochimica Acta* **2005**, *50* (15), 3049-3060.
14. McCreery, R. L., Advanced Carbon Electrode Materials for Molecular Electrochemistry. *Chemical Reviews* **2008**, *108* (7), 2646-2687.
15. Harris, P. J. F., *Carbon Nanotube Science: Synthesis, Properties and Applications*. Cambridge University Press: 2009.
16. Goldsmith, B. R.; Coroneus, J. G.; Kane, A. A.; Weiss, G. A.; Collins, P. G., Monitoring Single-Molecule Reactivity on a Carbon Nanotube. *Nano Letters* **2007**, *8* (1), 189-194.

17. Bates, M.; Huang, B.; Dempsey, G. T.; Zhuang, X., Multicolor Super-Resolution Imaging with Photo-Switchable Fluorescent Probes. *Science* **2007**, *317* (5845), 1749-1753.
18. Rust, M. J.; Bates, M.; Zhuang, X., Sub-diffraction-limit imaging by stochastic optical reconstruction microscopy (STORM). *Nature Methods* **2006**, *3* (10), 793-796.
19. Hess, S. T.; Girirajan, T. P. K.; Mason, M. D., Ultra-High Resolution Imaging by Fluorescence Photoactivation Localization Microscopy. *Biophysical Journal* **2006**, *91* (11), 4258-4272.
20. Betzig, E.; Patterson, G. H.; Sougrat, R.; Lindwasser, O. W.; Olenych, S.; Bonifacino, J. S.; Davidson, M. W.; Lippincott-Schwartz, J.; Hess, H. F., Imaging Intracellular Fluorescent Proteins at Nanometer Resolution. *Science* **2006**, *313* (5793), 1642-1645.
21. Zhang, Y.; Chang, A.; Cao, J.; Wang, Q.; Kim, W.; Li, Y.; Morris, N.; Yenilmez, E.; Kong, J.; Dai, H., Electric-field-directed growth of aligned single-walled carbon nanotubes. *Applied Physics Letters* **2001**, *79* (19), 3155.
22. Liu, H.; Takagi, D.; Chiashi, S.; Homma, Y., The controlled growth of horizontally aligned single-walled carbon nanotube arrays by a gas flow process. *Nanotechnology* **2009**, *20* (34), 345604.
23. Maehashi, K.; Iwasaki, S.; Ohno, Y.; Kishimoto, T.; Inoue, K.; Matsumoto, K., Aligned Single-Walled Carbon Nanotube Arrays on Patterned SiO₂/Si Substrates. *Japanese Journal of Applied Physics* **2010**, *49* (6S), 06GK01.
24. Okuda, S.; Okamoto, S.; Ohno, Y.; Maehashi, K.; Inoue, K.; Matsumoto, K., Horizontally Aligned Carbon Nanotubes on a Quartz Substrate for Chemical and Biological Sensing. *The Journal of Physical Chemistry C* **2012**, *116* (36), 19490-19495.
25. Xiao, J.; Dunham, S.; Liu, P.; Zhang, Y.; Kocabas, C.; Moh, L.; Huang, Y.; Hwang, K.-C.; Lu, C.; Huang, W.; Rogers, J. A., Alignment Controlled Growth of Single-Walled Carbon Nanotubes on Quartz Substrates. *Nano Letters* **2009**, *9* (12), 4311-4319.
26. Xu, W.; Shen, H.; Kim, Y. J.; Zhou, X.; Liu, G.; Park, J.; Chen, P., Single-Molecule Electrocatalysis by Single-Walled Carbon Nanotubes. *Nano Letters* **2009**, *9* (12), 3968-3973.
27. Bates, M.; Huang, B.; Zhuang, X., Super-resolution microscopy by nanoscale localization of photo-switchable fluorescent probes. *Current Opinion in Chemical Biology* **2008**, *12* (5), 505-514.
28. Huang, B.; Wang, W.; Bates, M.; Zhuang, X., Three-Dimensional Super-Resolution Imaging by Stochastic Optical Reconstruction Microscopy. *Science* **2008**, *319* (5864), 810-813.
29. Sumio Iijima, T. I., Single-shell carbon nanotubes of 1-nm diameter. *Nature* **1993**, *363*, 3.
30. Lambin, P.; Fonseca, A.; Vigneron, J. P.; Nagy, J. B.; Lucas, A. A., Structural and electronic properties of bent carbon nanotubes. *Chemical Physics Letters* **1995**, *245* (1), 85-89.
31. Chico, L.; Crespi, V. H.; Benedict, L. X.; Louie, S. G.; Cohen, M. L., Pure Carbon Nanoscale Devices: Nanotube Heterojunctions. *Physical Review Letters* **1996**, *76* (6), 971-974.

32. Xu, W.; Kong, J. S.; Yeh, Y.-T. E.; Chen, P., Single-molecule nanocatalysis reveals heterogeneous reaction pathways and catalytic dynamics. *Nature Materials* **2008**, *7* (12), 992-996.
33. Huang, B.; Bates, M.; Zhuang, X., Super-Resolution Fluorescence Microscopy. *Annual Review of Biochemistry* **2009**, *78* (1), 993-1016.
34. Lidke, K.; Rieger, B.; Jovin, T.; Heintzmann, R., Superresolution by localization of quantum dots using blinking statistics. *Opt. Express* **2005**, *13* (18), 7052-7062.
35. Rust, M. J.; Bates, M.; Zhuang, X., Sub-diffraction-limit imaging by stochastic optical reconstruction microscopy (STORM). *Nat Meth* **2006**, *3* (10), 793-796.
36. Thompson, R. E.; Larson, D. R.; Webb, W. W., Precise Nanometer Localization Analysis for Individual Fluorescent Probes. *Biophysical Journal* **2002**, *82* (5), 2775-2783.
37. Yildiz, A.; Selvin, P. R., Fluorescence Imaging with One Nanometer Accuracy: Application to Molecular Motors. *Accounts of Chemical Research* **2005**, *38* (7), 574-582.
38. Betzig, E.; Trautman, J. K., Near-Field Optics: Microscopy, Spectroscopy, and Surface Modification Beyond the Diffraction Limit. *Science* **1992**, *257* (5067), 189-195.
39. Hell, S. W.; Wichmann, J., Breaking the diffraction resolution limit by stimulated emission: stimulated-emission-depletion fluorescence microscopy. *Opt. Lett.* **1994**, *19* (11), 780-782.
40. Hell, S. W., Far-Field Optical Nanoscopy. *Science* **2007**, *316* (5828), 1153-1158.
41. Hell, S. W.; Kroug, M., Ground-state-depletion fluorescence microscopy: A concept for breaking the diffraction resolution limit. *Appl. Phys. B* **1995**, *60* (5), 495-497.
42. Gustafsson, M. G. L., Nonlinear structured-illumination microscopy: Wide-field fluorescence imaging with theoretically unlimited resolution. *Proceedings of the National Academy of Sciences of the United States of America* **2005**, *102* (37), 13081-13086.
43. Cheezum, M. K.; Walker, W. F.; Guilford, W. H., Quantitative Comparison of Algorithms for Tracking Single Fluorescent Particles. *Biophysical Journal* **2001**, *81* (4), 2378-2388.
44. Gordon, M. P.; Ha, T.; Selvin, P. R., Single-molecule high-resolution imaging with photobleaching. *Proceedings of the National Academy of Sciences of the United States of America* **2004**, *101* (17), 6462-6465.
45. Xu, W.; Kong, J. S.; Chen, P., Probing the catalytic activity and heterogeneity of Au-nanoparticles at the single-molecule level. *Physical Chemistry Chemical Physics* **2009**, *11* (15), 2767.
46. Weilin Xu, H. S., Yoon Ji Kim, Xiaochun Zhou, Guokun Liu, Jiwoong Park, and Peng Chen, Single-Molecule Electrocatalysis by Single-Walled Carbon Nanotubes. *Nano Letters* **2009**, *9*, 3968-3973.
47. Shen, H.; Xu, W.; Chen, P., Single-molecule nanoscale electrocatalysis. *Physical Chemistry Chemical Physics* **2010**, *12* (25), 6555.

48. Hu, H.; Zhao, B.; Itkis, M. E.; Haddon, R. C., Nitric Acid Purification of Single-Walled Carbon Nanotubes. *The Journal of Physical Chemistry B* **2003**, *107* (50), 13838-13842.
49. Pumera, M.; Iwai, H., Metallic Impurities within Residual Catalyst Metallic Nanoparticles Are in Some Cases Responsible for “Electrocatalytic” Effect of Carbon Nanotubes. *Chemistry – An Asian Journal* **2009**, *4* (4), 554-560.
50. Pumera, M.; Ambrosi, A.; Chng, E. L. K., Impurities in graphenes and carbon nanotubes and their influence on the redox properties. *Chemical Science* **2012**, *3* (12), 3347-3355.
51. Šljukić, B.; Banks, C. E.; Compton, R. G., Iron Oxide Particles Are the Active Sites for Hydrogen Peroxide Sensing at Multiwalled Carbon Nanotube Modified Electrodes. *Nano Letters* **2006**, *6* (7), 1556-1558.
52. Mintmire, J. W.; White, C. T., Universal Density of States for Carbon Nanotubes. *Physical Review Letters* **1998**, *81* (12), 2506-2509.